

## ABSTRACT

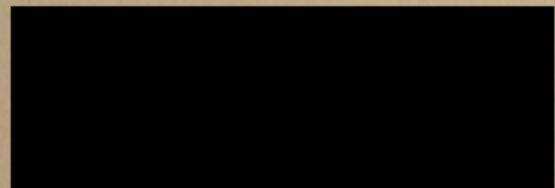
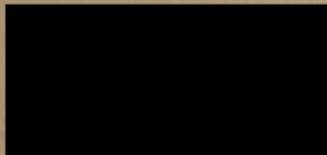
ERLAT, AHMET GÜN. Barrier Properties of Plasma Deposited SiO<sub>x</sub> Transparent Coatings on Polymer Substrates. (Under the direction of Richard J. Spontak.)

The focus of this study is to enhance the barrier performance of two commodity polymers, namely, poly(ethylene terephthalate) (PET) and polycarbonate (PC), through the plasma deposition of SiO<sub>x</sub>. A thin SiO<sub>x</sub> surface coating on either polymer substrate promotes a dramatic reduction in oxygen (and water vapor, in the case of PET) permeation without loss of fracture toughness. These combined properties are of the utmost importance in barrier materials currently sought by the food packaging, electronics and biomedical device industries.

In the PET/SiO<sub>x</sub> study, an extensive Non-Parametric Response Surface Methods optimization algorithm has been employed to identify the optimum Plasma-Enhanced Chemical Vapor Deposition (PECVD) conditions required to obtain SiO<sub>x</sub> coatings of superior barrier quality. Results from this study provide statistically meaningful correlations between surface morphology, coating microstructure and oxygen/water vapor transport mechanism in SiO<sub>x</sub> coatings varying in barrier performance. Relative to the uncoated PET substrate, the oxygen transmission rate decreases by up to two orders of magnitude upon SiO<sub>x</sub> treatment under the optimum deposition conditions discerned here. Atomic force microscopy reveals that the surface texture and topography of these SiO<sub>x</sub> coatings vary from smooth surfaces composed of densely packed, spherical SiO<sub>x</sub> grains to rough surfaces with large, irregularly shaped grains (which most likely create more defect sites) as the barrier quality decreases. Planar transmission electron microscopy provides direct evidence of the nanoscale defects responsible for permeation. These defects increase in both size and area density with decreasing barrier efficacy. Activation energy measurements demonstrate that the gas transport mechanism occurs two steps: (i) diffusion through defects in the SiO<sub>x</sub> coatings and (ii) thermally activated transport through the PET matrix. The SiO<sub>x</sub> coating becomes rate limiting in the case of water vapor, not oxygen,

transmission due to specific chemical (hydrogen bonding) interactions between water molecules and the channel walls of the defects in the  $\text{SiO}_x$  coatings.

In the companion study, the principal objective is to ascertain the effects of systematically varied (not optimized) PECVD parameters (e.g., deposition time, power, pressure, and oxygen and organosilicon monomer flow rates) on  $\text{SiO}_x$  coating characteristics and properties, including oxygen transmission rate, coating thickness, refractive index and surface morphology. As in the previous study, activated rate theory is employed to elucidate the mechanism of gas transport in  $\text{PC/SiO}_x$  laminates. Sufficient time is required for plasma stabilization, resulting in a critical coating thickness necessary for high barrier materials. An increase in power level results in a significant reduction in oxygen transmission, and is accompanied by increases in coating thickness and refractive index (or density). Variation in surface topology analogous to that observed in the  $\text{PET/SiO}_x$  study is also observed. The system pressure in PECVD should be maintained sufficiently low to minimize particle formation and thereby yield a dense  $\text{SiO}_x$  coating. Data obtained during the course of this work confirm that the organosilicon monomer flow rate is responsible for the amount of material deposited on the polymer surface, and indicate that this flow rate should be sufficiently high to ensure high-quality barrier coatings. Changes in both oxygen and monomer flow rate also have a direct impact on coating surface morphology. Unlike the  $\text{PET/SiO}_x$  system, an increase in the activation energy of oxygen permeation is found to occur as the barrier performance (and thickness) of the  $\text{SiO}_x$  coatings increases. A gas transport model that is consistent with experimental observations is proposed in which defect size and tortuosity in a thin  $\text{SiO}_x$  coating constitute rate-limiting considerations.



**BARRIER PROPERTIES OF PLASMA DEPOSITED SiO<sub>x</sub>  
TRANSPARENT COATINGS ON POLYMER SUBSTRATES**

by

**AHMET GÜN ERLAT**

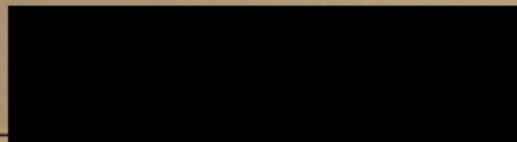
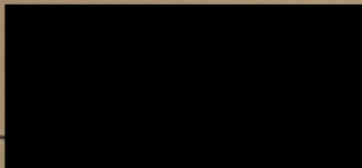
A thesis submitted to the Graduate Faculty of  
North Carolina State University  
in partial fulfillment of the requirements for the Degree of  
Master of Science

**MATERIALS SCIENCE AND ENGINEERING**

Raleigh

1998

**APPROVED BY:**



Chair of Advisory Committee

## BIOGRAPHY

Abdül Özgür Erolat was born on February 16, 1973 in Ankara, Turkey. After attending primary school in Turkey for two years, he studied the third grade in San Diego, CA. Upon returning to Turkey, he completed his primary, secondary and high school at TED Ankara College. In the Fall of 1992, he started his undergraduate studies in the Department of Metallurgical and Materials Engineering at Middle East Technical University (METU) in Ankara, Turkey. He spent his sophomore year in the Department of Materials Science and Engineering at North Carolina State University (NCSU) and returned to METU after a year to complete his undergraduate studies and received his B.S. degree (Spring 1996). He

*To my loving parents,*

*Güzin Erolat*

*&*

*Halûk Erolat*

## BIOGRAPHY

Ahmet Gün Erlat was born on February 16, 1975 in Ankara, Turkey. After attending primary school in Turkey for two years, he studied the third grade in San Diego, CA. Upon returning to Turkey, he completed his primary, secondary and high school at TED Ankara College. In the Fall of 1992, he started his undergraduate studies in the Department of Metallurgical and Materials Engineering at Middle East Technical University (METU) in Ankara, Turkey. He spent his sophomore year in the Department of Materials Science and Engineering at North Carolina State University (NCSU) and returned to METU after a year to complete his undergraduate studies and receive his bachelors degree (Spring 1996). He is now continuing his education and is a masters candidate in the Department of Materials Science and Engineering at NCSU.

In addition, a number of fellow scientists and students on NCSU campus have contributed to this project, which is greatly appreciated. Of these, first I thank Dr. Do-Chy Wang who helped me better understand the subject and never got tired of answering my questions, even from Pittsburgh. I am grateful to Jonathan Lauer for his never ending patience and support. Also, I would like to thank Donovan Leonard and Dale Bachelor for their help with the Atomic Force Microscope. In addition, my gratitude goes to Dan Leonard, Archie Paul Smith, Kai Young, Michelle Arnold and many others, who have been a great help.

I would like to thank a special person, Ms. Edna Deas, who, beginning from my undergraduate year at NCSU, has always believed in me and has always been there for me.

I would especially like to thank my family: my parents Gülsin and Haluk Erlat, my uncles Zeki, Erol and Erhan Gülsin, my aunt Jale Erlat and my grandmother Türkan Erlat. Without their love and support, none of this would have been possible. Also, I would like

## ACKNOWLEDGMENTS

It has been my pleasure to have worked under the direction of Dr. Richard J. Spontak. I thank him for the financial and emotional support he has given me throughout this project as well as the insight he has provided. I would also like to thank my other advisory committee members, Dr. Benny Freeman and Dr. Zlatko Sitar for their support.

My appreciation goes to Becton Dickinson Technologies (BDT), who have financially supported this project and also have permitted access to their facilities. In addition I am grateful to our fellow researchers at BDT, especially Dr. Erwin A. Vogler, Richard P. Clarke and Dr. Yelena Tropsha, for countless hours of insightful discussions and their encouragement. I would also like to thank Perry Haaland, Tommy Robinson, David Montgomery, Noel Harvey, Kevin Mar and Jane Graper from BDT for their valuable assistance.

In addition, a number of fellow scientists and students on NCSU campus have contributed to this project, which is greatly appreciated. Of these, first I thank Dr. Bo-Chy Wang who helped me better understand the subject and never got tired of answering my questions, even from Pittsburgh. I am grateful to Jonathan Laurer for his never ending patience and support. Also, I would like to thank Donovan Leonard and Dale Batchelor for their help with the Atomic Force Microscope. In addition, my gratitude goes to Dan Leonard, Archie Paul Smith, Kit Yeung, Michelle Arnold and many others, who have been a great help.

I would like to thank a special person, Ms. Edna Deas, who, beginning from my undergraduate year at NCSU, has always believed in me and has always been there for me.

I would especially like to thank my family: my parents Güzin and Haluk Erlat, my uncles Zeki, Erol and Erden Gülsoy, my aunt Jale Erlat and my grandmother Türkan Erlat. Without their love and support, none of this would have been possible. Also, I would like

to thank one very special person, my grandfather Basri Gülsoy, who will live in my heart forever.

Finally, I am grateful to my friends for standing by me no matter what. I thank Ferhat Fenercioglu, the man of multiple skills, Caglar Unlüdag, Orkun Gücük and all my friends for their support. Lastly, my gratitude and love goes to the sweetest, the most generous, thoughtful and beautiful person, Zeynep Kesler.

1.2	Industrial Needs and Applications	2
1.3	Gas Permeation and SiO <sub>2</sub> -Coated Polymers	4
1.3.1	Permeation and Activated Rate Theory	6
1.3.2	Permeation Studies of Polymer/SiO <sub>2</sub> Laminates	8
1.4	Effect of Thickness	11
1.5	Morphological Characteristics of SiO <sub>2</sub> Coatings	11
1.5.1	Atomic Force Microscopy	12
1.5.1.1	Atomic Force Microscopy of SiO <sub>2</sub> Coatings	13
1.6	Deposition Techniques	15
1.6.1	Plasma-enhanced Chemical Vapor Deposition	15
1.6.2	Comparison of SiO <sub>2</sub> Deposition Techniques	17
1.7	Chemical Characteristics of SiO <sub>2</sub> Coatings	18
1.8	Mechanical Characteristics of SiO <sub>2</sub> Coatings	20
1.9	Organization of Thesis	22
	References	23
2	EXPERIMENTAL	36
2.1	Film Deposition	36
2.1.1	Radio Frequency Discharge PECVD	36
2.1.2	Magnatron PECVD	36
2.2	Oxygen Transmission Measurements	37
2.3	Water Vapor Transmission Measurements	38
2.4	Atomic Force Microscopy	39
2.5	Transmission Electron Microscopy	40

## TABLE OF CONTENTS

LIST OF TABLES	ix
LIST OF FIGURES	x
1. LITERATURE REVIEW	1
1.1 Introduction	1
1.2 Industrial Needs and Applications	2
1.3 Gas Permeation and SiO <sub>x</sub> -Coated Polymers	4
1.3.1 Permeation and Activated Rate Theory	6
1.3.2 Permeation Studies of Polymer/SiO <sub>x</sub> Laminates	8
1.4 Effect of Thickness	11
1.5 Morphological Characteristics of SiO <sub>x</sub> Coatings	11
1.5.1 Atomic Force Microscopy	12
1.5.1.1 Atomic Force Microscopy of SiO <sub>x</sub> Coatings	13
1.6 Deposition Techniques	15
1.6.1 Plasma-enhanced Chemical Vapor Deposition	15
1.6.2 Comparison of SiO <sub>x</sub> Deposition Techniques	17
1.7 Chemical Characteristics of SiO <sub>x</sub> Coatings	18
1.8 Mechanical Characteristics of SiO <sub>x</sub> Coatings	20
1.9 Organization of Thesis	22
References	23
2. EXPERIMENTAL	36
2.1 Film Deposition	36
2.1.1 Radio Frequency Discharge PECVD	36
2.1.2 Magnetron PECVD	36
2.2 Oxygen Transmission Measurements	37
2.3 Water Vapor Transmission Measurements	38
2.4 Atomic Force Microscopy	39
2.5 Transmission Electron Microscopy	40

2.6	Thickness and Refractive Index Measurements	41
	References	42
3.	SiO <sub>x</sub> GAS BARRIER COATINGS ON POLYMER SUBSTRATES : MORPHOLOGY AND THE GAS TRANSPORT MECHANISM	51
3.1	Introduction	51
3.2	Experimental	53
	3.2.1 Material Processing	53
	3.2.2 Material Characterization	54
3.3	Results & Discussion	55
	3.3.1 Process parameters	55
	3.3.2 Morphological Characteristics	59
	3.3.3 Permeation Mechanism	63
3.4	Conclusions	68
	References	70
4.	EFFECT OF PECVD CONDITIONS ON THE MORPHOLOGY AND GAS BARRIER PROPERTIES OF SiO <sub>x</sub> COATINGS ON POLYCARBONATE	85
4.1	Introduction	85
4.2	Experimental	86
	4.2.1 Material Processing	86
	4.2.2 Material Characterization	87
4.3	Results and Discussion	88
	4.3.1 Deposition Time	88
	4.3.2 Deposition Power	90
	4.3.3 Deposition Pressure	94
	4.3.4 Gas Flow Rate	96
	4.3.5 Permeation Mechanism	99
4.4	Conclusions	102
	References	104
5.	CONCLUDING REMARKS AND FUTURE WORK	128
5.1	Concluding Remarks	128
	5.1.1 PC/SiO <sub>x</sub> Series	128
	5.1.2 PET/SiO <sub>x</sub> Series	130
5.2	Future Work	132

## LIST OF TABLES

## 6. BIBLIOGRAPHY

Table 1.1	Permeabilities of various gases and vapors through different silica glasses	5
Table 1.2	Permeability coefficients of various polymers	6
Table 3.1	Magnetron-PECVD deposition settings obtained from the NPSM optimization	56
Table 3.2	$\Delta G^{\circ}_{O_2}$ data	64

## LIST OF TABLES

Figure 1.1	A defect model for $\text{SiO}_2$ gas transport by Feltz	30
Table 1.1	Permeabilities of various gases and vapors through different silica glasses	5
Figure 1.2	Model of $\text{O}_2$ transport proposed by Tropsha and Harvey	
Table 1.2	Permeability coefficients of various polymers well as a widely used barrier material for PET	6
Figure 1.3	Dependence of $\Delta G^\ddagger_{\text{O}_2}$ on $\text{SiO}_2$ stoichiometry	32
Table 3.1	Magnetron-PECVD deposition settings obtained from the NPRSM optimization.	56
Figure 1.4	Dependence of $\Delta G^\ddagger_{\text{O}_2}$ on $\text{SiO}_2$ stoichiometry as applied to commercial applications	33
Table 3.2	$\Delta G^\ddagger_{\text{O}_2}$ data	64
Figure 1.5	$\Delta G^\ddagger_{\text{O}_2}$ stoichiometry on barrier performance shown both in terms of (a) dependence of $\Delta G^\ddagger_{\text{O}_2}$ on $x$ (reproduced from the data of Krug <sup>20</sup> ) and (b) the glassy network of $\text{SiO}_2$	34
Figure 1.6	Dependence of transparency attainable on $\text{SiO}_2$ stoichiometry for PET.	35
Figure 2.1	Schematic illustration of the radio-frequency (RF) discharge PECVD system employed as a part of this study to produce $\text{SiO}_2$ thin coatings on a polycarbonate (PC) substrate.	43
Figure 2.2	Schematic diagram of the Magnetron Plasma Deposition System used here to deposit $\text{SiO}_2$ on PET substrates.	44
Figure 2.3	Simplified schematic showing the operating principle of the Ox-Tran 2/20 oxygen transmission rate measurement system.	45
Figure 2.4	Flow diagram of the water vapor transmission rate measurement system	46
Figure 2.5	Schematic illustration demonstrating the operation of an Atomic Force Microscope.	47
Figure 2.6	Illustrations of the Castaing-Henry-Ottensmeyer energy filter in the Zeiss EM802 microscope.	48
Figure 2.7	Sample preparation method showing the necessary steps taken to isolate the $\text{SiO}_2$ films.	49
Figure 2.8	Schematic illustration of the Rudolph Ellipsometer system employed in this study for thickness and refractive index measurements of $\text{SiO}_2$ coatings on Si substrates.	50
Figure 3.1	Schematic illustration of the Magnetron Plasma Deposition System.	74
Figure 3.2a	Contour plots resulting from the Non-Parametric Response Surface (NPRSM) optimization in which $\text{O}_2$ flow rate is held constant at 6.5 sccm.	75
Figure 3.2b	Contour plots resulting from the Non-Parametric Response Surface Methods (NPRSM) optimization in which the HMDSO flow rate is held constant at 15.5 sccm.	76

## LIST OF FIGURES

Figure 1.1	A defect model for SiO <sub>x</sub> coatings proposed by Felts.	30
Figure 1.2	Empirical model of O <sub>2</sub> transport proposed by Tropsha and Harvey.	31
Figure 1.3	A general overview of the PECVD process, as well as a widely used cold wall parallel-plate PECVD reactor.	32
Figure 1.4	Chronological development of PECVD as applied to commercial applications.	33
Figure 1.5	Effect of Si:O stoichiometry on barrier performance shown both in terms of the (a) dependence of $\Pi_{O_2}$ on $x$ (reproduced from the data of Krug <sup>20</sup> ) and (b) the glassy network of SiO <sub>2</sub> .	34
Figure 1.6	Dependence of transparency attainable on SiO <sub>x</sub> stoichiometry for PET.	35
Figure 2.1	Schematic illustration of the radio frequency (RF) discharge PECVD system employed as a part of this study to produce SiO <sub>x</sub> thin coatings on a polycarbonate (PC) substrate.	43
Figure 2.2	Schematic diagram of the Magnetron Plasma Deposition System used here to deposit SiO <sub>x</sub> on PET substrates.	44
Figure 2.3	Simplified schematic showing the operating principle of the Oxtran 2/20 oxygen transmission rate measurement system.	45
Figure 2.4	Flow diagram of the water vapor transmission rate measurement system	46
Figure 2.5	Schematic illustration demonstrating the operation of an Atomic Force Microscope.	47
Figure 2.6	Illustrations of the Castaing-Henry-Ottensmeyer energy filter in the Zeiss EM902 microscope.	48
Figure 2.7	Sample preparation method showing the necessary steps taken to isolate the SiO <sub>x</sub> films.	49
Figure 2.8	Schematic illustration of the Rudolph Ellipsometer system employed in this study for thickness and refractive index measurements of SiO <sub>x</sub> coatings on Si substrates.	50
Figure 3.1	Schematic illustration of the Magnetron Plasma Deposition System.	74
Figure 3.2a	Contour plots resulting from the Non-Parametric Response Surface (NPRSM) optimization in which O <sub>2</sub> flow rate at 6.5 sccm.	75
Figure 3.2b	Contour plots resulting from the Non-Parametric Response Surface Methods (NPRSM) optimization in which the HMDSO flow rate is held constant at 15.5 sccm.	76

Figure 3.2c	Contour plots resulting from the Non-Parametric Response Surface Methods (NPRSM) optimization in which the deposition power is held constant at 65 W.	77
Figure 3.3	Variation of the water vapor transmission rate ( $\Pi_{H_2O}$ ) with oxygen transmission rate ( $\Pi_{O_2}$ ) on double-logarithmic coordinates for $SiO_x$ -coated PET in which the $SiO_x$ layer is derived from (a) HMDSO and (b) TMS monomer.	78
Figure 3.4	Series of atomic force microscopy (AFM) images obtained in tapping mode from $SiO_x$ coatings exhibiting different levels of barrier performance.	79
Figure 3.5	Values of the rms surface roughness obtained from the AFM images in Fig. 4 and presented here as a function of $\Pi_{O_2}$ on semi-logarithmic coordinates.	80
Figure 3.6	Energy-filtered (zero-loss) TEM images of a good $SiO_x$ barrier coating ( $\Pi_{O_2} = 0.48 \text{ cm}^3/\text{m}^2\text{-atm-day}$ : left) in comparison to a poor barrier ( $\Pi_{O_2} = 7.8 \text{ cm}^3/\text{m}^2\text{-atm-day}$ : right)	81
Figure 3.7	Dependence of (a) oxygen transmission rate ( $\Pi_{O_2}$ ) and (b) water vapor transmission rate ( $\Pi_{H_2O}$ ) on reciprocal temperature for four $SiO_x$ coatings produced under various conditions to yield different barrier performance, compared in terms of $\Pi_{O_2}$ at 30°C (in $\text{cm}^3/\text{m}^2\text{-atm-day}$ ): 0.18 (●), 1.6 (▲), 16 (○) and 80 (PET, Δ).	82
Figure 3.8	Dependence of the activation energy for $H_2O$ transport ( $\Delta G^\ddagger_{H_2O}$ ) on $SiO_x$ barrier performance.	83
Figure 3.9	Variation of $\psi_o [= \Pi_o \exp(\Delta S^\ddagger/R)]$ for $O_2$ permeation with $SiO_x$ barrier performance ( $\Pi_{O_2}$ ) suggesting a correlation between $\Delta S^\ddagger$ , a measure of defect size/density, and barrier quality.	84
Figure 4.1	Schematic illustration of the radio frequency (RF) discharge PECVD system employed as a part of this study to produce $SiO_x$ thin coatings on a polycarbonate (PC) substrate.	108
Figure 4.2	Variation of $SiO_x$ coating thickness with deposition time demonstrating that the relationship is nearly linear (solid line) when all other PECVD parameters are held constant.	109
Figure 4.3	Dependence of $O_2$ transmission rate ( $\Pi$ ) on $SiO_x$ coating thickness at constant power, pressure, HMDSO and $O_2$ flow rates (100 W, 16 Pa, 2.5 sccm and 70 sccm, respectively).	110
Figure 4.4	3-D AFM images of acquired from $SiO_x$ coatings at four different deposition times (in sec): (a) 10, (b) 40, (c) 80, (d) 120.	113

Figure 4.5	Oxygen transmission rate ( $\Pi$ ) presented as a function of deposition power at a pressure of 16 Pa, deposition time of 120 s, and flow rates of 2.5 (HMDSO) and 70 ( $O_2$ ) sccm.	114
Figure 4.6	Dependence of $SiO_x$ coating thickness from ellipsometry on PECVD power level under the conditions listed in the caption of Fig. 4.5.	115
Figure 4.7	Variation of refractive index ( $n$ ) with deposition power for the same series described in the caption of Fig. 4.5.	116
Figure 4.8	Tapping Mode AFM images acquired from $SiO_x$ coatings under the conditions listed in the caption of Fig. 4.5 at four different power levels (in W): (a) 10, (b) 20, (c) 60, (d) 100.	117
Figure 4.9	Surface roughness from AFM images similar to those displayed in Fig. 4.8 as a function of deposition power.	118
Figure 4.10	Effect of system pressure on (a) the oxygen transmission rate ( $\Pi$ ) and (b) the $SiO_x$ coating thickness for three deposition times (expressed in s): 20 (○), 60 (●) and 120 (△).	119
Figure 4.11	Oxygen transmission rates ( $\Pi$ ) presented as functions of (a) HMDSO flow rate and (b) HMDSO/ $O_2$ ratio.	120
Figure 4.12	Dependence of $SiO_x$ coating thickness on HMDSO flow rate for four different $O_2$ flow rates (in sccm): 50 (○), 70 (●), 90 (△) and 110 (▲).	121
Figure 4.13	AFM images obtained from $SiO_x$ coatings produced under the conditions listed in the caption of Fig. 3.11 for (a) high and (b) low HMDSO flow rates at a constant $O_2$ flow rate of 70 sccm.	122
Figure 4.14	AFM images obtained from $SiO_x$ coatings produced under the conditions listed in the caption of Fig. 3.11 for (a) high and (b) low $O_2$ flow rates at a constant HMDSO flow rate of 2.5 sccm.	123
Figure 4.15	Oxygen transmission rate ( $\Pi$ ) shown as a function of reciprocal temperature for four $SiO_x$ coatings produced under varying flow rates: 1.5 sccm HMDSO (open symbols), 3.5 sccm HMDSO (filled symbols), 50 sccm $O_2$ (circles) and 70 sccm $O_2$ (triangles).	124
Figure 4.16	Dependence of the activation energy for $O_2$ transport ( $\Delta G^\ddagger$ ) on $SiO_x$ barrier performance (denoted here by the $O_2$ transmission rate, $\Pi$ , evaluated at 30°C).	125
Figure 4.17	Activation energy for $O_2$ transport ( $\Delta G^\ddagger$ ) shown as a function of $SiO_x$ coating thickness, revealing that $\Delta G^\ddagger$ increases almost linearly (solid line) with increasing thickness.	126

## 1. LITERATURE REVIEW

- Figure 4.18 Schematic representation of  $O_2$  transport through  $SiO_x$ -coated polymer substrates on the basis of the data in Figs. 4.16 and 4.17. Poor  $SiO_x$  coatings are either very thin (incomplete surface coverage) or consist of large defects (relative to the  $O_2$  molecule). 127
- Figure 5.1 Dependence of  $O_2$  transmission rate ( $\Pi$ ) on reciprocal temperature on semi-logarithmic coordinates, demonstrating that a physical laminate of two-single coated substrates yields a significant increase in activation energy ( $\Delta G^\ddagger$ , corresponding to the slope). 136
- Figure 5.2 FTIR absorbance at  $1070\text{ cm}^{-1}$  (corresponding to Si—O—Si stretching) as a function of HMDSO flow rate for four different  $O_2$  flow rate levels (in sccm): 50 (O), 70 ( $\Delta$ ), 90 ( $\square$ ), 110 ( $\blacklozenge$ ). 137
- Figure 5.3 Schematic diagram of a glass permeation cell designed to determine the size of defects in  $SiO_x$  through the use of different molecules as penetrants. 138

# 1. LITERATURE REVIEW

## 1.1 INTRODUCTION

Low-cost, high-volume (commodity) polymers have been employed extensively in a variety of packaging applications (primarily for food preservation, electronics isolation or vacuum containment) for several decades.<sup>1-3</sup> The relatively high permeability of these polymers to environmental gases (e.g., oxygen and water vapor) reduces their effectiveness (and product shelf life) due to the free (unoccupied) volume inherent<sup>4</sup> in most thermoplastic macromolecules (selected due to their processability). Early,<sup>5</sup> as well as more recent,<sup>6</sup> attempts to overcome this shortcoming have sought to employ molecular engineering to reduce this free volume through the development of novel microstructured polymers. Unfortunately, economic considerations have thus far precluded the commercial viability of materials exhibiting sufficient barrier performance. Development of inorganically modified (e.g., aluminized) polymers has satisfied<sup>7-9</sup> the need for high-barrier polymers, but the route by which these materials are manufactured is not optimal.<sup>8</sup> Advances in deposition techniques have now provided new solutions to this challenge,<sup>10</sup> recently leading to the commercial production of polymer films modified with a thin inorganic surface coating of either  $Al_xO_y$  or  $SiO_x$ . Such laminated composites exhibit the desirable barrier properties of the inorganic constituent, but retain the fracture resistance of the polymer substrate.

The present work explores the factors governing the barrier efficacy of  $SiO_x$  coatings deposited on commodity polymer substrates. Over the past decade, numerous improvements have been realized in depositing such coatings at the production (industrial) and laboratory (research) scales. Both fundamental and applied studies have been conducted to investigate various aspects of this emerging technology, focusing on either (i) enhancing the capabilities of various deposition techniques, or (ii) analyzing the processing and/or material characteristics of  $SiO_x$ -coated polymer laminates. More specifically, such

efforts seek to elucidate and correlate the effects of deposition techniques on barrier performance, polymer and coating chemistry, morphological features of the  $\text{SiO}_x$  coating, and the mechanism of gas transport through polymer/ $\text{SiO}_x$  composites. These factors cannot be considered separately, since they are all intimately, and sometimes synergistically, coupled. The next section provides an overview of studies reported in the open (not patent) literature, and is followed by detailed descriptions of the factors listed above and methods by which these factors can be systematically manipulated or characterized.

## 1.2 INDUSTRIAL NEEDS AND APPLICATIONS

Two major industries that produce commercial devices requiring high impermeability to environmental gases (to protect the device contents) are the food packaging and medical device industries. In this section, the use of  $\text{SiO}_x$  coatings deposited on polymers for such applications is presented and discussed by comparing these coatings with other barrier materials that are presently available on a commercial basis.

The principal materials presently employed in food packaging include aluminum foil, laminates of poly(ethylene terephthalate) (PET) or oriented polypropylene (OPP) with poly(vinylidenechloride) (PVDC), and co-extruded layers of ethylvinyl alcohol (EVOH), acrylics and aluminum.<sup>7,8</sup> All these materials possess different shortcomings, therefore leading to the following reasons in support of inorganic coatings ( $\text{SiO}_x$ ) on polymer substrates for packaging applications:

- Gas (mainly oxygen and water vapor) barrier properties (to improve shelf life)<sup>11</sup>
- Ecological considerations (to promote product recyclability)<sup>8,12,13</sup>
- Transparency (to ensure content visibility)
- Retortability (to permit pressure cooking)<sup>14,15</sup>
- Microwavability (to avoid radiation damage)

The superiority of  $\text{SiO}_x$  glass over any known organic polymer in barrier performance

can be attributed to two common features of inorganic glasses: (i) very constricted spaces (i.e., little free volume) within the Si-O lattice, and (ii) a broad range of thermal stability.<sup>16-19</sup> However, the main competition for this technology remains Al-based films and coatings, which have saturated the market since 1964.<sup>20</sup> Coatings of this nature are known to extend product shelf-life, but comparable improvement in barrier performance is likewise obtained<sup>21</sup> through the use of deposited SiO<sub>x</sub> surface coatings. One obvious problem of Al-based packaging materials lies in their opacity, which prevents examination of the package contents. In many cases, transparency constitutes an important consideration in packaging, and commercial SiO<sub>x</sub> coatings are more than 90% transparent.<sup>22</sup> A more serious problem associated with the use of PVDC is that this material releases potential carcinogens into food,<sup>8,12</sup> as well as hydrochloric acid upon incineration,<sup>12</sup> thereby posing non-negligible health concerns. Another environmental issue is that laminates formed from different polymers cannot be easily recycled, whereas a sandwich layer of OPP/SiO<sub>x</sub>/OPP (final package form) can be re-extruded without significant loss of clarity or other barrier properties.<sup>13</sup> Lastly, the processing of SiO<sub>x</sub>/polymer laminates into final packaging products can be accomplished by several different routes<sup>23</sup> (e.g., solvent, aqueous or solventless adhesive lamination; extrusion lamination; extrusion and co-extrusion), thereby imparting desirable manufacturing flexibility.

In addition to the food packaging industry, the recent move in the medical community to substitute polymer/SiO<sub>x</sub> composite materials for glass has become a crucial consideration in the high-volume production of disposable devices, such as blood collection tubes, blood culture bottles and pre-filled syringes. The two critical requirements for such devices are transparency and impermeability. Transparency is requisite since medical staff must be able to visually and spectroscopically monitor the device contents. Impermeability is needed to prevent loss of vacuum in these devices so that the contents (including vacuum in the blood collection tubes) are not prematurely degraded by exposure to atmospheric gases. Traditionally, these devices have been manufactured from glass, which possesses both

medical requirements. Since glass can easily shatter upon impact and endanger the safety of medical personnel as well as patients, however, the medical industry is seeking to replace glass with tough commodity polymers in the production of such devices. In this conversion, however, an obvious, but unacceptable, trade-off is made in terms of impermeability. The solution to this problem lies in the deposition of a very thin layer of transparent inorganic coating on the polymer surface, thereby enhancing the barrier quality of the polymer without inducing embrittlement or an increase in opacity.<sup>22</sup> The transparency of the polymer/SiO<sub>x</sub> composite material is retained by using either amorphous (glassy) polymers (e.g., polycarbonate or polymethyl methacrylate) or nucleated semi-crystalline polymers<sup>24,25</sup> (e.g., PET or polypropylene).

### 1.3 GAS PERMEATION AND SiO<sub>x</sub>-COATED POLYMERS

As stated in the previous section, the most important reason for depositing SiO<sub>x</sub> thin layers on polymer substrates is the superior gas barrier efficacy afforded by this inorganic glass. The barrier characteristics of silicon oxide glasses have been studied<sup>26,27</sup> extensively, and the material properties responsible for such behavior are (i) the constricted interstitial spaces between Si and O atoms in the lattice,<sup>18,19</sup> and (ii) a broad thermal stability range.<sup>16,17,26</sup> The latter reflects the importance of a constant lattice, to avoid thermal stress build-up and eventual cracking, over a range of application temperatures (particularly in the vicinity of ambient temperature). The relative barrier efficacy of different silica glasses, including annealed silicon oxide,<sup>28</sup> microporous glass<sup>29</sup> and vitreous silica<sup>30</sup> can be ascertained from the permeabilities of various gases through them, as shown in Table 1.1.

**Table 1.1** Permeabilities (expressed in terms of mBa) of Various Gases and Vapors Through Different Silica Glasses

Gas	Annealed Silica <sup>28</sup>	Microporous Glass <sup>29</sup>	Vitreous Silica <sup>30</sup>
O <sub>2</sub>		1	0.9
He	61	9	-
Ne	0.04	-	-
Ar	7	-	-

On the other hand, the barrier properties of the polymers are dictated primarily by the inherent free volume.<sup>4</sup> Unlike molecularly rigid silicon oxides, the chain structure of polymers is dynamic, subject to thermal fluctuations and chain dynamics.<sup>31</sup> As a result of thermally dependent interchain interactions (most notably hydrogen bonding) and chain mobility, short-lived interstitial spaces varying in size and geometry are created, through which penetrant molecules diffuse. Here, we consider only simple penetrant molecules (e.g., the environmental gases O<sub>2</sub> and water vapor), and neglect the more complex ones capable of exhibiting segmental motion (and, hence, reptative diffusion).<sup>32</sup> Thermal and processing history also play important roles in the development of gas barrier properties in polymers. Since many commodity polymers, such as PET, OPP, nylon and cellophane, are employed in various packaging applications, their permeabilities (P) are of general interest and are presented for comparison in Table 1.2. It should be noted here that the most commonly used<sup>21</sup> substrates for SiO<sub>x</sub> deposition are the semi-crystalline polymers PET and OPP, typically ranging in thickness from 12 to 25 μm.

### 1.3.1 Permeation and Activated Rate Theory

The permeability coefficient of a gas or vapor through a homogeneous polymer membrane is defined as

**Table 1.2 Permeability Coefficients of Various Polymers<sup>33</sup>**

Polymer	Temperature (°C)	$P_{O_2} \times 10^{13}$ [cm <sup>3</sup> (STP)-cm/cm <sup>2</sup> -s-Pa]
PET (Mylar A)	25	0.03
PP	33	1.28
Nylon (Nylon 6)	30	0.0285
Cellophane	25	0.00536
PC (Lexan)	25	1.05
PMMA	34	0.116
PS (biaxially oriented)	25	2.0
HDPE	25	0.3
LDPE	25	2.2
PVDC (Saran)	30	0.00383

In light of these polymer material considerations, the importance of depositing thin (10–200 nm thick) SiO<sub>x</sub> coatings on polymer substrates for food and electronics packaging, as well as biomedical device fabrication, is evident. As mentioned earlier, various factors including coating thickness, chemistry, morphology and deposition conditions influence the resultant barrier properties in a highly coupled fashion. While these factors will be explored in turn in subsequent sections of this chapter, attention is first focused on the mechanism of ideal gas permeation, as described by activated rate theory, through such composite films.

### 1.3.1 Permeation and Activated Rate Theory

The permeability coefficient of a gas or vapor through a homogeneous polymer membrane is defined as

$$P = Q/At\Delta p \quad (1.1)$$

where Q represents the amount (volume or mass) of gas under specified conditions, l is the film thickness, A is the film surface area, t is time and  $\Delta p$  denotes the driving pressure. It is interesting to find that 29 different units have been reported in the literature for P! The most common of these is the Barrer, given by  $10^{-10} \text{ cm}^3(\text{STP})\text{-cm/cm}^2\text{-sec-cm Hg}$ . An alternate expression providing a measure of gas transport through a polymer under steady-state conditions is the gas transmission rate ( $\Pi$ ), generally expressed in units of  $\text{cm}^3(\text{STP})/\text{m}^2\text{-atm-day}$ ,  $\text{cm}^3/100 \text{ in}^2\text{-atm-day}$  or  $\text{mol/m}^2\text{-atm-sec}$ , is given by

$$\Pi = P/l \quad (1.2)$$

In literature studies comparing the barrier performance of polymer/SiO<sub>x</sub> composites,  $\Pi$  rather than P is often employed.<sup>10,34</sup> For the sake of consistency,  $\Pi$  is likewise used in the present work.

For laminate films or multilayered structures composed of n parallel layers all oriented normal to the direction of transport, gas transmission in the absence of edge (or boundary) effects can be expressed by the following expression:

$$\Pi = [l_1/\Pi_1 + l_2/\Pi_2 + l_3/\Pi_3 + \dots + l_n/\Pi_n]^{-1} \quad (1.3)$$

where  $l_i$  and  $\Pi_i$  correspond to the thickness and gas transmission rate of layer i, respectively. The framework yielding Eq. 1.3, referred to as the ideal laminate theory,<sup>34-39</sup> assumes that each layer is homogeneous and defect-free, which, as will be discussed later, is certainly not the case for SiO<sub>x</sub> coatings. Poor coatings contain macroscopic defects (e.g., pinholes),<sup>35,38</sup> whereas superior (low- $\Pi$ ) coatings consist of nanoscale defects.<sup>39-41</sup> General activated rate theory nonetheless serves as a valuable method of analyzing these defects and elucidating the mechanism governing gas transport through SiO<sub>x</sub> coatings. The basis of activated rate theory lies in the temperature dependence of  $\Pi$ , which, for transport through inorganic glasses<sup>28,42</sup> and glassy polymers,<sup>32</sup> can be expressed by an Arrhenius-type equation of the form

$$\Pi = \Pi_0 \exp(-\Delta G^\ddagger/RT) \quad (1.4)$$

where  $\Pi_0$  is a constant,  $\Delta G^\ddagger$  is the apparent activation energy,  $R$  is the universal gas constant and  $T$  denotes absolute temperature. While  $\Delta G^\ddagger$  has been adopted for use throughout this study, other notations (e.g.,  $E_p$ ,  $\Delta E_p$  and  $\Delta E$ ) are widely used in the literature. The rate-limiting step for gas transmission through a polymer coated with  $\text{SiO}_x$  is determined by the component (polymer substrate or  $\text{SiO}_x$  coating) possessing the highest value of  $\Delta G^\ddagger$ . In the next section, studies aimed at using gas transmission rates through  $\text{SiO}_x$  thin films to discern the corresponding mechanism governing such molecular transport will be discussed.

### 1.3.2 Permeation Studies of Polymer/ $\text{SiO}_x$ Laminates

The two principal environmental permeants examined extensively over the last decade are  $\text{O}_2$  and water vapor. Since the first commercialization of  $\text{SiO}_x$  coatings in the mid-1980's, values of oxygen and water vapor transmission rates ( $\Pi_{\text{O}_2}$  and  $\Pi_{\text{H}_2\text{O}}$ , respectively) have been reported<sup>10, 43</sup> for  $\text{SiO}_x$  coatings produced on different polymer substrates by various deposition techniques, which will be discussed further in a subsequent section. Apart from the bulk film properties mentioned in the introduction, the microstructure of these coatings (expressed in terms of defects) and its effect on barrier performance have only recently become the subject of in-depth investigation.

The first significant barrier values due to  $\text{SiO}_x$  surface deposition were reported by Chahroudi,<sup>15</sup> who obtained a  $\Pi_{\text{O}_2}$  of  $0.1 \text{ cm}^3/100 \text{ in}^2\text{-atm-day}$  for PET/ $\text{SiO}_x$ . This compared surprisingly well with  $\Pi_{\text{O}_2}=0.03\text{--}0.15 \text{ cm}^3/100 \text{ in}^2\text{-atm-day}$  aluminized PET. Likewise, a  $\Pi_{\text{H}_2\text{O}}$  of  $0.08 \text{ g}/100 \text{ in}^2\text{-day}$  from PET/ $\text{SiO}_x$  laminates compared favorably against  $0.04\text{--}0.15 \text{ g}/100 \text{ in}^2\text{-day}$  from PET/Al analogs. Initially, values of  $\Pi_{\text{O}_2}$  less than  $1 \text{ cm}^3/\text{m}^2\text{-atm-day}$  and of  $\Pi_{\text{H}_2\text{O}}$  less than  $0.3 \text{ g}/\text{m}^2\text{-day}$  were acceptable for industrial purposes. In one of the first attempts to relate  $\text{SiO}_x$  microstructure to barrier performance, Krug<sup>20</sup> proposed that oxygen transmission occurs primarily through *pin windows*, which he defined as bare (uncoated) surfaces on the film surface. Felts,<sup>44</sup> however, first proposed

the possibility of defects in the  $\text{SiO}_x$  structure and introduced a simplistic defect model, a schematic of which is presented in Fig. 1.1. He argued that the partial coverage advocated by Krug<sup>20</sup> could likewise arise from patches of insufficiently thick coating. Furthermore, he believed that the ultimate gas barrier performance of a given coating was dependent on the number and type of defects present, since  $\Pi_{\text{O}_2}$  never attained zero, as seen in Fig. 1.1. Hagenburgh<sup>45</sup> also reported impressive barrier improvement, which supported the presence of nanoscale coating defects. Mercea and Bartan<sup>46,47</sup> have examined the permeability of various gases (He,  $\text{H}_2$ , Ne, Ar, Kr, CO,  $\text{CH}_4$ ,  $\text{O}_2$ ,  $\text{N}_2$  and  $\text{CO}_2$ ) through PET on which a thin  $\text{SiO}_2$  coating measuring 100 nm thick was deposited. Their results also revealed that these gases permeate through defects of the  $\text{SiO}_2$  layer. Such defects were thought to exist mainly in the form of pinholes and fine cracks. They also suggested the presence of molecular diffusion pathways along the grain boundaries of  $\text{SiO}_2$  during its growth.

As is evident from the studies mentioned above, the presence of defects in  $\text{SiO}_x$  coatings has been recognized for providing the diffusive pathways responsible for gaseous transport. Only recently have systematic studies attempted to elucidate the molecular transport mechanism of  $\text{O}_2$  and water vapor through polymer/ $\text{SiO}_x$  composites. Tropsha and Harvey<sup>34</sup> obtained  $\Delta G^\ddagger$  measurements for  $\text{O}_2$  ( $\Delta G^\ddagger_{\text{O}_2}$ ) and water vapor ( $\Delta G^\ddagger_{\text{H}_2\text{O}}$ ) transmission through uncoated (virgin) PET, as well as through single- (PET/ $\text{SiO}_x$ ) and double- ( $\text{SiO}_x$ /PET/ $\text{SiO}_x$ ) laminates. Their results indicated that  $\Delta G^\ddagger_{\text{O}_2}$  for single-coated systems was, within experimental uncertainty, identical to that for uncoated PET ( $\Delta G^\ddagger_{\text{O}_2} = 29 \pm 4$  kJ/mol). In marked contrast, results acquired from PET with double-sided  $\text{SiO}_x$  coatings yielded an increase in  $\Delta G^\ddagger_{\text{O}_2}$  of 54 kJ/mol relative to uncoated PET. Moreover, the ratio of  $\Pi_{\text{O}_2}$  from PET/ $\text{SiO}_x$  laminates to that of  $\text{SiO}_x$ /PET/ $\text{SiO}_x$  composites, predicted to be 2 by the ideal laminate theory (Eq. 1.3), was experimentally discerned to be about 5.

On the basis of these results for  $\text{SiO}_x$ -coated polymers, they<sup>34</sup> proposed a molecular

transport model, illustrated in Fig. 1.2, in which they concluded that fine-scale defects in the  $\text{SiO}_x$  coating serve as physical barriers to diffusion (blocks). While oxygen molecules must traverse these blocks, the principal source of thermally activated transport was believed to occur through the polymer matrix. For the double-coated laminates, however, they were forced to concede that the rate-limiting barrier efficacy resulted from the  $\text{SiO}_x$  layer(s), despite imperfections in their coatings. These results are substantiated and extended to new regimes in subsequent chapters of the present study. Complementary  $\Pi_{\text{H}_2\text{O}}$  measurements by Tropsha and Harvey<sup>34</sup> revealed an increase in  $\Delta G^\ddagger_{\text{H}_2\text{O}}$ , but these values were independent of the substrate, implying that interactions between the water molecules (with their tendency to form hydrogen bonds) and the  $\text{SiO}_x$  coating dictated the energetics of molecular transport.

In the same vein as Tropsha and Harvey,<sup>34</sup> Roberts et al.<sup>39</sup> and Henry et al.<sup>48</sup> further investigated the mechanism of gas transport through PET/ $\text{SiO}_x$  composites differing in thickness through the use of  $\Pi_{\text{O}_2}$  (and consequently  $\Delta G^\ddagger_{\text{O}_2}$ ) measurements using He, Ne and Ar. Their high-resolution transmission electron microscopy (TEM), scanning electron microscopy (SEM) and atomic force microscopy (AFM) efforts yielded no evidence of pinholes or other macroscopic defects responsible for measured  $\Pi_{\text{O}_2}$  levels, and so they concluded that the characteristic defect size was less than 1.0 nm. Furthermore, they refined their estimate of defect (pore) size through application of Eq. 1.3. By comparing the kinetic diameters of their penetrant gases with the known pore sizes of various silica structures, they concluded that pores less than 0.27 nm in diameter exist (on the basis of their results using He). Larger pores ranging from 0.4 to 0.6 nm were calculated from the transport behavior of heavier gases. As will be seen in later chapters, direct TEM, in addition to similarly inferred, results obtained for superior  $\text{SiO}_x$  coatings in the present study are in excellent agreement with this latter pore size range. An insightful study of  $\text{SiO}_x$  coatings employing both theoretical modeling and in-depth morphological analysis was recently reported by Henry et al.,<sup>38</sup> who addressed the role of macroscopic defects in

marginal  $\text{SiO}_x$  barrier coatings.

#### 1.4 EFFECT OF THICKNESS

One of the most important considerations in the design of  $\text{SiO}_x$  coatings exhibiting superior barrier performance is the coating thickness, as is evident for simple laminate structures from the ideal laminate theory (Eq. 1.3). For polymer/ $\text{SiO}_x$  composites, the relationship between coating thickness and gas transmission (mostly oxygen and water vapor) becomes increasingly more complex, since the  $\text{SiO}_x$  layer is not homogeneous and consists of defects (pores) varying in size at the nanoscale.<sup>39-41</sup> This relationship, first explored by Felts,<sup>35,44</sup> is also displayed in Fig. 1.1 and reveals that the  $\Pi_{\text{O}_2}$  initially decreases with increasing coating thickness until a critical thickness is achieved (Regime I). Such behavior is linked to the fraction of polymer surface area covered by the coating during the initial stages of deposition (when  $\text{SiO}_x$  nucleation and growth transpires). Beyond this critical thickness (Regime II),  $\Pi_{\text{O}_2}$  behavior remains relatively invariant as a consequence of a superior barrier coating. However, as the thickness is increased further (Regime III), barrier performance is observed to degrade due to extensive exposure of the film to plasma, free-spanning of the web or a build-up of internal stresses in the coating (resulting in cracking when released).

#### 1.5 MORPHOLOGICAL CHARACTERISTICS OF $\text{SiO}_x$ COATINGS

Morphological studies performed to discern the effect of  $\text{SiO}_x$  morphology on barrier efficacy have employed optical interferometry, SEM, TEM and, most recently, AFM. Cross-sectional SEM demonstrates that high-quality barrier coatings tend to exhibit a layered consistency and uniform deposition. In addition, Phillips<sup>49</sup> and Roberts et al.<sup>39</sup> have shown that pinholes and other macroscopic defects are absent in such coatings. Apart from these few studies, SEM has served primarily as a tool to measure coating thickness directly on polymer substrates (other techniques, such as ellipsometry, require a model substrate, such as Si, for such measurement). Few cross-sectional TEM studies have been

conducted to date due to difficulties in specimen preparation (by ultramicrotomy). Reported results have, for the most part, served the same purpose as cross-sectional SEM due to the relatively poor statistics associated with such defect analysis. Since no evidence of defects could be observed by Henry et al.<sup>48</sup> in their high-resolution cross-sectional TEM analysis, they infer that the pores must be 1 nm or less. Direct visualization of these defects has been achieved in the present work through the use of planar TEM, in which defect sizes and populations could be unambiguously ascertained. Since the SiO<sub>x</sub> coatings exist as thin surface films, AFM is ideally suited for the characterization of such coatings. While SEM and TEM are firmly established analytical techniques, AFM has only received proper credit over the last decade or so. Therefore, before discussing reported AFM results of SiO<sub>x</sub> coatings, an introduction to the technique is deemed essential for the reader and is provided in the following section.

### 1.5.1 Atomic Force Microscopy

Invention of scanning tunneling microscopy (STM) by Binnig and Rohrer<sup>50</sup> opened a previously closed path for researchers to image surface features (including individual surface atoms) at very high spatial resolution. The success of the STM led to the development of one of the most important types of *scanned probe* microscopies, namely atomic force microscopy (AFM).<sup>51-53</sup> The basic operating premise of AFM involves imaging a surface through the use of interatomic forces (not current) between a sharp tip (composed of, e.g., Si<sub>3</sub>N<sub>4</sub>) and the sample surface. This feature of AFM, unlike STM, permits examination of electrically non-conducting, as well as conducting, surfaces. In an AFM microscope, the tip is connected to an oscillating cantilever beam, which facilitates acquisition of phase, height and 3-D images of the surface, as well as measurement of surface roughness at the nanometer scale. There are two common modes of operation in AFM, namely, contact and tapping mode.<sup>53</sup> In contact mode, the first established mode of operation for AFM, the tip comes in physical contact with the surface of interest, and tip-

sample interactions consequently determine the acquired images.

This technique is suitable for analysis of hard surfaces, such as diamond or silicon (Si) wafers, but is highly problematic for soft (polymers)<sup>54</sup> and fragile ( $\text{SiO}_x$ ) materials.<sup>55</sup> Irreversible plastic deformation of such soft and fragile surfaces is commonly introduced by the tip due to a thin water monolayer present on the surface, which promotes adhesive capillary forces, when AFM is performed under ambient atmospheric conditions.<sup>56</sup> To prevent this deleterious effect, non-contact (tapping) mode AFM has been developed.<sup>57</sup> In this mode, the tip is rapidly vibrated in the vicinity of the surface, minimizing tip-sample interactions (responsible for surface deformation). Image information is obtained from long-range forces such as Van der Waals and electrostatic forces, which modify the spring constant and thus the resonant frequency of the spring attached to the cantilever beam. This solution to the problems initially associated with AFM has been extended by increasing the energy stored in the oscillating system so that the tip may be permitted to touch the surface at its lowest point during each vibrational cycle. Emerging AFM imaging techniques exploit such tip-surface contact to discriminate between phases or defects on the basis of local mechanical properties of the surface.<sup>56,58</sup>

#### **1.5.1.1 Atomic Force Microscopy of $\text{SiO}_x$ Coatings**

Initial surface morphology studies of  $\text{SiO}_x$  coatings were performed by optical interferometry,<sup>59</sup> which lacks the high magnification and sensitivity attainable by AFM. Characterization of  $\text{SiO}_x$  coatings by AFM has focused<sup>34,48,49,59-62</sup> on correlating the effect of surface morphology (topography), growth mechanism and root-mean-square (rms) surface roughness with the barrier performance (gas permeation) of these coatings. In addition, recent efforts have been directed toward identification of macroscopic and microscopic coating defects believed to be responsible for variable barrier quality. Phillips et al.<sup>49</sup> demonstrated that improved barrier coatings were obtained with smoother  $\text{SiO}_x$  surfaces. Benmalek<sup>60</sup> explored the effect of polymer substrate roughness on the resulting

barrier properties of (PET,PP,PE)/SiO<sub>x</sub> composites, and found that the thickness of the SiO<sub>x</sub> coating required to achieve a sufficient level of barrier performance increased on rougher substrates. In addition, the SiO<sub>x</sub> surface was described as being composed of nodular features. Garcia-Ayuso et al.<sup>55</sup> also demonstrated that coatings with surface roughnesses less than that of the polymer substrate typically possess low permeabilities.

Macroscopic pinhole-like defects were believed<sup>20,46,47</sup> to be directly responsible for the final barrier quality of SiO<sub>x</sub> coatings. A contrary viewpoint advocated<sup>34,39-41</sup> that the improvement in barrier efficacy achieved ( $\Pi < 1 \text{ cm}^3/\text{m}^2\text{-atm-day}$ ) constituted an indication of microscopic defects in the SiO<sub>x</sub> structure, rather than large-scale defects. Morphology-barrier studies conducted by Garcia-Ayuso et al.<sup>55</sup> provided no evidence for the existence of pinholes, and they characterized the surface of good (high-barrier) coatings as granular. Tropsha and Harvey<sup>34</sup> more recently reported that the SiO<sub>x</sub> surface consisted of irregular grain-like features and, on the basis of their AFM findings, suggested a film growth mechanism in which SiO<sub>x</sub> particles or grains grow as columns or cones around single nucleation sites. In support of these data, Henry et al.<sup>49</sup> used roughness measurements to show that SiO<sub>x</sub> surface features become more pronounced as the coating thickens, which is associated with the late-stage growth mechanism identified by Benmalek.<sup>60</sup> In a recent study by Wang et al.,<sup>62</sup> the surface morphology was investigated with respect to deposition power. Highly resolved images revealed an obvious trend in surface morphology as the power was increased and the barrier quality was consequently improved. At low power levels, irregular domains containing small grains were distributed inhomogeneously. As the power was increased, however, the grains became tightly packed with well-demarcated boundaries, thereby minimizing the possibility of surface defects. In the same study, a reduction in surface roughness accompanied an increase in deposition power.

## 1.6 DEPOSITION TECHNIQUES

As mentioned earlier, the development of vacuum deposition techniques constituted a crucial factor in promoting the increased level of interest in  $\text{SiO}_x$  gas barrier coatings on polymers. The principal deposition processes developed for  $\text{SiO}_x$  coatings include Physical Vapor Deposition (PVD) techniques<sup>13,22,46</sup> such as sputtering and electron beam (EB) gun deposition (thermal and reactive evaporation), as well as various forms of Plasma-Enhanced Chemical Vapor Deposition (PECVD).<sup>11,62-65</sup> The two most widely used processes are EB evaporation and PECVD. A conventional EB gun web-coater consists of a vacuum chamber (divided into winding and coating chambers), a pumping system, a web winding system, the EB-gun and control system, and a crucible system. The role of each of these parts and the operation of EB deposition is explained in detail by Krug et al.<sup>22</sup> and Schiller et al.<sup>66</sup> and will not be discussed further here. The deposition process of interest in the present study, PECVD, will be examined in more detail in the next section, which is followed by a comparison review of various deposition processes for  $\text{SiO}_x$ .

### 1.6.1 Plasma-Enhanced Chemical Vapor Deposition

Thin-film deposition processes in which molecular gases or vapors are used as source materials to react and form a solid film are commonly referred to as *chemical vapor deposition* (CVD) processes.<sup>67</sup> Classification of these processes reflects the method of activation: thermal energy (CVD), photon energy (photo or laser CVD) or electron energy (plasma-enhanced CVD, or PECVD).<sup>68</sup> We now focus our attention exclusively on the PECVD process. A simplified schematic of PECVD and a typical process chamber are displayed in Figs. 1.3a and 1.3b, respectively. As is evident in Fig. 1.3a, PECVD can be generally viewed<sup>68,69</sup> as consisting of three sequential processes: (i) chemical activation of gas molecules upon electron impact, (ii) dissociation into free radicals (e.g., removal of hydrogen from silane), and (iii) transport of these radical species to the substrate where

surface chemical reactions form the film. Electrons in the plasma, the source of energy for PECVD, are normally generated by Direct Current (DC), Radio Frequency (RF) or microwave discharges.<sup>70</sup> These plasma-generation techniques differ primarily in the energy distribution of the plasma-generated electrons, which, in turn, affect the nature of the activated plasma species responsible for forming the deposited film. Once the active species are formed, they are transported to the substrate surface by diffusion, the rate of which is referred to as the deposition rate. By judicious choice of the process parameters (such as power, pressure, precursor gas flow rates and deposition time), one can control the deposition rate and improve the quality of the film deposited. The singular and coupled effects of these parameters on the control of plasma conditions are addressed by Yasuda.<sup>71</sup>

One of the most desirable attributes of PECVD is that deposition can be conducted on various substrates at relatively low temperatures (i.e., room temperature to 500°C).<sup>72</sup> When compared to thermal CVD, which could increase the substrate temperature to 900°C,<sup>72,73</sup> PECVD affords a lower activation barrier for surface reactions. Of particular interest in the development of polymer/SiO<sub>x</sub> laminates, low temperature deposition reduces the extent of substrate damage (including flow) and minimizes the stress induced in the coating arising from thermal mismatch between the coating and substrate (detrimental in CVD).<sup>68</sup> In addition, PECVD is a multi-source process that is not dependent on line-of-sight considerations (in contrast to sputtering and evaporation).<sup>68</sup> This characteristic facilitates deposition of multilayered structures and good coverage of planar surfaces, as well as more complex geometries (e.g., cylindrical tubes with spherical caps or bottles).<sup>10,68</sup> Compositional uniformity of the resultant coating can also be maintained<sup>10,64,68</sup> in PECVD through control of the flow of gases and optimization of reactor geometry. Lastly, large substrate areas can be coated during a single run by roll-to-roll or batch-type PECVD coaters.<sup>11</sup> In fairness, it should be pointed out that PECVD also has several shortcomings, such as powder formation, cross contamination (causing poorly defined interfaces), severe and long-lasting start-up transients, and scale-up

difficulties.<sup>68,74,75</sup>

With these drawbacks notwithstanding, the advantages listed above have made PECVD a widely used thin-film deposition process in a variety of commercial applications.<sup>68</sup> Beginning with the first commercial PECVD reactors developed in the late 1970's to deposit silicon nitride passivation layers in the microelectronics industry,<sup>76</sup> PECVD applications have expanded considerably, as shown in Fig. 1.4. Use of PECVD to deposit transparent  $\text{SiO}_x$  gas-barrier coatings constitutes the main interest in this study, and it will be compared to other deposition techniques employed for this purpose in the next section.

### 1.6.2 Comparison of $\text{SiO}_x$ Deposition Techniques

The deposition techniques discussed earlier were introduced into the literature from the perspective of process or component improvement, with usually relatively little discourse provided in terms of the accompanying effect on  $\text{SiO}_x$  barrier performance. Mirroring the evolution of such process development, this section provides a chronological comparison of  $\text{SiO}_x$  deposition efforts.

The earliest and most established method by which to deposit  $\text{SiO}_x$  gas barrier coatings was sputtering. Chahroudi<sup>14</sup> in the late 1980's reported that EB sources provided 10–100% faster deposition than sputtering and were therefore more cost effective. Furthermore, Schiller<sup>77</sup> demonstrated that, although sputtering could be generally enhanced by diode, rather than magnetron, sputtering, this deposition process was unable to deposit films at deposition rates higher than 10 nm/sec. In marked contrast, evaporation by EB sources yielded densely packed  $\text{SiO}_x$  coatings (by increasing the substrate temperature and plasma excitation, and lowering the residual gas pressure) at deposition rates of up to 100 nm/sec.<sup>77</sup> The drawback to EB evaporation lies in the fact that the source material must be heated to very high temperatures (1100–1250°C for SiO and 1350–1500°C for  $\text{SiO}_2$ <sup>77</sup>). A reduction in thermal damage to the substrate was ultimately realized through the use of the low-temperature PECVD process.

Felts<sup>10</sup> has compiled an extensive comparison of these three deposition techniques with respect to SiO<sub>x</sub> barrier coatings. Upon comparing the two PVD techniques, sputtering resulted in coatings exhibiting better  $\Pi_{O_2}$  values relative to evaporation (0.13 vs. 3.78 cm<sup>3</sup>/100 in<sup>2</sup>-day-atm), in contrast to the results reported by Schiller.<sup>77</sup> The conclusions reached by Felts,<sup>10</sup> which were later confirmed,<sup>78</sup> can be attributed to the denser and more durable coatings obtained as a result of mixing (re-sputtering) at the substrate surface. Coatings produced by PECVD were, however, clearly superior to both PVD techniques ( $\Pi_{O_2}$ =0.04 cm<sup>3</sup>/100 in<sup>2</sup>-day-atm) due, in part, to improved adhesion of the coating to the substrate. An added benefit of PECVD, resulting from higher plasma exposure as compared to evaporation and sputtering, was more extensive cross-linking (from spectroscopic analysis<sup>10</sup>) of dissociated organosilicon molecules to form the SiO<sub>x</sub> coating structure.<sup>10</sup> As pointed out by Felt,<sup>11</sup> another advantage of PECVD is its ability to coat 3-D devices (e.g., tubes or bottles). In another extensive comparison of SiO<sub>x</sub> deposition processes, Chahroudi<sup>12</sup> has identified the advantages of PECVD over EB evaporation in terms of the following considerations. A broader range of starting materials and reaction conditions are available for PECVD, in which case the coating chemistry required for a specific application can be tailored with added flexibility. Moreover, PECVD produces uniform coatings on dust particles (the size of which can be minimized by lowering pressure and optimizing power and flow rates) incorporated in a thin SiO<sub>x</sub> coating, whereas EB evaporation (in its line-of-site operation) forms undesirable pinholes around dust particles. Finally, as mentioned before, PECVD can be conducted at reduced (substrate-safe) temperatures and does not require a cooling device such as a chill drum.<sup>12</sup>

## 1.7 CHEMICAL CHARACTERISTICS OF SiO<sub>x</sub> COATINGS

The chemistry of SiO<sub>x</sub> coatings also constitutes a non-trivial process consideration affecting their barrier performance. Control of oxygen content is particularly important, since the Si:O stoichiometry governs both the gas barrier properties and transparency of the

SiO<sub>x</sub> coating.<sup>15,20,77, 79</sup> In addition, the nature of the chemical bonds present and the incorporation of impurities (e.g., carbon or hydrogen) in the coating are extremely sensitive to deposition conditions and can dramatically degrade barrier performance.<sup>10,80,81</sup> In this section, studies employing various analytical techniques, such as Fourier-transform infrared (FTIR) spectroscopy, X-Ray photoelectron spectroscopy (XPS), electron probe microanalysis (EPMA), and elastic recoil detection are presented.

Coatings exhibiting superlative barrier efficacy and transparency are reportedly obtained<sup>10,15,20,77,79</sup> from sub-stoichiometric SiO<sub>x</sub> coatings in which x is greater than 1.5 and less than 1.8. Krug<sup>20</sup> has explained the effect of Si:O stoichiometry on barrier performance in terms of both the dependence of O<sub>2</sub> transmission rate on x (reproduced in Fig. 1.5a) and the glassy network of SiO<sub>2</sub> (Fig. 1.5b). The trend evident in Fig. 1.5a is attributed to the densification of the glassy network by (i) the removal of oxygen atoms and (ii) the closing of pores (see Fig. 1.5b). A concurrent transparency comparison between uncoated and coated PET has been performed<sup>20</sup> and is presented in Fig. 1.6. Here, the loss of clarity is due to absorption of UV light at unsaturated chemical bonds within the SiO<sub>x</sub> coating.<sup>20</sup> Thus, the value of x should be above 1.5 to avoid a yellowish tinge to the coating. Schiller et al.<sup>77,79</sup> and Chahroudi<sup>15</sup> have both confirmed this analysis, and Schiller et al.<sup>77</sup> have also proposed that x depends on the kind of particles impinging on the substrate surface, their impact ratio, sticking probability and chemical reactivity. While Suzuki et al.<sup>82</sup> has ascertained the compositions of SiO<sub>x</sub> coatings with EPMA, Pai et al.<sup>83</sup> have demonstrated that the Si–O–Si stretch peak position (at 1070 cm<sup>-1</sup> in FTIR spectroscopy) is directly proportional to the Si:O ratio. Felts<sup>10</sup> has used this method to calculate a value of x and, on the basis of this work, has proposed that a reduction in O<sub>2</sub> content increases the degree of Si–Si bonding while decreasing Si–O bonding. As a consequence of the number of valence sites — 4 for Si and 2 for O — an increased density of Si–Si bonds renders more efficient crosslinking, thus better barrier properties.

Felts<sup>10</sup> also reports greater SiO<sub>x</sub> film densification (which also improves barrier

performance) is obtained when the Si–O–Si vibrational peak broadens. Cross-linking of Si–O–Si chains is correlated with peak broadening,<sup>84</sup> and broadening is attributed to an increase in Si–O bonding.<sup>10,85</sup> The dense structure of a thin SiO<sub>x</sub> coating and the corresponding barrier properties both deteriorate upon incorporation of impurities such as C and H,<sup>80,81</sup> which reflect the relative concentrations of organosilicon and O<sub>2</sub> supplied during deposition. Theil<sup>81</sup> has found that the content of C within SiO<sub>x</sub> coatings can acceptably range from 1 to 36 atomic%. Higher C concentrations have a detrimental impact on the film structure, causing the coating to soften and become more polymeric. The presence of C and H impurities, detected by FTIR,<sup>80</sup> may likewise promote internal stresses that eventually lead to cracking. Likewise, Fusi et al.<sup>86</sup> have shown a considerable amount of C present by XPS and Secondary Neutral Mass Spectroscopy (SNMS) which, in contrast have attributed to C atoms released from the polymer substrate instead of from deposition and therefore they have concluded that it did not affect barrier properties.

## 1.8 MECHANICAL CHARACTERISTICS OF SiO<sub>x</sub> COATINGS

The durability and integrity of SiO<sub>x</sub> coatings deposited on polymer substrates must also be considered in the design of polymer/SiO<sub>x</sub> barrier materials to ensure quality control and long-term reliability. However, brittleness, which is a shared property of ceramic materials, hinders the handling of these coatings, since they can readily lose their barrier properties. In light of this potential shortcoming, studies have been conducted to measure the mechanical properties of these coatings. Their toughness, tensile stress response, adhesion and abrasion resistance are described in this section.

Initial efforts by Chahroudi<sup>8</sup> have shown that, even in a densely packed unstressed SiO<sub>1.8</sub> film of sufficient thickness, the maximum elastic elongation achieved was only 3%. The elasticity of the film was found to increase by increasing its packing density or by alloying it with small percentages of magnesium or aluminum oxide (as commercialized by Flex Products). Felts<sup>44</sup> also investigated the durability of SiO<sub>x</sub> coatings by straining

PET/SiO<sub>x</sub> laminates across an oxygen permeation cell and testing the laminate at incremental strain levels, and demonstrated that PVD coatings failed (cracked) at low strain levels (2-3%). The PECVD analogs, on the other hand, withstood 5-12% tensile strain before suffering the same catastrophic fate. An interesting result from the study of Felts<sup>44</sup>,<sup>87</sup> was that the rate at which  $\Pi_{O_2}$  degrades after a critical strain provides an indication of the level of adhesion between the coating and substrate. On the basis of this observation, a model was formulated in which elongation was increased through either an increase in substrate-coating adhesion or a reduction in coating thickness. Cracking patterns formed in PET/SiO<sub>x</sub> laminates upon tensile deformation were observed by SEM analysis and provided a measure of substrate-coating adhesion: the presence of regular, fine cracks indicated good adhesion, while coarse cracks not parallel to the tensile axis were representative of poor adhesion. Heil<sup>80</sup> performed similar experiments, as well as strained laminate films *in situ* during SEM. A 23% increase in  $\Pi_{O_2}$  beyond 8% critical strain for the PET substrate was achieved, but the PET/SiO<sub>x</sub> composite failed at only 2-4% strain. Cracking patterns, which developed transverse to the direction of the load, were also observed by SEM, supporting the conclusions of Felts<sup>44</sup> in that the critical strain to induce film cracking increases as coating thickness decreases. Peel tests also revealed<sup>80</sup> that PET-SiO<sub>x</sub> adhesion was fairly strong, in which case cracking or cohesive failure was not observed until tensile strains of 6%. Langowski<sup>88</sup> has also documented partial barrier loss for SiO<sub>x</sub> films at 4-8% for final PET/SiO<sub>x</sub> laminate products.

A recent study by Pitton et al.<sup>89</sup> has addressed the adhesion of PET/SiO<sub>x</sub> films, as measured by two different techniques (a scratch test and a fragmentation test), to identify the mode of failure: interfacial, cohesive or both. Tests performed on both stoichiometric and sub-stoichiometric silicon oxide films showed that SiO<sub>x</sub> films undergo little delamination, whereas SiO<sub>2</sub> films flake off their substrate after the tests. These results signified that the mode of failure was interfacial, in which case adhesion was improved by N<sub>2</sub> plasma treatment of the substrate prior to deposition. Additional studies have examined

the integrity of SiO<sub>x</sub> thin films by Acoustic Emission (AE) characterization and laser microscopy. Yanaka et al.<sup>90</sup> discovered that two types of AE signals were generated due to film fracture and delamination, whereas Futatsugi et al.<sup>91</sup> identified SiO<sub>x</sub> cracking as Mode-I and provided evidence of delamination under tensile stretching. These studies also employed laser microscopy to show that long cracks measuring a few millimeters in length in SiO<sub>x</sub> coatings can be accompanied by segmental cracks 0.07-0.18 mm in length due to the presence of impurities. Yanaka et al.<sup>92</sup> recently proposed a modification to the shear lag model<sup>88</sup> for multiple cracking of thin films to account for the failure of SiO<sub>x</sub> coatings measuring between 75 and 660 nm thick on a PET substrate. They found that the difference between the residual strains of the film and substrate increased as the thickness of the coating decreased, indicating that a form of relaxation occurs in the thicker films. Also, in both initial and multiple crack formation, SiO<sub>x</sub> coatings measuring more than 200 nm thick failed at critical stresses of 200 to 300 MPa. In marked contrast, thinner coatings failed at higher stress levels, thereby substantiating that SiO<sub>x</sub> coating toughness eventually decreases with increasing thickness.

## 1.9 ORGANIZATION OF THESIS

This thesis is organized to first provide (in Chapter 2) the reader with an abbreviated overview of (i) the PECVD process employed here to produce SiO<sub>x</sub> coatings on polymer substrates, and (ii) the analytical techniques used to characterize the morphological characteristics and barrier properties of the resultant polymer/SiO<sub>x</sub> laminates. Results obtained from an extended series of optimized PET/SiO<sub>x</sub> laminates subjected to O<sub>2</sub> and water vapor transmission are presented and discussed in Chapter 3. Chapter 4 provides a detailed description of the effect of PECVD processing parameters on the barrier properties and morphological evolution of SiO<sub>x</sub> coatings deposited on polycarbonate (PC) and subjected to O<sub>2</sub> permeation. This is followed by a listing of the most important conclusions to be drawn from this study and suggested future work (Chapter 5).

## REFERENCES

1. Koros, W.J., ed., *Barrier Polymers and Barrier Structures*, American Chemical Society, Washington, D.C., 1990.
2. Ashley, R.J. in *Polymer Permeability* (Comyn, J. ed.), Elsevier Applied Science Publishers, New York, 1985, pp. 269-308.
3. Goosey, M.T. in *Polymer Permeability* (Comyn, J. ed.), Elsevier Applied Science Publishers, New York, 1985, pp. 309-339.
4. Kumins, C.A. and Kwei, T.K. in *Diffusion in Polymers* (Crank, J., Park, G.S. eds.), Academic Press, New York, 1968, pp. 107-140.
5. Paulos, J.P. and Thomas, E.L. *Journal of Applied Polymer Science* **1980**, 25, 15.
6. Decandia, F., Vittoria, V., Rizzo, G. and Titomanlio, G. *Journal of Macromolecular Science and Physics* **1986**, B25, 365.
7. Bowler, J.F. *5th International Conference on Vacuum Web Coating 1991*, Bakish Materials Corp., Englewood, NJ, 72.
8. Chahroudi, D. *5th International Conference on Vacuum Web Coating 1991*, Bakish Materials Corp., Englewood, NJ, 79.
9. Jamieson, E.H.H. and Windle, A.H. *Journal of Materials Science* **1983**, 18, 64.
10. Felts, J. T. *Proceedings of the Society of Vacuum Coaters 33rd Annual Technical Conference 1993*, Society of Vacuum Coaters, Albuquerque, NM, 184.
11. Felts, J.T. and Grubb, A. D. *Journal of Vacuum Science and Technology A* **1992** 10, 1675.
12. Chahroudi, D. *Proceedings of the Society of Vacuum Coaters 33rd Annual Technical Conference 1990*, Society of Vacuum Coaters, Albuquerque, NM, 212.
13. Chahroudi, D. *Proceedings of the Society of Vacuum Coaters 34th Annual Technical Conference 1991*, Society of Vacuum Coaters, Albuquerque, NM, 130.
14. Chahroudi, D. *Proceedings of the Society of Vacuum Coaters 31st Annual Technical Conference 1988*, Society of Vacuum Coaters, Albuquerque, NM, 145.

15. Chahroudi, D. *Proceedings of the Society of Vacuum Coaters 32nd Annual Technical Conference 1989*, Society of Vacuum Coaters, Albuquerque, NM, 29.
16. Zachariasen, W.H. *Journal of American Chemical Society* **1932**, *54*, 3841.
17. Mozzi, R.L. and Warren, B.E. *Journal of Applied Crystallography* **1969**, *2*, 164.
18. Shackleford, J.F. and Masanyk, J.S. *Journal of Non-Crystalline Solids* **1978**, *30*, 27.
19. Shackleford, J.F. and Masanyk, J.S. *Journal of Non-Crystalline Solids* **1976**, *21*, 55.
20. Krug, T.G. *Proceedings of the Society of Vacuum Coaters 33rd Annual Technical Conference 1990*, Society of Vacuum Coaters, Albuquerque, NM, 163.
21. Broomfield, A.A. *Proceedings of the Society of Vacuum Coaters 35th Annual Technical Conference 1992*, Society of Vacuum Coaters, Albuquerque, NM, 21.
22. Krug, T., Ludwig, R. and Steiniger, G. *Proceedings of the Society of Vacuum Coaters 36th Annual Technical Conference 1993*, Society of Vacuum Coaters, Albuquerque, NM, 302.
23. Kinstle, J.F. *Proceedings of the Society of Vacuum Coaters 37th Annual Technical Conference 1994*, Society of Vacuum Coaters, Albuquerque, NM, 134.
24. Ghosal, K. and Freeman, B.D. *Polymers for Advanced Technologies* **1994**, *5*, 673.
25. Shepard, T.A., DelSorbo, C.R., Louth, R.M., Walborn, J.L., Norman, D.A., Harvey, N.G. and Spontak, R.J., *Journal of Polymer Science B : Polymer Physics* **1997**, *35*, 2617.
26. Doremus, R.H. *Glass Science*, John Wiley & Sons, Inc., London, 1973, pp. 213-228.
27. Bansal, N.P. and Doremus, R.H. *Handbook of Glass Properties*, Academic Press, New York, 1986, pp. 25-28.
28. Perkins, W.G. and Beagal, P.R. *Journal of Chemical Physics* **1971**, *54*, 1683.
29. Skelekihini, A.B., Dixon, A.B. and Ma, Y.H. *AIChE Journal* **1995**, *41*, 58.

30. Norton, F.J. *Nature* **1961**, *191*, 701.
31. Billmeyer, F.W. *Textbook of Polymer Science*, John Wiley & Sons, 1984.
32. Stannett, V. in *Diffusion in Polymers* (Crank, J., Park, G.S. eds.), Academic Press, New York, 1968, pp. 41-73.
33. Brandrup, J. and Immergut, E.H., eds., *Polymer Handbook* 3rd ed., John Wiley & Sons, New York, 1989, pp. VI/437-VI/444.
34. Tropsha, Y.G. and Harvey, N.G. *Journal of Physical Chemistry B* **1997**, *101*, 2239.
35. Felts, J.T. *Proceedings of the Society of Vacuum Coaters 34th Annual Technical Conference 1991*, Society of Vacuum Coaters, Albuquerque, NM, 99.
36. Rossi, G. and Nulman, M. *Journal of Applied Physics* **1993**, *74*, 5471.
37. Friedman, A. *Mathematics in Industrial Problems*, Springer-Verlag, New York, 1975, pp. 125-134.
38. Henry, B.M., Roberts, A.P., Grovenor, C.R.M., Sutton, A.P., Briggs, G.A.D., Tsukahara, Y., Miyamoto, T. and Chatet, R.J., to be submitted to the *Journal of Physical Chemistry B*.
39. Roberts, A.P., Henry, B.M., Sutton, A.P., Grovenor, C.R.M. and Briggs, G.A.D. to be submitted to *Journal of Physical Chemistry B*.
40. Erlat, A.G., Spontak, R.J., Clarke, R., Robinson, T., Haaland, P.D., Tropsha, Y., Harvey, N.G. and Vogler, E.A. *Journal of Chemical Physics* (submitted).
41. Erlat, A.G., Wang, B., Spontak, R.J., Tropsha, Y., Mar, K., Montgomery, D. and Vogler, E.A. *Journal of Materials Research* (submitted).
42. Norton, F.J. *Journal of American Ceramic Society* **1953**, *36*, 90.
43. Misiano, C., Simonetti, E., Menichella, S., Staffetti, F. and Taglioni, G. *Proceedings of the Society of Vacuum Coaters 36th Annual Technical Conference 1993*, Society of Vacuum Coaters, Albuquerque, NM, 269.
44. Felts, J.T. *Proceedings of the Society of Vacuum Coaters 36th Annual Technical*

- Conference 1993*, Society of Vacuum Coaters, Albuquerque, NM, 324.
45. Hagenbaugh, J. *5th International Conference on Vacuum Web Coating 1991*, Bakish Materials Corp., Englewood, NJ, 114.
  46. Mercea, P.V. and Bartan, M. *Journal of Membrane Science 1991*, 59, 353.
  47. Mercea, P.V. and Bartan, M. *Materials Chemistry and Physics 1991*, 30, 33.
  48. Henry, B.M., Roberts, A.P., Grovener, C.R.M., Sutton, A.P, Briggs, G.A.D., Tsukahara, Y., Miyamoto, T., Yanaka, M. and Chater, R.J. *Proceedings of the Society of Vacuum Coaters 41st Annual Technical Conference 1997*, Society of Vacuum Coaters, Albuquerque, NM, 434.
  49. Phillips, R.W., Markantes, T. and LeGallee, C. *Proceedings of the Society of Vacuum Coaters 36th Annual Technical Conference 1993*, Society of Vacuum Coaters, Albuquerque, NM, 293.
  50. Binnig, G., Rohrer, H., Gerber, C. and Weibel, E. *Physical Review Letters 1983*, 50, 120.
  51. Binnig, G., Quate, C.F. and Gerber, C. *Physical Review Letters 1986*, 56, 930.
  52. Heinzelmann, H., Meyer, E., Grütter, P., Hidber, H.R., Rosenthaler, L. and Güntherodt, H.J. *Journal of Vacuum Science and Technology A 1988*, 6, 275.
  53. Rugar, D. and Hansma, P. *Physics Today 1990*, October, 23.
  54. Bhushan, J., Israelachvili, J.N. and Landman, U. *Nature 1995*, 374, 607.
  55. Garcia-Ayuso, G., Vazquez, L. and Martinez-Duart, J.M. *Surface and Coatings Technology 1996*, 80, 203.
  56. Schmitz, I., Schreiner, M., Friedbacher, G. and Grasserbauer, M. *Applied Surface Science 1997*, 115, 190.
  57. Martin, Y., Williams, C.C. and Wichramasinghe, G.H. *Journal of Applied Physics 1987*, 61, 4723.
  58. Magonov, S.N., Elings, V. and Whangbo, M.H. *Surface Science 1997*, 375, L385.
  59. Gavitt, I. F. *Proceedings of the Society of Vacuum Coaters 36th Annual Technical*

- Conference 1993*, Society of Vacuum Coaters, Albuquerque, NM, 254.
60. Benmalek, M. and Dunlop, H.M. *Surface & Coatings Technology* **1995**, 76-77, 821.
61. Zuniga- Segunda, A., Ruiz, F., Vazquez- Lopez, C., Gonzales- Hernandez, J., Torres- Delgado, G. and Tsu, D.V. *Journal of Vacuum Science and Technology A* **1994**, 12, 2572.
62. Wang, B., Erlat, A.G., Spontak, R.J., Tropsha, Y. G., Vogler, E.A., Dalvie, M. and Mar, K. *ACS Polymer Preprints* **1997**, 38, 1018.
63. Kleimberg-Sapieha, J.E., Martinu, L., Kuttel, O.M. and Wertheimer, M.R. *Proceedings of the Society of Vacuum Coaters 36th Annual Technical Conference 1993*, Society of Vacuum Coaters, Albuquerque, NM, 445.
64. Knoll, R. W. and Theil, J.A. *Proceedings of the Society of Vacuum Coaters 38th Annual Technical Conference 1995*, Society of Vacuum Coaters, Albuquerque, NM, 425.
65. Walther, M., Heming, M. and Spallek, M. *Surface and Coatings Technology* **1996**, 80, 200.
66. Schiller, S., Neumann, M., Morgner, H. and Schiller, N. *Proceedings of the Society of Vacuum Coaters 36th Annual Technical Conference 1993*, Society of Vacuum Coaters, Albuquerque, NM, 278.
67. Jansen, K.F. and Kern, W. in *Thin Film Processes II* (Vossen, J.L. and Kern, W. eds.), Academic Press, San Diego, 1991, Part III-1.
68. Jansen, F. *American Vacuum Society Short Course Program, 43rd National Symposium*, American Vacuum Society, Philadelphia, 1996.
69. Mort, J. and Jansen, F. *Plasma Deposited Thin Films*, CRC Press, Inc., Boca Raton, 1986.
70. Wertheimer, M.R. and Moisan, M. *Journal of Vacuum Science and Technology A* **1983**, 3, 2643.

71. Yasuda, H. *Plasma Polymerization*, Academic Press, Inc., New York, 1985, pp. 277-333.
72. Sherman, A. *Chemical Vapor Deposition for Microelectronics: Principles, Technology and Applications*, Noyes Publications, New York, 1987, pp. 120-131.
73. Reif, R. and Kern W. in *Thin Film Processes II* (Vossen, J. and Kern, W., eds.) pp. 526-558.
74. Jansen, F. and Kuhman, D. *Journal of Vacuum Science and Technology* **1988**, A6, 13.
75. Nguyen, S.V., Dobunzinsky, D., Dopp, D., Gleason, R., Gibson, M. and Fridmann, S. *Thin Solid Films* , **1990**, 193/194, 595.
76. Rosler, R.S. *Solid State Technology* June 1991, 67.
77. Schiller, S., Neumann, M. and Strumpf, J. *Proceedings of 3rd International Conference on Vacuum Web Coating* **1989**, Bakish Materials Corp., Englewood, NJ, 24.
78. Misiano, C., Simonetti, E., Cerolini, P. and Staffetti, F. *Proceedings of the Society of Vacuum Coaters 34th Annual Technical Conference* **1991**, Society of Vacuum Coaters, Albuquerque, NM, 105.
79. Schiller, S, Neumann, M. and Zeissig, G. *5th International Conference on Vacuum Web Coating* **1991**, Bakish Materials Corp., Englewood, NJ, 19.
80. Heil, R.B. *Proceedings of the Society of Vacuum Coaters 38th Annual Technical Conference* **1995**, Society of Vacuum Coaters, Albuquerque, NM, Society of Vacuum Coaters, Albuquerque, NM, 33.
81. Theil, J.A., Brace, J.G. and Knoll, R.W. *Journal of Vacuum Science and Technology* **1994**, A2, 1365.
82. Suzuki, T., Sato, M., Tsukagoshi, K., Takahashi, Y., Inagawa, K., Tsukahara, S., Yamamori, T. and Matsumori, A. *5th International Conference on Vacuum Web Coating* **1991**, Bakish Materials Corp., Englewood, NJ, 86.

83. Pai, P.G., Chao, S.S. and Takagi, Y. *Journal of Vacuum Science and Technology* **1986**, A4, 689.
84. Wrobel, A.M., Wertheimer, M.R., Dib, J. and Schreiber, H.P. *Journal of Macromolecular Science-Chemistry* **1980**, A14, 321.
85. Adams, A.C. *Solid State Technology* April 1983, 135.
86. Fusi, A., Misiano, C., Stafetti, F., Kammer, M., and Raarup, S. *Proceedings of the Society of Vacuum Coaters 39th Annual Technical Conference 1996*, Society of Vacuum Coaters, Albuquerque, NM, 366.
87. Wajeiechowski, P. and Mendolia, M. in *Physics of Thin Films*, Academic Press, Inc., 1992, 271.
88. Langowski, H.C. *Proceedings of the Society of Vacuum Coaters 39th Annual Technical Conference 1996*, Society of Vacuum Coaters, Albuquerque, NM, 398.
89. Pitton, Y., Hamm, D., Lang, F. R., Mathieu, H. J., Leterrier, Y. and Manson, J.-A. E. *Journal of Adhesion Science and Technology* **1996**, 10, 1047.
90. Yanaka, M., Nakaso, N., Tshukara, Y. and Niltsu, N. *Journal of Acoustic Emission* **1995**, 13, 23.
91. Futatsugi, T., Ogawa, S., Takemoto, M., Yanaka, M. and Tsukahara, Y. *Non-Destructive Testing & Evaluation International* **1996**, 29, 37.
92. Yanaka, M., Tsukahara, Y., Nakaso, N. and Takeda, N. *Journal of Materials Science* **1998**, 33, 2111.

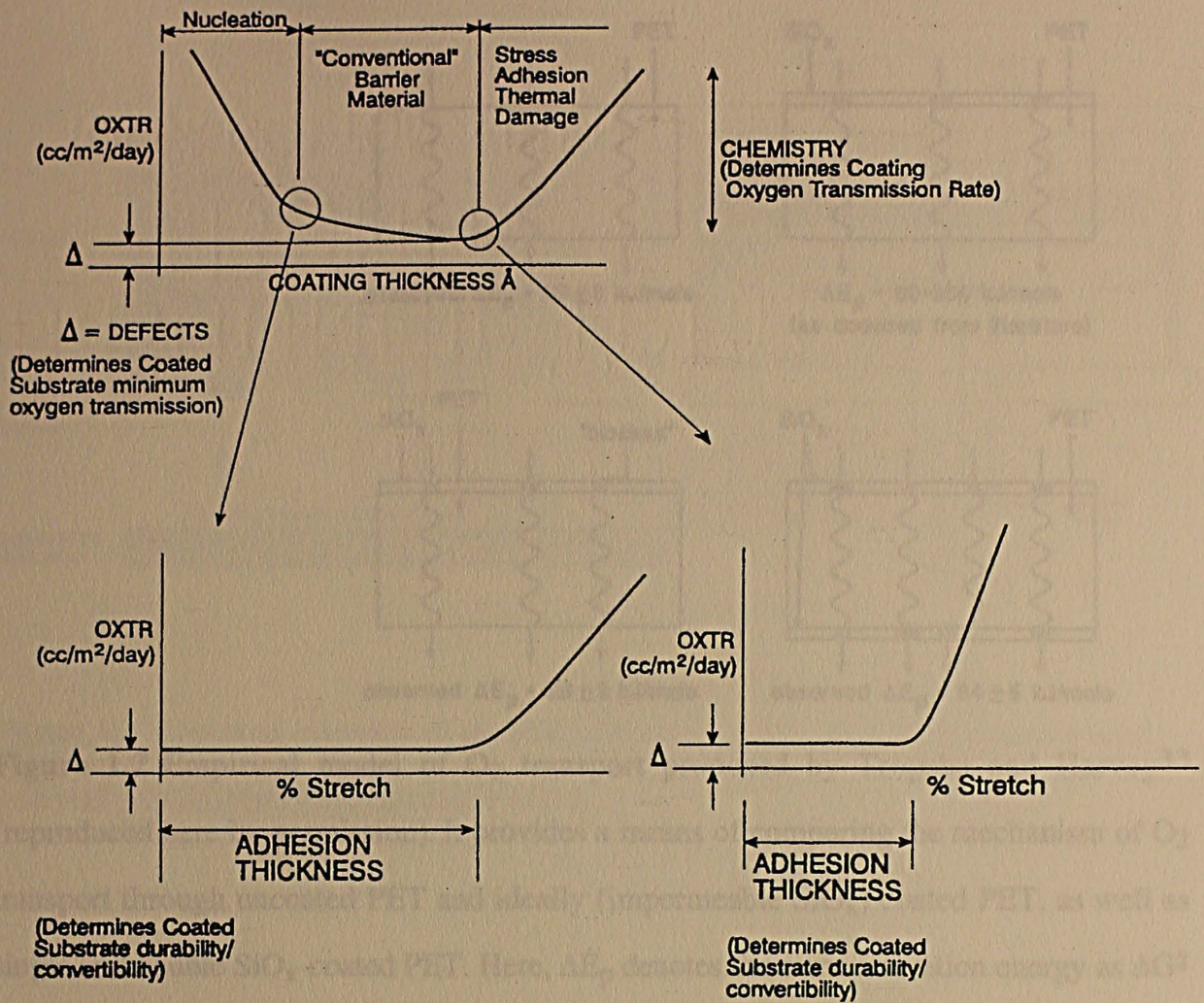


**Figure 1.1.** A defect model for  $\text{SiO}_x$  coatings proposed by Felts<sup>43</sup> (and reproduced here with permission), based on extensive measurements aiming to correlate the effect of thickness on the  $\text{O}_2$  transmission rate.

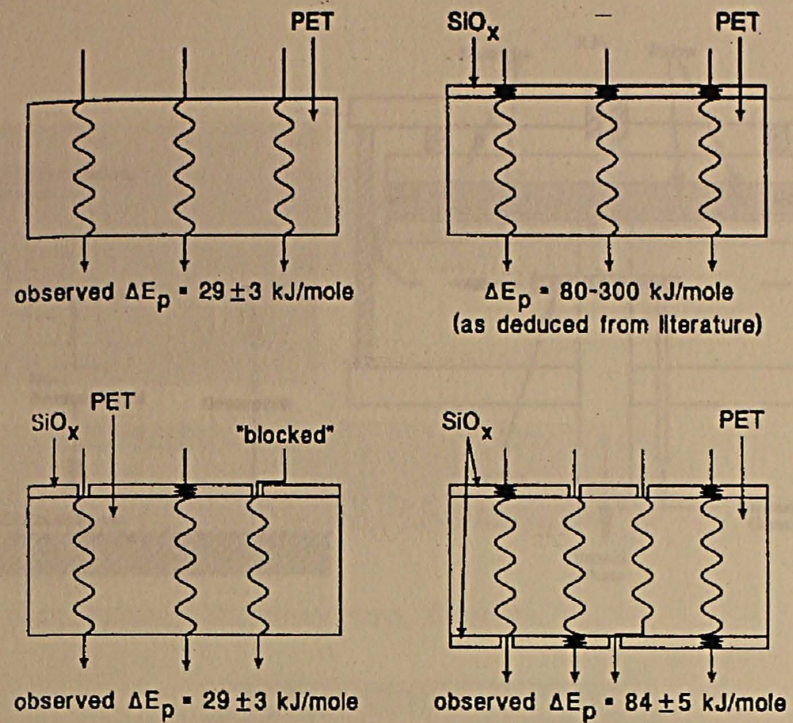


**Figure 1.2** Empirical model of  $O_2$  transport proposed by Tropsha and Harvey<sup>33</sup> (reproduced here by permission). It provides a means of comparing the mechanism of  $O_2$  transport through uncoated PET and ideally (impermeable  $SiO_x$ ) coated PET, as well as single and double  $SiO_x$ -coated PET. Here,  $\Delta E_p$  denotes the same activation energy as  $\Delta G^\ddagger$  used in the text.

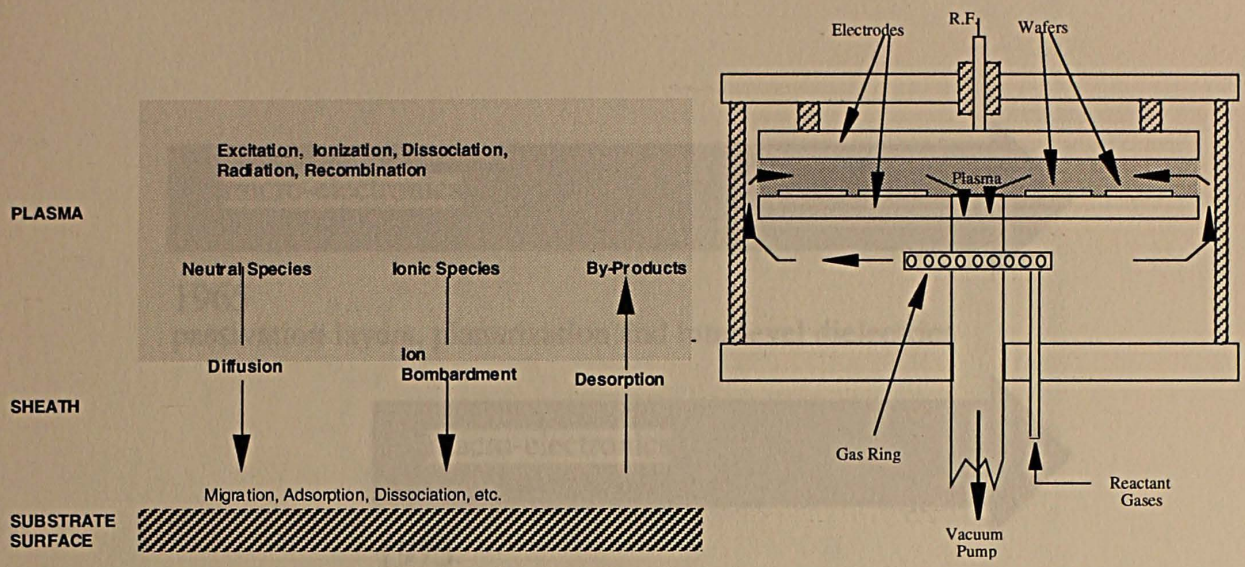


**Figure 1.3** A general overview of the PECVD process (left), as well as a widely used cold wall parallel-plate PECVD reactor (right).

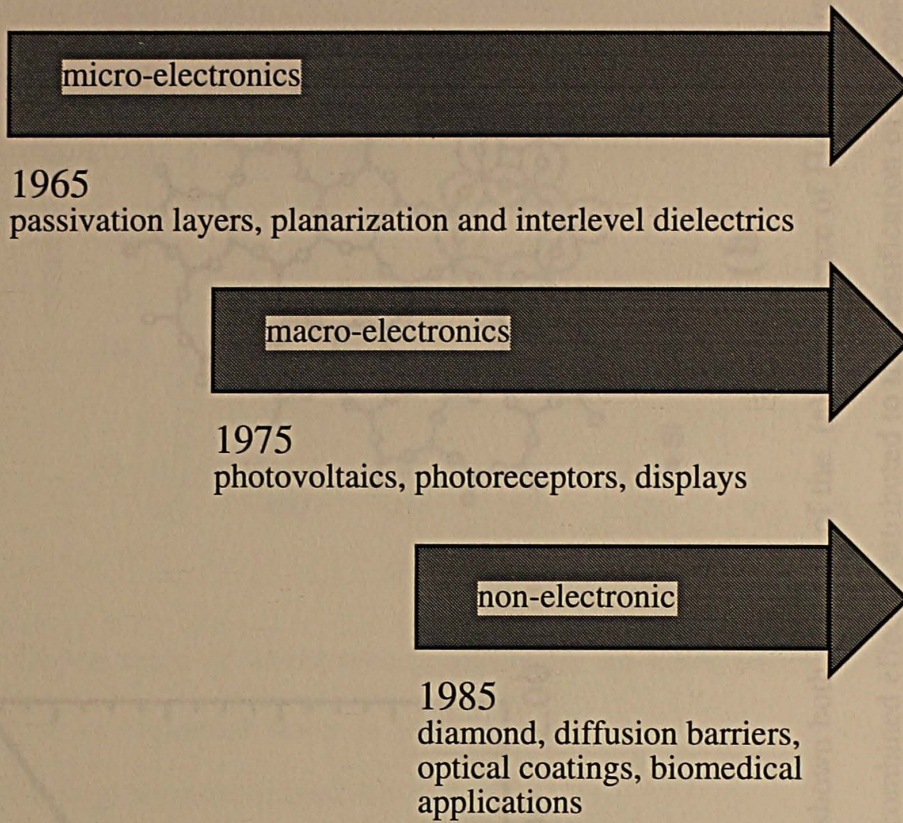
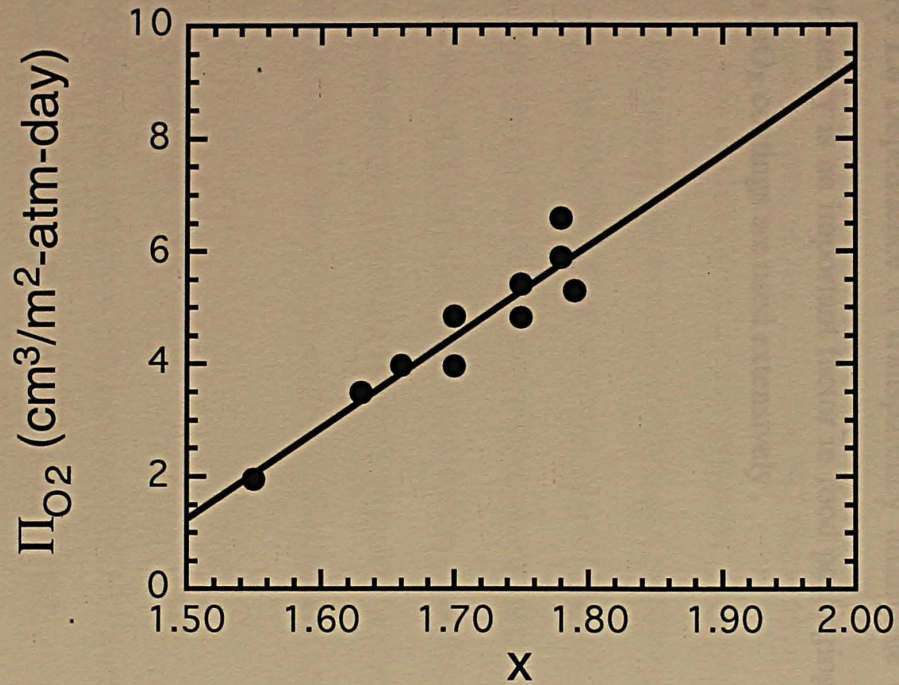
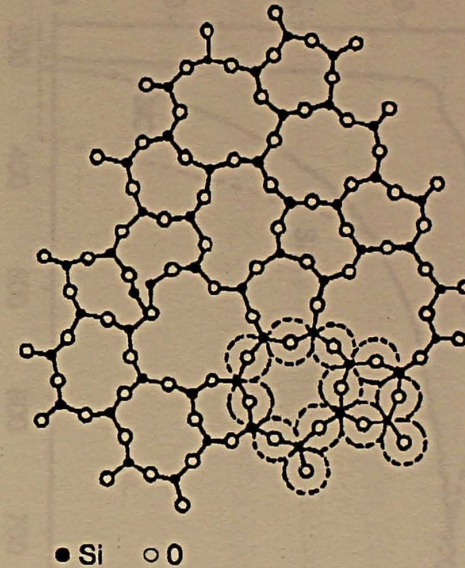


**Figure 1.4** Chronological development of PECVD as applied to commercial applications



(a)



(b)

**Figure 1.5** Effect of Si:O stoichiometry on barrier performance shown both in terms of the (a) dependence of  $\Pi_{O_2}$  on  $x$  (reproduced from the data of Krug<sup>20</sup>) and (b) the glassy network of  $SiO_2$ . A combined effect is attributed to the densification of the coating as the concentration of available  $O_2$  decreases.

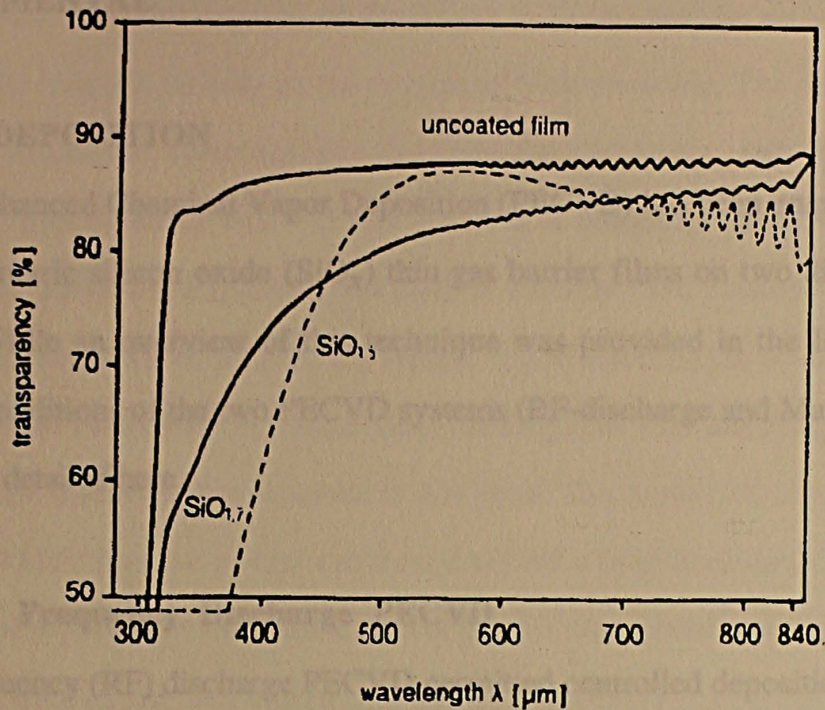


**Figure 1.6** Dependence of transparency attainable on  $\text{SiO}_x$  stoichiometry for PET. Transparency is an important factor in food packaging and medical device industries in which  $\text{SiO}_x$  coatings are used extensively .

### 1.1.2 Magnetically Enhanced PECVD

A magnetically enhanced (Magnatron) PECVD system was used to deposit  $\text{SiO}_x$  films on Mylar® — polyethylene terephthalate (PET) — substrates measuring about 23 μm thick. Two reactants, HMDSO and trimethylsilane (TMS), constituted the organosilicon starting materials. Displayed in Fig. 2.3 is a schematic illustration of the system, in which

## 2. EXPERIMENTAL

### 2.1 FILM DEPOSITION

Plasma Enhanced Chemical Vapor Deposition (PECVD) has been employed to deposit sub-stoichiometric silicon oxide ( $\text{SiO}_x$ ) thin gas barrier films on two different polymer substrates. While an overview of this technique was provided in the Introduction, the operational conditions of the two PECVD systems (RF-discharge and Magnetron) used in this study are detailed here.

#### 2.1.1 Radio Frequency Discharge PECVD

Radio frequency (RF) discharge PECVD permitted controlled deposition of  $\text{SiO}_x$  films on polycarbonate (PC) substrates. For this series, PC films measuring about 0.18 mm thick were coated with hexamethyldisiloxane (HMDSO). A schematic of this RF-PECVD system can be seen in Fig. 2.1. The PC films were placed on the electrodes, and the chamber was evacuated to a base pressure, preferably below 0.7 Pa. Following this, HMDSO monomer and an oxidizer ( $\text{O}_2$ ) were admitted into the chamber (see Fig. 2.1). For this study, the HMDSO flow rate was varied from 1.5 to 3.5  $\text{cm}^3(\text{STP})/\text{min}$  (abbreviated sccm), and the  $\text{O}_2$  flow rate ranged from about 50 to 110 sccm. The system was pumped continuously at a sufficient rate to maintain a predetermined system pressure. The RF power generator and matching network generated a plasma with a frequency of about 1 to 50 MHz at 0.1 to 2  $\text{W}/\text{cm}^2$ , depending on the number and proximity of the electrodes.

#### 2.1.2 Magnetron PECVD

A magnetically enhanced (Magnetron) PECVD system was used to deposit  $\text{SiO}_x$  films on Mylar® — poly(ethylene terephthalate) (PET) — substrates measuring about 25  $\mu\text{m}$  thick. Two monomers, HMDSO and trimethylsilane (TMS), constituted the organosilicon starting materials. Displayed in Fig. 2.2 is a schematic illustration of the system,<sup>1</sup> in which

a magnetic field was superimposed on the 10 cm × 10 cm titanium vertical electrodes by placing ten bar magnets radially on the reverse of each electrode. The resultant sandwich sample was suspended symmetrically between the electrodes, and the chamber was subsequently evacuated to below 133.3 Pa with a roughing pump, after which the turbomolecular pump was activated. Flow rates of monomer and oxidizer were adjusted, as was the system pressure, to preselected values. Upon stabilization of the flow rates and pressure, the electrodes were powered using the amplifier and matching network. Glow from the plasma discharge was observed at this point. The deposition time was constant at 3 min, after which time the power was turned off for a brief cool-down period. Plasma deposition was repeated 2× more for a total of three 3 min depositions/sample. At the end of deposition, the chamber was vented, and the sample was carefully removed for testing.

## 2.2 OXYGEN TRANSMISSION MEASUREMENTS

Oxygen transmission measurements for PC/SiO<sub>x</sub> and PET/SiO<sub>x</sub> laminates were conducted through the use of an Oxtran 2/20 O<sub>2</sub> permeability measuring instrument, manufactured by Modern Controls, Inc. (Minnesota, MN). This instrument was computer controlled, as is seen from a schematic diagram of the instrument in Fig. 2.3. Specimen films were first cut by hand so that the tested area was 50 cm<sup>2</sup>, or (in the case of the PC substrate) masked with Al foil for a reduced area of 5 cm<sup>2</sup>, and mounted into the test cell. The edges of the test cell were tightly sealed by an O-ring to prevent external air leakage into the cell. Films were conditioned for up to 4 hrs prior to testing by flushing the system with N<sub>2</sub> to remove residual O<sub>2</sub> from within the cell.

During measurements, O<sub>2</sub> was continuously fed into the test cell through the *outside* chamber and was removed through an exhaust port. A mixture of high-purity N<sub>2</sub> (98%) and H<sub>2</sub> (2%) served as the carrier gas and was concurrently admitted in continuous fashion into the cell through the *inside* chamber. Before entering the cell however, the carrier gas passed over a catalyst that promoted reaction between H<sub>2</sub> and O<sub>2</sub> to form water vapor.

Thus, the carrier gas was assured to be free of O<sub>2</sub>, which might inadvertently affect the O<sub>2</sub> transmission rate measurements. Throughout the test, O<sub>2</sub> permeating through the laminate under investigation was sent (via the carrier gas) to a Coulox O<sub>2</sub> sensor for counting and then removed through the exhaust port. The Coulox sensor was a coulometric fuel cell that produced an electrical current when impacted by molecular O<sub>2</sub>. The current generated was directly proportional to the amount of oxygen passing through the sensor, which was outputted as the O<sub>2</sub> transmission rate expressed in units of cm<sup>3</sup>/m<sup>2</sup>-atm-day. Unless otherwise stated, all O<sub>2</sub> transmission rate measurements reported in this study were conducted at 30°C and 0% relative humidity. For a limited number of specimens, additional measurements performed for Arrhenius-type activation energy analysis were acquired at 10, 20, 30, 35 and 40°C.

### 2.3 WATER VAPOR TRANSMISSION MEASUREMENTS

Thin SiO<sub>x</sub> coatings deposited on PET substrates were also examined for water vapor transmission rate by use of a Permatran-W600 instrument, illustrated in Fig. 2.4. The PET/SiO<sub>x</sub> laminates were cut to an area of 10 cm × 10 cm and mounted between the upper and lower halves of a removable diffusion cell. The lower part of the assembled cell contained a pad moistened with water or a saturated brine solution, whereas the upper part was vented through two openings to permit a constant flow of bone dry N<sub>2</sub> to pass across the exposed area (50 cm<sup>2</sup>) of the film. Once a specimen was inserted in the conditioning rack and clamped, it was subsequently exposed to continuous flow of dry N<sub>2</sub> across the upper side, whereas the bottom side was exposed to water vapor from the moist pad in the high humidity cavity. The cells were conditioned for about 24 hrs until a steady-state transmission rate was established.

Once steady-state conditions were attained, a test cycle commenced when the N<sub>2</sub> side of the test cell was vented to an infrared sensor and pump. Gas leaving the dry cavity through the exhaust port consisted of air and water vapor in a ratio determined by both the dry air-

purge rate and the rate of water vapor transmission through the PET/SiO<sub>x</sub> composite film. A constant dry air flow rate into the cell was required to ensure that the water vapor density in the exhaust line was determined solely by the water vapor transmission rate, which was measured by the infrared detector. The output from this detector was proportional to the transmission rate of moisture through the film, which was expressed in units of g/m<sup>2</sup>-day. Water vapor transmission rate measurements were obtained at 38°C to permit comparison of coatings deposited under variable deposition conditions, and between 24 and 42°C for activation energy analysis.

## 2.4 ATOMIC FORCE MICROSCOPY

Operation of an atomic force microscopy (AFM) instrument necessitated imaging SiO<sub>x</sub> surfaces by force (not current) through the use of a sharp tip (e.g., Si<sub>3</sub>N<sub>4</sub>), which was connected to an oscillating cantilever beam. This design permitted simultaneous acquisition of phase, height and 3-D oblique images, as well as profilometric surface roughness measurements at the nanoscale.<sup>2</sup> The instrument operated in two modes, contact and tapping. The first was not suitable for PET/SiO<sub>x</sub> composite films due to damage imparted to the SiO<sub>x</sub> surface by the tip. Therefore, tapping mode was used throughout this study. In this mode, the tip was rapidly vibrated near the surface, thereby minimizing the tip-sample interactions responsible for surface deformation while probing long-range forces (e.g., van der Waals and electrostatic) for images. The magnitude of these forces was measured by changes in the spring constant and thus the resonant frequency of the spring connected to the cantilever.

In this work, a Digital Instruments Nanoscope D-3000 AFM was employed in tapping mode. An operational schematic diagram of this instrument is presented in Fig. 2.5a. Super sharp Olympus tapping mode etched silicon tips (shown in Fig. 2.5b) were used to reduce tip-generated effects (which are convoluted with the measured forces<sup>3</sup>) and increase image quality at reasonably high spatial resolution. Specimens were prepared by first cutting a

small piece (about 3 mm × 3 mm) of each SiO<sub>x</sub>-coated polymer investigated and then attaching this piece to a glass slide through the use of double-sided tape. The mounted specimen was then placed onto the sample stage (see Fig. 2.5a) for examination at ambient temperature and pressure.

## 2.5 TRANSMISSION ELECTRON MICROSCOPY

Transmission electron microscopy (TEM) was performed on SiO<sub>x</sub> coatings deposited only on PET substrates. In this technique, electrons accelerated to predetermined voltage were focused onto the sample through the use of electromagnetic lenses, and transmitted (unscattered, elastically scattered and inelastically scattered) electrons were collected onto a phosphorus viewing screen with the aid of additional magnetic lenses. A tungsten filament was used to produce the electron beam. The operation of a conventional TEM can be found in any textbook<sup>4-7</sup> on the subject and, for this reason, is not reproduced here. In this study, a Zeiss EM902 transmission electron spectroscopic microscope (depicted in Fig. 2.6) was operated at an accelerating voltage of 80 kV and an energy loss of 0 eV. Such zero-loss imaging enhanced the low image contrast inherent in the amorphous samples due to selective removal of inelastically scattered electrons from the images (only unscattered and elastically scattered electrons were permitted to form the image).<sup>6</sup> Planar images of the SiO<sub>x</sub> coatings (typically measuring on the order of 0.1 μm thick) were collected upon dissolution of the PET substrate.

Following Jamieson and Windle<sup>8</sup> in their studies of PET/Al<sub>x</sub>O<sub>y</sub> composites, the technique by which this was achieved is displayed in Fig. 2.7. Very small pieces of a PET/SiO<sub>x</sub> laminate were first cut and placed on the top of 400 mesh Cu TEM grids (measuring *ca.* 3 mm in diameter), and the loaded grids were placed on a graphite screen supported by small metal pieces in a Petri dish. The bottom of the dish was subsequently filled with a small amount of *o*-chlorophenol (caution was exercised to avoid contacting the solvent to the screen), and the dish was covered prior to heating to 110°C. After about 1 hr

under these conditions, the PET was dissolved by the *o*-chlorophenol vapor, leaving behind the SiO<sub>x</sub> thin film on the copper grid. During this sample preparation, the lid was opened (in a fumehood) every 5-10 min to prevent condensation of *o*-chlorophenol on the glass lid and eventually on the SiO<sub>x</sub> coating. Specimens were carefully removed from the dish and cleaned with ethanol prior to drying and TEM examination.

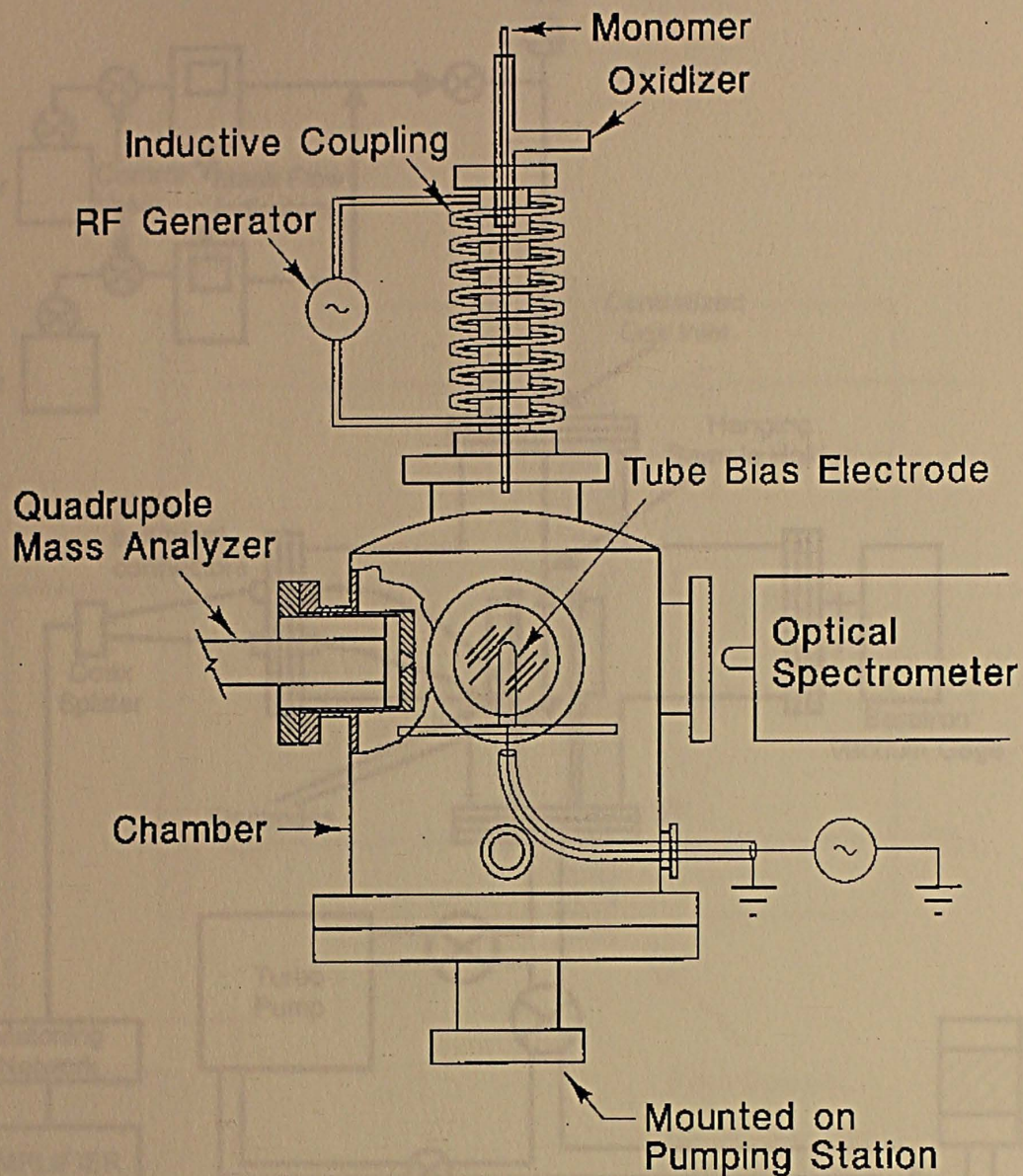
## 2.6 THICKNESS AND REFRACTIVE INDEX MEASUREMENTS

Ellipsometry, a well-established optical technique to determine the optical constants of bare surfaces and the refractive indices and thicknesses of thin films on those surfaces, was performed on SiO<sub>x</sub> coatings deposited onto the PC substrate. During analysis, a collimated beam of unpolarized, monochromatic light was transmitted through a polarizer (polarizing prism) and a compensator to the surface of the sample at an angle of incidence set by the user. The beam was reflected by the sample and passed through another polarizing prism, the analyzer, to a photomultiplier detector. The reflection from the sample altered the polarization state of the beam due to the optical properties of the sample. As a consequence, the refractive index and thickness of each tested sample were determined. Refractive index and thickness measurements were conducted using a Rudolf ellipsometer (see Fig. 2.8) on SiO<sub>x</sub> coatings deposited onto Si wafers. Measurements were obtained at a wavelength of 632.8 nm and an incidence angle of 70° from at least four different spots on each sample and averaged to obtain the final refractive index and thickness (variation in the data was less than 1%).

## REFERENCES

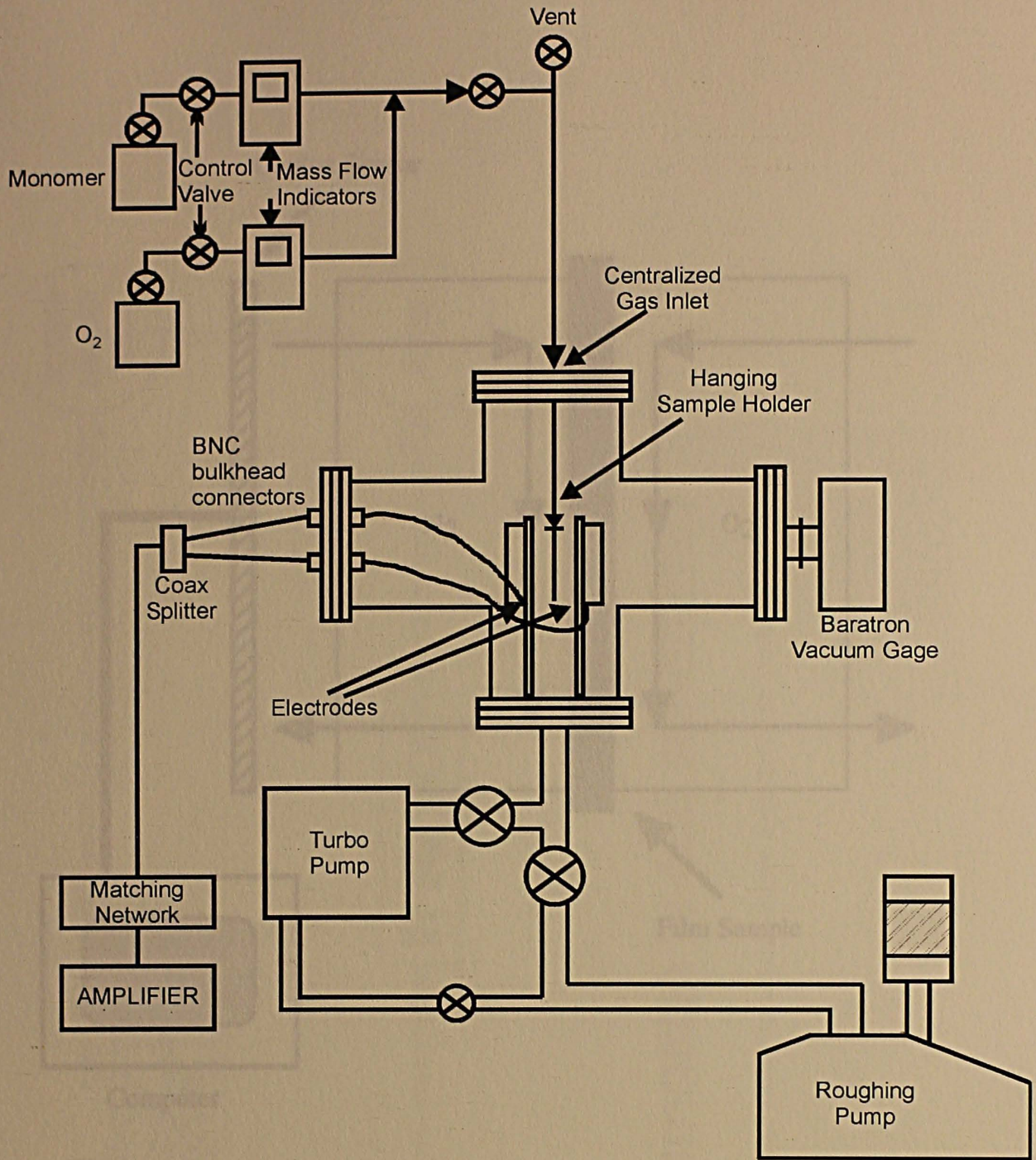
1. Yasuda, H. *Plasma Polymerization*, Academic Press, Inc., New York, 1985, pp. 277-333.
2. Heinzelmann, H., Meyer, E., Grütter, P., Hidber, H.R., Rosenthaler, L. and Güntherodt, H.J. *Journal of Vacuum Science and Technology A* **1988**, *6*, 275.
3. Schmitz, I., Schreiner, M., Friedbacher, G. and Grasserbauer, M. *Applied Surface Science* **1997**, *115*, 190.
4. Reimer, L. *Transmission Electron Microscopy; Physics of Image Formation and Microanalysis*, 3rd ed., Springer-Verlag, New York, 1993, pp. 86-134.
5. Agar, A.W., Alderson, R.H. and Chescoe, D. *Principles and Practice of Electron Microscope Operation*, North Holland Publishing Company, New York, 1985, pp. 166-190.
6. Reimer, L., ed., *Energy-Filtering Transmission Electron Microscopy*, Springer, New York, 1995, pp. 48-49.
7. Williams, D.B. and Carter, C.B. *Transmission Electron Microscopy, A Textbook For Materials Science*, Plenum Press, New York, 1996, pp. 131-153.
8. Jamieson, E.H.H. and Windle, A.H. *Journal of Materials Science* **1983**, *18*, 64.

Figure 2.1 Schematic illustration of the radio frequency (RF) discharge PECVD system employed as a part of this study to produce SiO<sub>2</sub> thin coatings on a polycarbonate (PC) substrate.

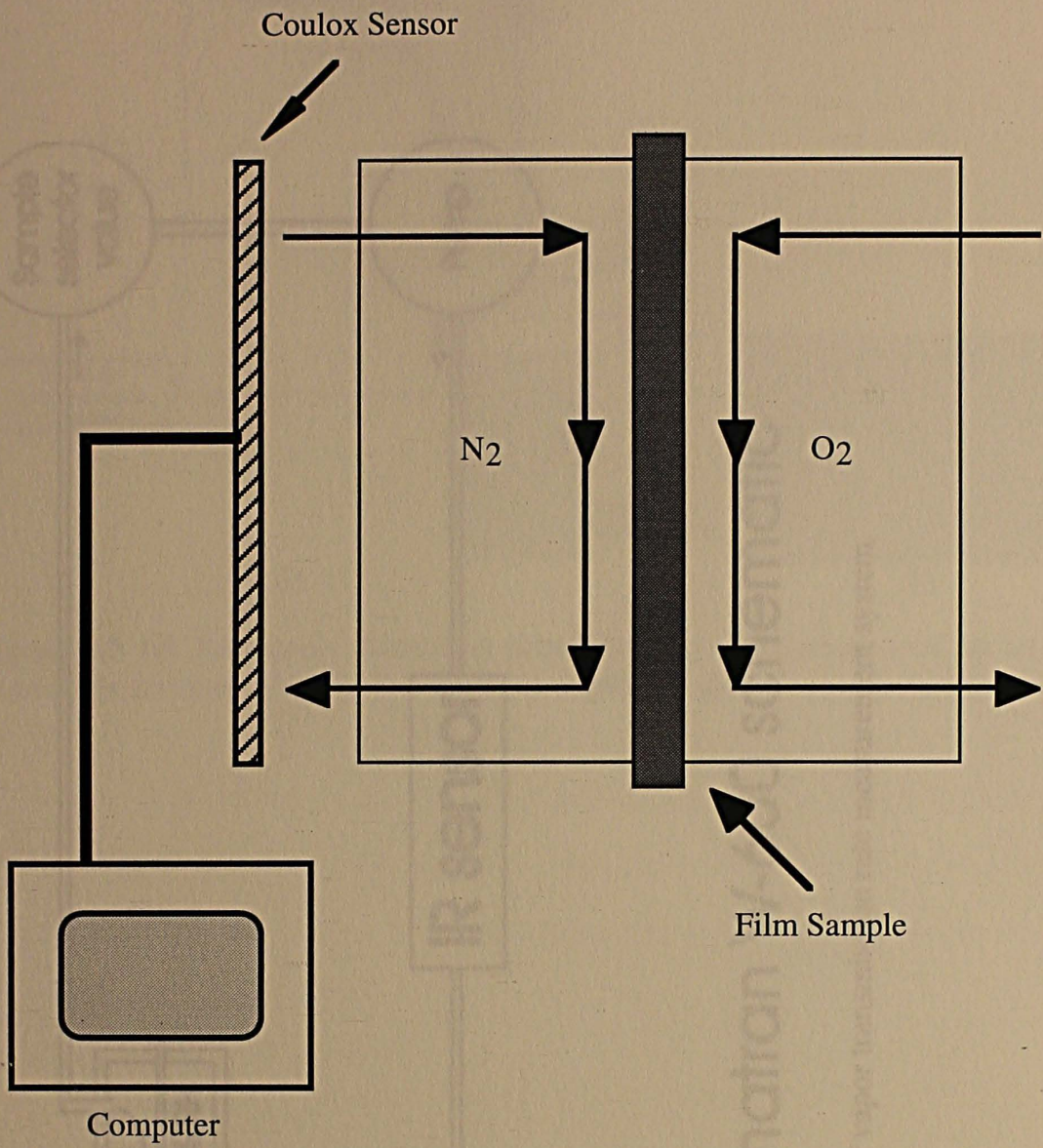


**Figure 2.1** Schematic illustration of the radio frequency (RF) discharge PECVD system employed as a part of this study to produce  $\text{SiO}_x$  thin coatings on a polycarbonate (PC) substrate.

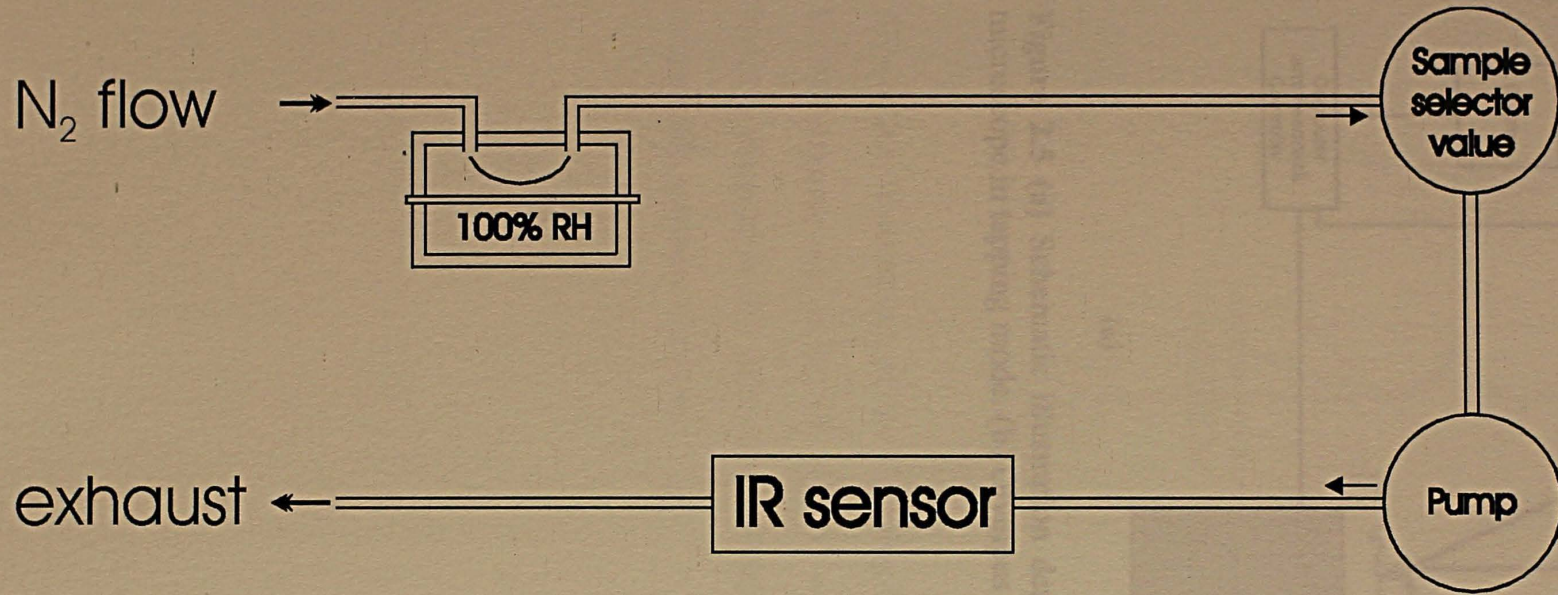
Figure 2.2 Schematic diagram of the Magnesium Plasma Deposition System used here to deposit  $\text{SiO}_2$  on PET substrates.



**Figure 2.2** Schematic diagram of the Magnetron Plasma Deposition System used here to deposit SiO<sub>x</sub> on PET substrates.

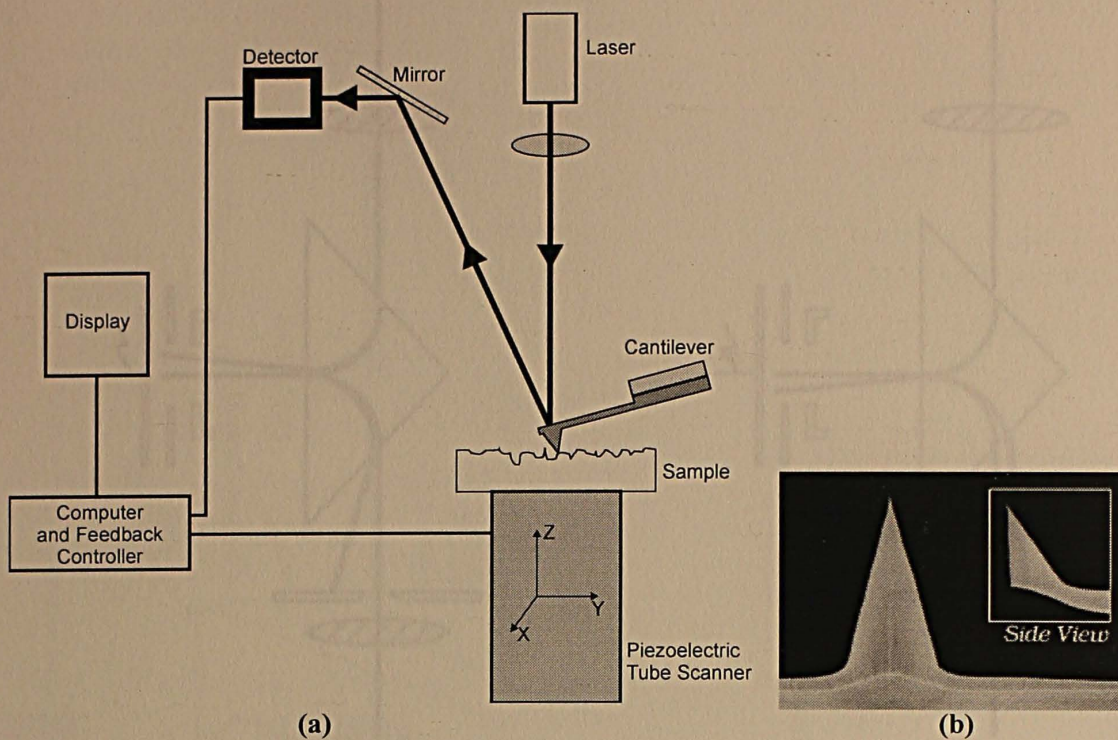


**Figure 2.3** Simplified schematic showing the operating principle of the Oxtran 2/20 oxygen transmission rate measurement system.



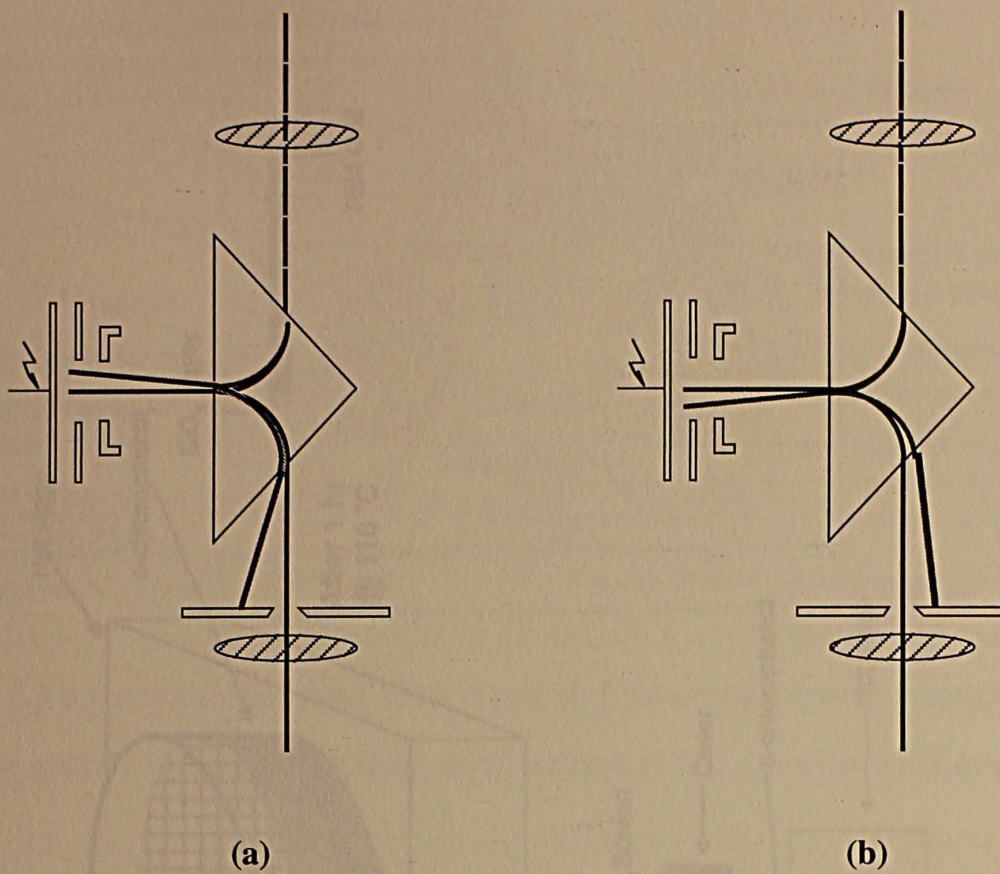
## Permatran W-600 schematic

Figure 2.4 Flow diagram of the water vapor transmission rate measurement system.



**Figure 2.5 (a)** Schematic illustration demonstrating the operation of an atomic force microscope in tapping mode. **(b)** Olympus tapping mode etched silicon probe.

Figure 2.6 illustrates the operation of the Constant-Height-Modulation energy filter in the Zeiss EM100 microscope. In (a)  $\Delta E = 0$  eV, which yields classic bright-field and dark-field images, whereas in (b)  $\Delta E > 0$  eV, which permits electron spectroscopic imaging with inelastically scattered electrons.



**Figure 2.6** Illustrations of the Castaing-Henry-Ottensmeyer energy filter in the Zeiss EM902 microscope. In (a)  $\Delta E = 0$  eV, which yields elastic bright-field and dark-field images, whereas in (b)  $\Delta E > 0$  eV, which permits electron spectroscopic imaging with inelastically scattered electrons.

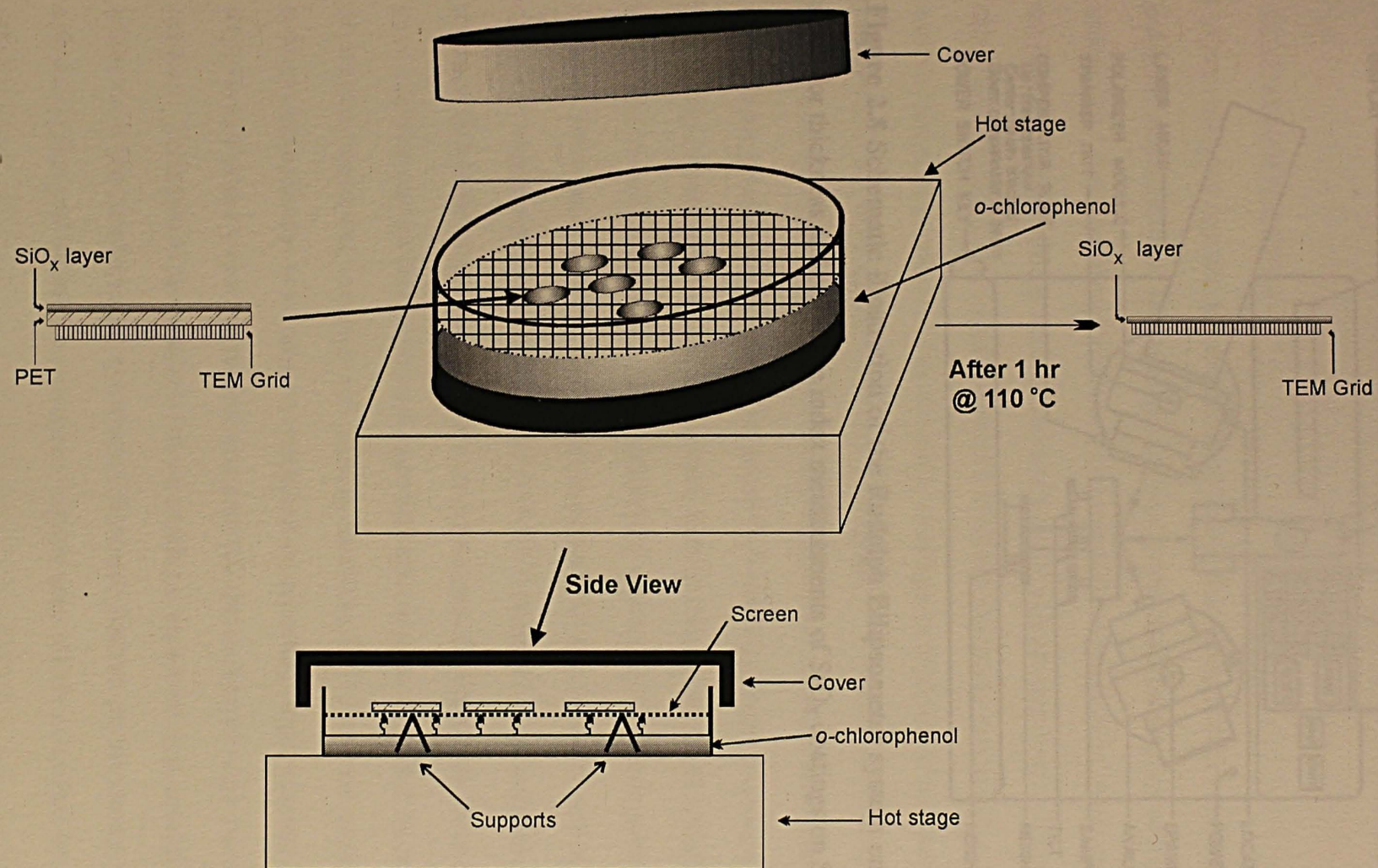


**Figure 2.7** Sample preparation method showing the necessary steps taken to isolate the  $\text{SiO}_x$  film.

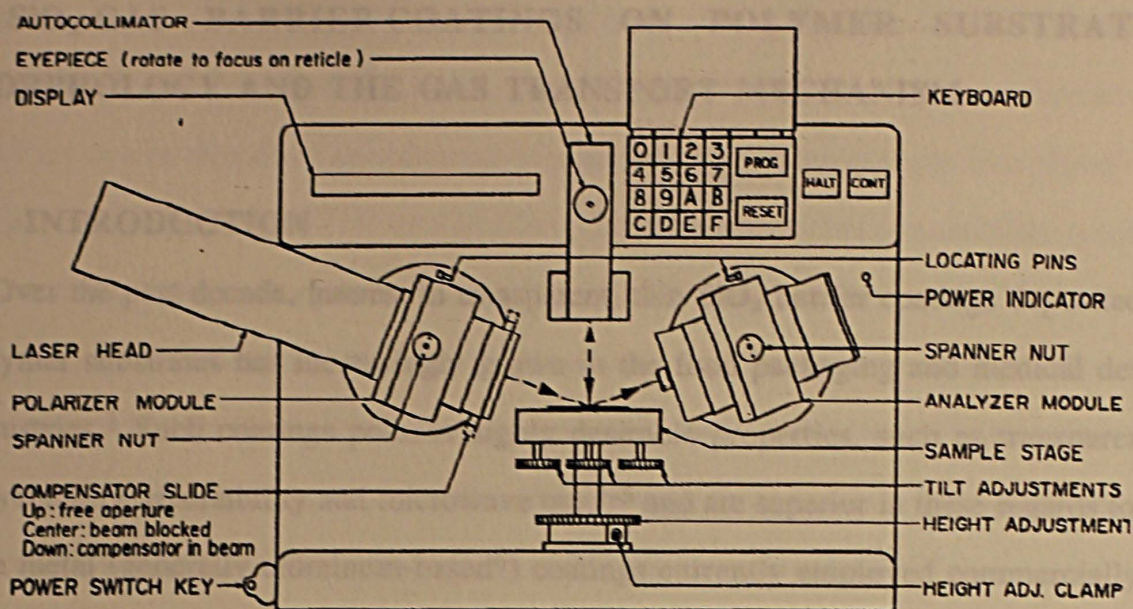


**Figure 2.8** Schematic illustration of the Rudolph Ellipsometer system employed in this study for thickness and refractive index measurements of  $\text{SiO}_x$  coatings on Si substrates.

water vapor permeability. Recent studies<sup>11-12</sup> of  $\text{SiO}_x$  coatings produced by different processing routes have, in fact, shown that both of these criteria are satisfied. One of the benefits of these coatings lies in the flexibility by which they can be deposited on a polymer surface. Thus far, sputtering,<sup>13-16</sup> electron-beam (EB) deposition<sup>17</sup> and plasma-enhanced chemical vapor deposition (PECVD)<sup>11,12,18-20</sup> have all been utilized successfully to produce  $\text{SiO}_x$  barrier coatings on polymer substrates. Of these, the latter has become the most popular due to its operational ease and efficiency, as signified by low-temperature deposition, improved coverage and process tunability.<sup>17-18</sup> Previous studies<sup>14-15</sup> of  $\text{SiO}_x$  coatings have, for the most part, concentrated on reporting improvements in (i) measured oxygen and water vapor permeabilities and (ii) the design of high-vacuum deposition systems. To improve the quality of these coatings, however, it is crucial to identify and understand the fundamental correlations between barrier performance, morphological characteristics and molecular transport, which may all be governed by the deposition conditions.

### 3. SiO<sub>x</sub> GAS BARRIER COATINGS ON POLYMER SUBSTRATES: MORPHOLOGY AND THE GAS TRANSPORT MECHANISM

#### 3.1 INTRODUCTION

Over the past decade, interest in transparent, thin SiO<sub>x</sub> barrier coatings deposited on polymer substrates has increasingly grown in the food packaging and medical device industries.<sup>1</sup> Such coatings possess highly desirable properties, such as transparency, recyclability, retortability and microwave use,<sup>1-5</sup> and are superior in these regards to the thin metal (generally aluminum-based<sup>6</sup>) coatings currently employed commercially on various polymer substrates. For the SiO<sub>x</sub> coatings to compete effectively against more established, as well as concurrently emerging,<sup>7-10</sup> barrier technologies, they must demonstrate time and temperature stability, and promote substantially reduced oxygen and water vapor permeability. Recent studies<sup>4,11,12</sup> of SiO<sub>x</sub> coatings produced by different processing routes have, in fact, shown that both of these criteria are satisfied. One of the benefits of these coatings lies in the flexibility by which they can be deposited on a polymer surface. Thus far, sputtering,<sup>13,14</sup> electron-beam (EB) deposition<sup>1,2</sup> and plasma-enhanced chemical vapor deposition (PECVD)<sup>11,13,15-16</sup> have all been utilized successfully to produce SiO<sub>x</sub> barrier coatings on polymer substrates. Of these, the latter has become the most popular due to its operational ease and efficacy, as signified by low-temperature deposition, improved coverage and process tunability.<sup>17-18</sup> Previous studies<sup>14-15</sup> of SiO<sub>x</sub> coatings have, for the most part, concentrated on reporting improvements in (i) measured oxygen and water vapor permeabilities and (ii) the design of high-vacuum deposition systems. To improve the quality of these coatings, however, it is crucial to identify and understand the fundamental correlation between barrier performance, morphological characteristics and molecular transport, which may all be governed by the deposition conditions.

Surface and sub-surface characterization of  $\text{SiO}_x$  coatings by atomic force microscopy (AFM)<sup>19-24</sup> and scanning electron microscopy (SEM)<sup>24-26</sup> reveal that the surface of such coatings can be described as columnar or granular, rather than pinhole-like. Roughness measurements performed<sup>23-24</sup> by AFM have likewise shown that permeability generally decreases with increasing surface smoothness. In light of these results, the principal structure of the coating regulating permeation is currently believed to consist of fine-scale (Angstrom- or nanometer-level) defects, instead of pores in  $\mu\text{m}$  range.<sup>26</sup> Such fine-scale defects induce highly tortuous molecular-size pathways through which penetrant molecules must diffuse before reaching the polymer substrate. Prior attempts<sup>25,27</sup> to examine these defects by cross-sectional high-resolution transmission electron microscopy (HRTEM) have met with limited success due to difficulties associated with sample preparation and defect identification. As a complement to morphological characterization, permeation activation energy measurements of  $\text{SiO}_x$  coatings on several commodity polymer substrates have been conducted by Tropsha et al.<sup>28</sup> To explain observed data trends, their study proposes a simplified defect model, which provides valuable insight into the mechanism (in terms of molecular tortuosity) dictating oxygen and water vapor permeation through the coatings. Recent results reported by Henry et al.<sup>27</sup> combine morphological and activation energy measurements obtained for a variety of gases, and support the existence of fine-scale defects, which vary in size and density (thereby yielding changes in barrier performance).

In the present study, the extensive statistical Non-Parametric Response Surface Methods (NPRSM) algorithm<sup>29</sup> has been applied to optimize the RF-discharge PECVD and obtain superior quality  $\text{SiO}_x$  barrier coatings deposited on poly(ethylene terephthalate) (PET) substrates. Results obtained from this experimental design facilitate comparison of coating microstructure, surface morphology and gas (oxygen and water vapor) transport mechanism of  $\text{SiO}_x$  coatings differing in barrier performance to identify statistically meaningful correlations. Moreover, planar, rather than cross-sectional, transmission

electron microscopy (TEM) is used to resolve the fine-scale defects in the  $\text{SiO}_x$  films alluded to above, whereas AFM provides insight into the growth mechanism and texture evolution of the coatings. Temperature-dependent permeation measurements acquired from oxygen and water vapor transport are analyzed in the context of thermally activated rate theory, and results are discussed here in light of the morphological characteristics discerned by TEM and AFM.

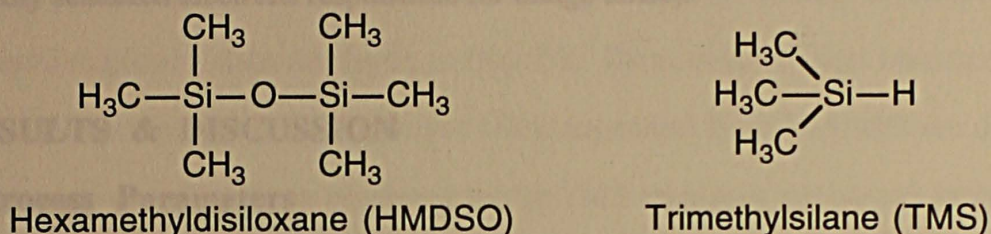
## 3.2 EXPERIMENTAL

### 3.2.1 Material Processing

The PET substrate employed here was obtained in sheet form from Atlantic Plastics (Raleigh, NC) and had a number-average molecular weight of 38,000 g/mol. It was extruded into a thin (25  $\mu\text{m}$  thick) film, which exhibited a degree of crystallinity of about 28% according to Differential Scanning Calorimetry measurements. The  $\text{SiO}_x$  coatings investigated in this work were deposited on these PET films (cut into 8 cm  $\times$  8 cm squares) at room temperature in a Magnetron, a magnetically enhanced PECVD apparatus schematically illustrated in Fig. 3.1 and described in detail elsewhere.<sup>30</sup> In the Magnetron, a magnetic field was superimposed on the 10 cm  $\times$  10 cm titanium vertical electrodes by placing ten bar magnets radially on the backside of each electrode, and two PET films sandwiched together were suspended symmetrically between the anode and cathode. Following this, the chamber was evacuated to below 1 torr using a roughing pump, whereupon the turbomolecular pump was activated. At this point, the flow rates of monomer and oxidizer, as well as the pressure, were adjusted. Upon system stabilization over the course of few minutes, the electrodes were energized, and the matching network was tuned to a predetermined power level. The deposition time was maintained constant at 3 min, after which time the power was turned off for a brief cool-down period. This process was repeated twice more for a total of three 3-min depositions/sample. At the end

of this deposition sequence, the chamber was vented and the two coated samples were carefully removed for testing.

Two series of PET/SiO<sub>x</sub> films were produced in this manner by feeding trimethylsilane (TMS) and hexamethyldisiloxane (HMDSO) monomers, supplied at 98% purity from United Chemical Technologies and Aldrich Chemicals (Milwaukee, WI), respectively, into the plasma chamber with oxygen at 99.5% purity from National Welders (Raleigh, NC). The chemical structures of the SiO<sub>x</sub>-forming monomers are displayed in Scheme I.



**Scheme I**

In each case, the three most important deposition parameters — power, oxygen flow rate and monomer flow rate — were varied according to results from the NPRSM optimization in order to operate at the optimum process conditions and thereby ensure superior barrier performance.

### 3.2.2 Material Characterization

Oxygen transmission measurements were performed over the course of 24 hrs on an Oxtran 2/20 permeability testing instrument (Modern Controls, Inc., Minneapolis, MN) at 10, 20, 30, 35 and 40°C. Water vapor transmission rates were measured under analogous conditions from 24 to 38°C with a Permatran W600 (Modern Controls, Inc.). A Digital Instruments Nanoscope D-3000 operated in tapping mode<sup>31</sup> provided phase and topographical images of SiO<sub>x</sub> coatings, as well as corresponding root-mean-square (rms) surface roughness measurements. Complementary TEM analysis was conducted on the SiO<sub>x</sub> coatings by using a method developed<sup>6</sup> for the examination of metallized Al coatings deposited on PET. Small pieces of the PET/SiO<sub>x</sub> composites were placed on 400-mesh

copper TEM grids, and the grids were arranged on a graphite screen elevated by metal supports in a petri dish. Upon addition of *o*-chlorophenol, the dish was covered and heated to 110°C, resulting in complete dissolution of the PET substrate over the course of 1 hr. [The lid was removed every 10 min in a fumehood to avoid condensation of *o*-chlorophenol vapor on the fragile SiO<sub>x</sub> film.] The resulting self-supported SiO<sub>x</sub> film was imaged on a Zeiss transmission electron spectroscopic microscope operated at 80 kV in zero-loss ( $\Delta E=0$  eV) imaging mode<sup>32</sup> to enhance phase contrast (by filtering out the inelastically scattered electrons responsible for image noise).

### 3.3 RESULTS & DISCUSSION

#### 3.3.1 Process Parameters

The NPRSM experimental design facilitates identification of the optimum settings of the Magnetron-PECVD process parameters responsible for minimizing oxygen permeation through the PET/SiO<sub>x</sub> composites. The experimental variables optimized during the course of this extensive statistical design include deposition power, expressed in watts, and the monomer and oxygen flow rates, both expressed in units of cm<sup>3</sup>(STP)/min (hereafter abbreviated as sccm for consistency with the literature). These are generally considered<sup>16,29</sup> to constitute the crucial process parameters governing film quality in a PECVD process. Additional process conditions, such as deposition time and cool down between depositions, have been held constant to ensure valid material comparison, whereas pressure and signal frequency must be adjusted according to the optimum parameters selected.

Process optimization is conducted separately for films coated with HMDSO and TMS monomers. Throughout this optimization, reactor constraints and process modifications define the experimental boundaries at each step of the experimental design. The optimization strategy for both monomers starts with a fractional factorial design, developed on the basis of previous information regarding the Magnetron-PECVD system,<sup>33</sup> as the

feasible operating regime. These initial conditions are listed in Table 3.1. Identification of these initial conditions is followed by fractional factorial designs, steepest ascent pathways, response surface designs, space-filling designs, and optimum search algorithms that all employ thin-spline models.<sup>34</sup> A detailed review providing the sequence of experiments resulting in this experimental design, as well as describing more fully the NPRSM optimization algorithm, is available elsewhere.<sup>28</sup> During the course of optimization, a reduction in oxygen transmission rate ( $\Pi_{O_2}$ ) is accompanied by increases in all three PECVD process parameters from their initial settings, thereby enabling construction of the comprehensive process map displayed in Fig. 3.2. Here, contour plots corresponding to the three optimum process conditions for films deposited from HMDSO are displayed. Similar contour plots have been generated for the TMS monomer but are not included here since the HMDSO-based coatings were studied more extensively, thereby yielding a more complete picture of the optimization model.

**Table 3.1.** Magnetron-PECVD deposition settings obtained from the NPRSM optimization.

Monomer	Settings	Power (W)	O <sub>2</sub> flow rate (sccm)	Monomer flow rate (sccm)
HMDSO	Initial	23 – 40	0.5 – 4.0	3.0 – 10
	Optimum	65	6.5	15.5
TMS	Initial	20 – 45	0.8 – 4.2	2.5 – 11
	Optimum	65	7.0	15.0

The effect of simultaneously varying power and HMDSO flow rate on  $\Pi_{O_2}$  is shown at a constant O<sub>2</sub> flow rate of 6.5 sccm in Fig. 3.2a. At the optimum HMDSO flow rate (*ca.* 15.5 sccm), the contour lines reveal a significant improvement in barrier performance (*i.e.*, reduced  $\Pi_{O_2}$ ) as the power level is increased. A bowl-shaped optimum in the vicinity of 65 W is eventually realized. This behavior is attributed to a more intense plasma in the glow

region and a corresponding increase in the kinetic energy of ions, resulting in enhanced ion bombardment, which improves the degree to which HMDSO and O<sub>2</sub> molecules dissociate to form dense and uniform SiO<sub>x</sub> networks.<sup>35</sup> Moreover, oxidation of elements such as carbon and hydrogen is complete under these conditions.<sup>30,35</sup> This constitutes an important consideration, since unwanted byproduct gases (e.g., CO, CO<sub>2</sub> and H<sub>2</sub>O) are formed at this power level and subsequently vented out of the plasma chamber, minimizing the level of impurities incorporated within the SiO<sub>x</sub> coating.

As is also evident in Fig. 3.2a, higher or lower HMDSO flow rates promote a significant (and highly undesirable) increase in  $\Pi_{O_2}$ . An insufficient HMDSO flow rate at any power level is expected to generate poor SiO<sub>x</sub> coatings due to premature monomer depletion, which would become more pronounced with increasing power (and HMDSO consumption). Premature HMDSO depletion would, in turn, result in incomplete surface coverage, non-uniform coating thickness and more defect sites, thereby increasing  $\Pi_{O_2}$ . Excess monomer at high HMDSO flow rates (particularly at low power levels), on the other hand, would leave unreacted species in the chamber upon plasma deactivation. These species would tend to deposit on the SiO<sub>x</sub> coating if they did not vent out of the chamber during deposition. The presence of such impurities in SiO<sub>x</sub> coatings can be highly detrimental to the coating chemistry and, hence, increase gas permeability.<sup>36</sup>

For comparison, Fig. 3.2b displays the effect of varying power and O<sub>2</sub> flow rate on  $\Pi_{O_2}$  at a constant HMDSO flow rate of 15.5 sccm. The role of power in this figure is the same as that discussed above with regard to Fig. 3.2a. At the optimum power level (*ca.* 65 W), a bowl-shaped minimum in  $\Pi_{O_2}$  is apparent, centered at an O<sub>2</sub> flow rate of about 6.5 sccm. Reduction in barrier performance at higher and lower O<sub>2</sub> flow rates can be explained in terms of coating properties. At higher O<sub>2</sub> flow rates, the corresponding SiO<sub>x</sub> coatings possess a higher oxygen content and become brittle (and prone to stress cracking).<sup>5</sup> Lower O<sub>2</sub> flow rates produce porous SiO<sub>x</sub> coatings with a high residual carbon content, since the byproduct gases mentioned earlier would not form completely and vent during

deposition.<sup>35</sup> Figure 3.2c represents the combinatorial effect of concurrently varying HMDSO and O<sub>2</sub> flow rates on  $\Pi_{O_2}$  at a constant power level of 65 W. As in the two previous figures, a minimum in  $\Pi_{O_2}$  is clearly resolved at HMDSO and O<sub>2</sub> flow rates of about 15.5 and 6.5 sccm, respectively. At a constant O<sub>2</sub> flow rate, the barrier efficacy of SiO<sub>x</sub> coatings degrades upon increasing or decreasing the HMDSO flow rate. At low flow rates, the formation of SiO<sub>x</sub> networks is hindered (despite plasma activation) due to HMDSO depletion, yielding non-uniform and insufficiently dense coatings. For the opposite case of excess HMDSO monomer, impurities again contaminate the SiO<sub>x</sub> coatings.

In the previous section, results from the NPRSM optimization have been compared with limited experimental data to demonstrate that subtle changes in Magnetron-PECVD deposition parameters could induce dramatic, and undesirable, increases in  $\Pi_{O_2}$ . An important consideration to be addressed at this juncture is whether the optimization parameters identified in Fig. 3.2 for  $\Pi_{O_2}$  could be legitimately extended to water vapor. This uncertainty is resolved in Fig. 3.3a, in which water vapor transmission rate ( $\Pi_{H_2O}$ ) is presented as a function of  $\Pi_{O_2}$  on double-logarithmic coordinates for a wide variety of SiO<sub>x</sub>-coated PET samples produced under different deposition conditions. While these data exhibit some scatter, they nonetheless demonstrate that an increase in  $\Pi_{O_2}$  is accompanied by an increase in  $\Pi_{H_2O}$  (the correlation coefficient, *r*, corresponding to the solid line shown in this figure is 0.92). Such correlation confirms that, although oxygen and water vapor possess vastly different properties (water vapor, *e.g.*, is highly condensable), (i) SiO<sub>x</sub> coatings constitute excellent barrier materials against both permeants, and (ii) the optimization results discussed earlier with respect to  $\Pi_{O_2}$  may be applied, at least on a semi-quantitative basis, to  $\Pi_{H_2O}$ .

The data compiled in Table 3.1 reveal that the optimum parameter settings for HMDSO and TMS are nearly identical, suggesting that the barrier performance of SiO<sub>x</sub> coatings produced from both monomers is comparable. This inference is supported by the data

provided in Fig. 3.3b. Here,  $\Pi_{\text{H}_2\text{O}}$  is shown as a function of  $\Pi_{\text{O}_2}$  for PET/SiO<sub>x</sub> composites in which the SiO<sub>x</sub> coating is derived from TMS monomer. Comparison of Figs. 3.3a and 3.3b reveals that (i) the  $\Pi_{\text{H}_2\text{O}}$ - $\Pi_{\text{O}_2}$  correlation identified for coatings from HMDSO is likewise valid for those generated from TMS, and (ii) coatings that exhibit similar barrier performance can be obtained from either HMDSO or TMS. This last point is in agreement with previous studies<sup>1</sup> in which different organosilicon monomers did not significantly influence the barrier efficacy of the resultant SiO<sub>x</sub> coatings. [The apparent improvement in coatings from HMDSO may reflect, in part, the more extensive HMDSO analysis alluded to earlier.] In comparing  $\Pi_{\text{O}_2}$  and  $\Pi_{\text{H}_2\text{O}}$  data from the same specimens (as is done in Fig. 3.3), an important point to note is that the O<sub>2</sub> measurement was performed prior to the water vapor measurement for two reasons. First, O<sub>2</sub> constitutes a better model permeant due to its established and relatively simplistic transport properties. For this reason, it is often employed in studies of barrier coatings,<sup>1-16</sup> whereas water vapor permeation can be problematic due to the preponderance of water molecules to hydrogen-bond in highly confined or porous environments.<sup>37</sup> The second reason for measuring  $\Pi_{\text{O}_2}$  before  $\Pi_{\text{H}_2\text{O}}$  is that water vapor is known<sup>38</sup> to induce structural changes in the SiO<sub>x</sub> matrix through stress cracking.

### 3.3.2 Morphological Characteristics

Atomic force microscopy has been employed in this study to identify (and quantify where possible) differences arising in surface morphology and roughness from samples exhibiting barrier efficacies ranging from 10 to 167× improvement in  $\Pi_{\text{O}_2}$  relative to the uncoated PET substrate ( $\Pi_{\text{O}_2}$ =80 cm<sup>3</sup>/m<sup>2</sup>-atm-day). For this comparison, samples with SiO<sub>x</sub> coatings produced from the TMS monomer have been selected along the  $\Pi_{\text{H}_2\text{O}}$ - $\Pi_{\text{O}_2}$  correlation evident in Fig. 3b. Images collected from 5 μm × 5 μm areas do not reveal macroscopic defects such as pinholes or macro-pores on the SiO<sub>x</sub> coating surface, in

agreement with results reported by Garcia-Ayuso,<sup>19</sup> who confirmed that pinholes are not fully responsible for measured permeabilities through SiO<sub>x</sub> coatings. The absence of such defects also reflects the relatively low  $\Pi_{O_2}$  values measured from the chosen samples (0.48–7.8 cm<sup>3</sup>/m<sup>2</sup>-atm-day). To ascertain if morphological features are at least partly responsible for the differences in  $\Pi_{O_2}$ , higher resolution 1  $\mu\text{m} \times 1 \mu\text{m}$  phase and oblique (3-D) images have been acquired from the coatings selected and are presented in Fig. 3.4. These images are representative of the surfaces and clearly show differences in surface texture (and growth mechanism) in SiO<sub>x</sub> coatings varying in barrier quality.

The phase images displayed in Fig. 3.4 show an obvious surface texture trend and are similar in appearance to those obtained by Wang et al.<sup>22</sup> for SiO<sub>x</sub> coatings generated from HMDSO monomer on polystyrene and polycarbonate substrates. Deposited near optimum PECVD conditions, the best coating is presented in Fig. 3.4a. Its surface is composed of densely packed, spherical clusters of SiO<sub>x</sub> networks (grains) with well-defined boundaries. The majority (75–80% of the total image area) of these features measure  $24 \pm 4$  nm, with larger features measuring  $56 \pm 13$  nm distributed randomly. Such fine uniform features are responsible for the low  $\Pi_{O_2}$  measured (0.48 cm<sup>3</sup>/m<sup>2</sup>-atm-day) since the penetrant molecules must locate and diffuse through the relatively few and small defect sites (due to the dense packing of particles) within the coating. As the deposition conditions are varied slightly from optimum, a poorer barrier coating ( $\Pi_{O_2}=1.5$  cm<sup>3</sup>/m<sup>2</sup>-atm-day) is produced. The surface texture of this coating is shown in Fig. 3.4b. Note that the shape of the SiO<sub>x</sub> clusters are irregular with sharper grain boundaries, which may favor the formation of defect sites. Another interesting characteristic of this figure is that the texture is composed of features that measure  $37 \pm 10$  nm across and that appear to coalesce into larger agglomerates measuring  $96 \pm 16$  nm in diameter. An increase in particle size is accompanied by an increase in grain boundary area. When this effect is combined with the irregular grain texture, it is anticipated that a greater number of penetrant molecules will diffuse through intergranular pores. In Fig. 3.4c, the surface morphology of a barrier coating

coating providing only a 10× improvement in barrier efficacy with respect to the uncoated PET substrate is displayed. This image clearly reveals that relatively large and irregularly shaped particle clusters (individual particles could not be resolved) comprise the SiO<sub>x</sub> coating, which appears to be very inhomogeneous due to a non-optimum deposition.

Insight into the permeation mechanism through PECVD-deposited SiO<sub>x</sub> coatings can be gleaned from the oblique (3-D) topographical images included in Fig. 3.4. The characteristic surface topography of SiO<sub>x</sub> coatings can be described as dome-shaped, as seen in the 3-D images. Upon comparing Figs. 3.3a–c, the domes are observed to deform and become irregular as the barrier performance degrades. When compared on a fixed vertical scale (z-range of 200 nm), the topography of the best barrier (Fig. 3.4a) appears to be composed of uniformly distributed, small columnar features, which become larger and irregular as the barrier performance decreases (Figs. 3.4b–c). The large domes create valleys that may not be completely covered with SiO<sub>x</sub>, thereby forming diffusive pathways in coatings that exhibit poor barrier quality. Such megalithic structures invariably change the rms surface roughness, which is shown in Fig. 3.5 as a function of  $\Pi_{O_2}$  for the AFM images provided in Fig. 3.4. Although a direct relationship has not yet been conclusively established, the surface roughness of SiO<sub>x</sub> coatings is believed to be a non-negligible factor affecting barrier performance.<sup>23,25</sup> Correlation between surface roughness and  $\Pi_{O_2}$  is evident in this figure, but more data are necessary to establish an indisputable relationship.

In the previous sections, the  $\Pi_{O_2}$  and  $\Pi_{H_2O}$  values clearly demonstrate a tremendous improvement in barrier performance relative to PET. These data nevertheless indicate that even the best SiO<sub>x</sub> coatings are not impermeable, in which case defects (pores) must create pathways through which penetrant molecules diffuse. Marked improvement in barrier efficacy, coupled with AFM results such as those presented in Fig. 3.4, implies that the best barrier coatings are completely devoid of macropores or pinholes. Thus, the defects governing O<sub>2</sub> and water vapor permeation through these coatings must be pores in the nanometer or even Angstrom size range. Previous attempts to identify such defects have

employed cross-sectional TEM<sup>25,27</sup> and planar SEM,<sup>24-26</sup> but defects in this size range have not been satisfactorily resolved. In the present work, planar TEM images have been collected to discern the presence, size and distribution of nanoscale defects in SiO<sub>x</sub> coatings varying in barrier effectiveness. Shown in Fig. 3.6 are energy-filtered TEM micrographs of two SiO<sub>x</sub> coatings derived from TMS monomer with  $\Pi_{O_2}$  values of 0.52 and 16 cm<sup>3</sup>/m<sup>2</sup>-atm-day, thereby providing a comparison between good and relatively poor barrier coatings.

The microstructure corresponding to a good SiO<sub>x</sub> barrier coating (Fig. 3.5a) is seen to consist of spherical SiO<sub>x</sub> particles, tightly packed and uniformly deposited. They range in diameter from 2 to 15 nm. The low level of contrast observed throughout the micrograph reflects the even coating thickness. Electron-opaque (dark) features distributed randomly in the images, can most likely be attributed to mass-thickness contrast due to the deposition conditions or sample preparation described earlier. It is also conceivable that these features represent particles that are richer in silicon (and lower in carbon) than the surrounding matrix. Features of opposite electron contrast (appearing light) are, however, of more interest here, since they identify defects (pores) through which penetrant molecules diffuse. For superior SiO<sub>x</sub> coatings, very few of these defects (about 5% of the image area) exist. They measure less than 1.0 nm. across (the lower limit cannot be determined with certainty due to the resolution limit of the microscope, estimated to be about 0.4 nm in zero-loss imaging mode). This size scale is consistent with the low  $\Pi_{O_2}$  obtained by depositing the coating at or near optimum conditions. Nanoscale defects are most clearly resolved in the image provided in Fig. 3.6b for a poor barrier coating. The first result worth noting in this image is the obvious and gross change in microstructure, in which the SiO<sub>x</sub> particles, of comparable size to those in Fig. 3.6a, no longer appear spherical in shape. Instead, the particles in Fig. 3.6b are deformed into irregular shapes possessing sharp boundaries. Moreover, the area percentage of intergranular defects has increased significantly to about 30% of the total area. Unlike those seen in Fig. 3.6a, the defects visible in Fig. 3.6b are

significantly larger, extending up to *ca.* 5 nm across . Pores this large will certainly accommodate a significant flux of either O<sub>2</sub> (molecular diameter of 0.33 nm) or water vapor (molecular diameter of 0.34 nm).

These results provide visual evidence to substantiate the hypothesis that the principal mechanism of molecular transport in the best SiO<sub>x</sub> coatings occurs through nanoscale intergranular pores in the Angstrom or nanometer size range. As the coating deposition deviates from the optimum process conditions listed in Table 3.1 and the barrier quality is degraded, the size and density of nanoscale defects increase markedly, resulting in coatings composed of irregularly shaped particles. One drawback of TEM images is that they are 2-D projections of 3-D features, in which case information regarding the precise shape of these pores through the coating is not possible without the use of transmission electron microtomography. The activation energy studies presented in the following section will, however, provide additional insight into this issue.

### 3.3.3 Permeation Mechanism

The temperature dependence of ideal molecular transport through silicon oxide glasses<sup>39-40</sup> and polymers below their glass transition temperature<sup>41</sup> can generally be represented by an Arrhenius equation of the form:

$$P = P_0 \exp(-\Delta G^\ddagger/RT) \quad (3.1)$$

Here,  $\Delta G^\ddagger$  is the thermal activation energy, R is the universal gas constant and T denotes absolute temperature. Equation 1, if applicable to the PET/SiO<sub>x</sub> composites investigated here, could be used to probe the nanostructure of the SiO<sub>x</sub> coatings, since  $\Delta G^\ddagger$  is expected to be sensitive to changes in the mechanism of molecular transport.<sup>28</sup> The transmission data displayed in Fig. 3.3 reflect more than 100 samples prepared according to the NPRSM optimization and measured at 25°C. Temperature-dependent P measurements have been acquired from a limited series of HMDSO-based SiO<sub>x</sub> coatings selected along the correlation evident in Fig. 3.3a, and representative data are presented in Arrhenius-type

fashion for both O<sub>2</sub> and water vapor transmission in Figs. 3.7a and 3.7b, respectively. In all cases, Arrhenius behavior is clearly observed, indicating that (i) permeation through SiO<sub>x</sub>-coated glassy polymers is thermally activated and (ii) Eq. 3.1 may be applied to analyze the data collected here.

**Table 3.2**  $\Delta G^\ddagger_{O_2}$  data

$\Delta G^\ddagger_{O_2}$ (kJ/mol)	$\Pi_{O_2}(T)$ (cm <sup>3</sup> /m <sup>2</sup> -atm-d)
30.4	0.44
31.2	0.66
32.2	1.5
29.5	2
27.3	7.8
29.6	13

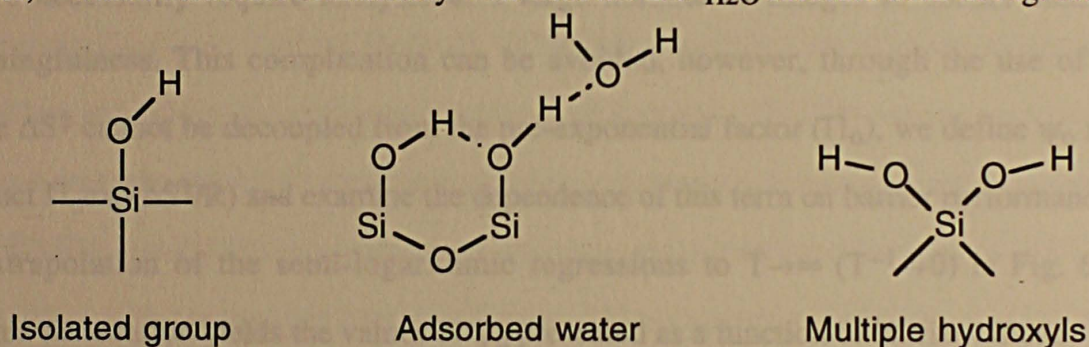
Values of  $\Delta G^\ddagger_{O_2}$  determined from  $\Pi_{O_2}(T)$  data are compiled in Table 3.2, and indicate that oxygen transmission through SiO<sub>x</sub>-coated PET ( $\Delta G^\ddagger_{O_2}=30\pm 2$  kJ/mol) and uncoated PET ( $\Delta G^\ddagger_{O_2}=29$  kJ/mol) transpires by the same mechanism, even if the barrier performance is increased by a factor of 182 $\times$ . This result supports the results of a previous study by Tropsha and Harvey,<sup>28</sup> who proposed that the particles comprising SiO<sub>x</sub> coatings serve as blockades which oxygen molecules must traverse to reach the PET substrate (where primary activated transport occurs). Invariance in the activation energy for O<sub>2</sub> transmission confirms that the SiO<sub>x</sub> coatings, despite their enhanced barrier performance, are not defect-free, in agreement with the TEM images shown in Fig. 3.6. In the present study, the Magnetron-PECVD conditions have been systematically varied to generate superlative barrier efficacy. As the barrier performance is increased and the size and density of defects are correspondingly reduced, one might suspect the eventual existence of a permeation regime in which the size of defects in the SiO<sub>x</sub> coating is of the same scale as the penetrant molecule. In this case, the permeant may be forced to diffuse along the axis

of its smallest projected area or be constricted in some other fashion, thereby causing an increase in  $\Delta G^\ddagger$ . While such behavior is observed<sup>42</sup> in  $\text{SiO}_x$  coatings produced from HMDSO by RF-discharge PECVD on polycarbonate, it is not reproduced in the  $\Pi_{\text{O}_2}$  data reported here due to differences in either the coatings (Magnetron-PECVD *vs.* RF-discharge PECVD) or the polymer substrates (semi-crystalline *vs.* glassy).

In marked contrast,  $\Delta G^\ddagger_{\text{H}_2\text{O}}$  for water vapor transmission through PET/ $\text{SiO}_x$  composites increases as the barrier quality improves. This relationship is displayed in Fig. 3.8, in which  $\Delta G^\ddagger_{\text{H}_2\text{O}}$  is presented as a function of  $\Pi_{\text{O}_2}$  on semi-logarithmic coordinates. Our reason for using  $\Pi_{\text{O}_2}$  as the independent (abscissa) variable is due to oxygen behaving as a nearly ideal penetrant expected to show very little (if any) physico-chemical interaction with the  $\text{SiO}_x$  surface. Thus, the  $\Pi_{\text{O}_2}$  data represent a reliable measure of barrier performance in the present study. According to Fig. 3.8,  $\Delta G^\ddagger_{\text{H}_2\text{O}}$  does not change for the poor quality barriers relative to the PET substrate ( $\Delta G^\ddagger_{\text{H}_2\text{O}}=50$  kJ/mol). At values of  $\Pi_{\text{O}_2}$  less than  $1 \text{ cm}^3/\text{m}^2\text{-atm-day}$ , however,  $\Delta G^\ddagger_{\text{H}_2\text{O}}$  clearly increases with decreasing  $\Pi_{\text{O}_2}$  (by up to about 20 kJ/mol for  $10\times$  improved barrier performance). This result questions the role of the  $\text{SiO}_x$  matrix, which appears to become the rate-limiting step, in the water vapor transport mechanism. As mentioned earlier with regard to oxygen permeation, it is plausible that the nanoscale defects in the  $\text{SiO}_x$  coatings with  $\Pi_{\text{O}_2}<1 \text{ cm}^3/\text{m}^2\text{-atm-day}$  are sufficiently small to physically hinder the diffusion of water molecules. In the case of water, however, an additional possibility must be considered: the water molecules may chemically interact with the  $\text{SiO}_x$  surface. In either case, additional energy would be required for the water molecules to continue permeating.

As reported<sup>26,28</sup> previously and substantiated here, permeation of small molecules through PECVD-deposited  $\text{SiO}_x$  coatings is defect-driven. Consider as a limiting case silica ( $\text{SiO}_2$ ) glass, which exhibits superior barrier properties due to highly constricted interstitial spaces in the Si–O lattice (the Si–O bond length is 0.15 nm). In this case,  $\Delta G^\ddagger_{\text{H}_2\text{O}}$  is about 84 kJ/mol for water vapor permeation through the matrix at elevated temperatures.<sup>43</sup> Since

$\Delta G^{\ddagger}_{H_2O}$  increases by at most 20 kJ/mol beyond that of the PET substrate in Fig. 3.8, it is obvious that the rate-limiting mechanism of water vapor transport in the present  $SiO_x$  coatings is not the same as in  $SiO_2$ . This does not, however, preclude the possibility that the size or shape of the nanoscale defects present in the best  $SiO_x$  coatings physically hinders the diffusion of water molecules. Another plausible explanation for the observed increase in  $\Delta G^{\ddagger}_{H_2O}$  with decreasing  $\Pi_{O_2}$  is due to water molecules chemically interacting with the  $SiO_x$  surface, especially in highly confined nanoscale environments. Studies of silica glass have shown<sup>37</sup> that dangling bonds (e.g., Si–O– or Si–) rapidly react with water to form SiOH groups. In addition, examination of the hydroxyl population on silica surfaces by infrared spectroscopy<sup>44,45</sup> suggests that even molecular water physically adsorbs to  $SiO_2$  in abundance. Hydrogen bonding between hydroxyl groups and silica can result in several different arrangements, depicted in Scheme II. Energy penalties required to distort a hydrogen bond arising from hydroxyl/silica coupling range from about 4 to 25 kJ/mol,<sup>46</sup> which coincides remarkably well with the  $\Delta G^{\ddagger}_{H_2O}$  increase seen in Fig. 3.8. In



**Scheme II**

light of these considerations, we propose that the observed increase in  $\Delta G^{\ddagger}_{H_2O}$  with decreasing  $\Pi_{O_2}$  is most likely due to the energy required to remove adsorbed water molecules from the walls of the nanoscale pores, although size-induced hindered diffusion should not be completely ruled out. Further microchemical analysis is necessary to decouple the relative importance of these two effects.

An alternative analysis of the  $\Delta G^{\ddagger}$  data obtained during the course of this study for both oxygen and water vapor permeation assists in elucidating the defect density of the  $SiO_x$

coatings. Since  $\Delta G^\ddagger$  for an isothermal process can generally be written as  $\Delta H^\ddagger - T\Delta S^\ddagger$ , Eq. 1 may be rewritten as

$$\Pi = \Pi_0 \exp(\Delta S^\ddagger/R) \exp(-\Delta H^\ddagger/RT) \quad (3.2)$$

In the preceding discussion, the  $\Pi_{O_2}(T)$  and  $\Pi_{H_2O}(T)$  data shown in Figs. 7a and 7b, respectively, have been examined in terms of the Arrhenius-type Eq. 3.1, in which case the slopes yield values of  $\Delta G^\ddagger$ . According to Eq. 3.2, these slopes explicitly yield the enthalpic contribution to the energy of activation, in which case  $\Delta H^\ddagger$  can be viewed as a coupled interaction energy describing both the diffusion and solubility of the penetrant molecules in a matrix (PET and/or  $SiO_x$ ). The corresponding entropic term ( $\Delta S^\ddagger$ ), on the other hand, characterizes the degree of disorder in the matrix and therefore provides a direct measure of the defect (pore) size/density. While TEM micrographs such as those displayed in Fig. 3.6 qualitatively demonstrate that the pore size and population (density) decrease with decreasing  $\Pi_{O_2}$ , a quantitative correlation founded on the basis of such investigation would necessarily require analysis of a large number of images to ensure statistical meaningfulness. This complication can be avoided, however, through the use of  $\Delta S^\ddagger$ . Since  $\Delta S^\ddagger$  cannot be decoupled from the pre-exponential factor ( $\Pi_0$ ), we define  $\psi_0$  as the product  $\Pi_0 \exp(\Delta S^\ddagger/R)$  and examine the dependence of this term on barrier performance.

Extrapolation of the semi-logarithmic regressions to  $T \rightarrow \infty$  ( $T^{-1} \rightarrow 0$ ) in Fig. 6a for oxygen permeation yields the values of  $\psi_0$  presented as a function of barrier efficacy ( $\Pi_{O_2}$  evaluated at 25°C) in Fig. 3.9. This figure shows that, despite limited experimental scatter attributed to different deposition conditions, an increase in  $\Pi_{O_2}$  clearly promotes an increase in  $\psi_0$ . Since  $\Delta H^\ddagger_{O_2}$  corresponding to oxygen in the  $SiO_x$  matrix is negligible ( $\Delta G^\ddagger_{O_2}$  is independent of  $\Pi_{O_2}$  from the data listed in Table 3.2), the increase in  $\psi_0$  with increasing  $\Pi_{O_2}$  confirms the existence of a correlation solely between defect size/density and barrier performance. Recall that the  $SiO_x$  coatings employed to generate the  $\Pi_{O_2}(T)$  data for oxygen permeation in Fig. 3.6a have also been employed to obtain the  $\Pi_{H_2O}(T)$  data in Fig. 3.6b. In this case, the defect size/density information embedded in  $\psi_0$  can be

used to probe the permeation mechanism of water vapor in these  $\text{SiO}_x$  coatings. Values of  $\Delta G^\ddagger$  (or, alternatively,  $\Delta H^\ddagger$ ) in Fig. 3.8 are observed to increase with decreasing  $\Pi_{\text{O}_2}$ , whereas the  $\psi_0$  data in Fig. 3.9 increase with increasing  $\Pi_{\text{O}_2}$ . It immediately follows that  $\Delta G^\ddagger$  (or  $\Delta H^\ddagger$ ) must increase with decreasing  $\psi_0$ , again indicating that energetic interactions between the penetrant molecules and the matrix (PET and/or  $\text{SiO}_x$ ) become more pronounced, due to either size or chemical considerations, as the size/density of nanoscale defects in the  $\text{SiO}_x$  matrix decreases.

### 3.4 CONCLUSIONS

In this study, the morphological characteristics and barrier efficacy of a large number of PET/ $\text{SiO}_x$  composites with  $\text{SiO}_x$  coatings (deposited from Magnetron-PECVD) widely ranging in oxygen and water vapor barrier quality have been examined to identify key correlations and explore the molecular mechanism by which oxygen and water vapor permeate through such composites. A statistical experimental design employing Non-Parametric Response Surface Methods (NPRSM) constitutes an efficient optimization algorithm, identifying the optimum conditions of important PECVD process parameters to produce coatings exhibiting superlative barrier performance. Preparation of  $\text{SiO}_x$  coatings from HMDSO and TMS monomers near optimum deposition conditions yields PET/ $\text{SiO}_x$  composites with comparable barrier efficacy. This observation indicates that the use of different organosilicon monomers in  $\text{SiO}_x$  deposition (by at least Magnetron-PECVD) does not significantly alter the resultant barrier performance.

Images from AFM reveal that the particle shape (i.e., surface texture) and topography of  $\text{SiO}_x$  coatings vary in a consistent manner as the coating barrier quality is diminished. Good barriers are characterized by the presence of densely packed, small  $\text{SiO}_x$  grains with a smooth surface. As the barrier performance degrades, the grains become irregularly shaped and coalesce into larger features, producing rougher surfaces and creating more defect sites. Planar TEM images of  $\text{SiO}_x$  coatings facilitate comparison of microstructure

and defect size/density between coatings differing in barrier quality. Intergranular defects as large as 5.0 NM across have been detected from such TEM images. Very few defects of this nature, typically smaller than 1.0 NM across, are visible in good coatings. As the barrier quality decreases, the change in particle shape from spherical to irregular promotes an increase in the size/density of nanoscale defect (pore) sites.

The principal mechanism of both oxygen and water vapor transport through  $\text{SiO}_x$ -coated PET occurs through nanoscale defects in the  $\text{SiO}_x$  coating, followed by activated transport through the PET matrix. Transmission measurements obtained as a function of temperature for both oxygen and water vapor permeation reveal that (i) the transport mechanism is thermally activated, and (ii)  $\text{SiO}_x$  coatings become rate-limiting only for water vapor. In the latter case, the activation energy is found to increase by as much as 20 kJ/mol beyond that attributable to permeation through the semi-crystalline PET matrix. This increase most likely reflects a combination of physically constrained water molecules and chemically interacting water molecules (via hydrogen bonding to the  $\text{SiO}_x$  surface) in defects measuring on the same size scale as the penetrant molecules in good  $\text{SiO}_x$  barrier coatings. On the basis of this observation, the entropic contribution to the activation energy is adopted as a measure of defect size/density and is found to increase monotonically with decreasing barrier performance.

9. Phillips, R.W., Mantoux, T., and LaGalbe, C. *Proceedings of the Society of Vacuum Coaters 36th Annual Technical Conference 1993*, Society of Vacuum Coaters, Albuquerque, NM, 307.

9. Phillips, R.W., Mantoux, T., and LaGalbe, C. *Proceedings of the Society of Vacuum Coaters 36th Annual Technical Conference 1993*, Society of Vacuum Coaters, Albuquerque, NM, 293.

10. Bedard, F., Beal, G., Dennick, M., Bove, J.P., Duzlop, H.M., and Jurek, M. *The Solid State* 1994, 247, 21.

11. Kuo, J.T., and Grubb, A.D. *Journal of Vacuum Science and Technology A* 1992, 10, 1873.

## REFERENCES

1. Krug, T., Ludwig, R. and Steiniger, G. *Proceedings of the Society of Vacuum Coaters 36th Annual Technical Conference 1993*, Society of Vacuum Coaters, Albuquerque, NM, 302.
2. Chahroudi, D. *Proceedings of the Society of Vacuum Coaters 34th Annual Technical Conference 1991*, Society of Vacuum Coaters, Albuquerque, NM, 130.
3. Chahroudi, D. *Proceedings of the Society of Vacuum Coaters 36th Annual Technical Conference 1988*, Society of Vacuum Coaters, Albuquerque, NM, 145.
4. Chahroudi, D. *Proceedings of the Society of Vacuum Coaters 36th Annual Technical Conference 1989*, Society of Vacuum Coaters, Albuquerque, NM, 29.
5. Krug, T.G. *Proceedings of the Society of Vacuum Coaters 36th Annual Technical Conference 1990*, Society of Vacuum Coaters, Albuquerque, NM, 163.
6. Jamieson, E.H.H. and Windle, A.H. *Journal of Materials Science* **1983**,18, 64.
7. Misiano, C., Simonetti, E., Stafetti, F. and Taglioni, G. *Proceedings of 6th International Conference on Vacuum Web Coating 1992*, Bakish Materials Corp., Englewood, NJ, 70.
8. Misiano, C., Simonetti, E., Cerolini, P., Stafetti, F., Taglioni, G., Pasqui, A. and Fusi, F. *Proceedings of the Society of Vacuum Coaters 36th Annual Technical Conference 1993*, Society of Vacuum Coaters, Albuquerque, NM, 307.
9. Philips, R.W., Markantes, T. and LeGallee, C. *Proceedings of the Society of Vacuum Coaters 36th Annual Technical Conference 1993*, Society of Vacuum Coaters, Albuquerque, NM, 293.
10. Bodino, F., Baud, G., Benmalek, M., Besse, J.P., Dunlop, H.M. and Jacquet, M. *Thin Solid Films* **1994**,241, 21.
11. Felts, J.T. and Grubb, A.D. *Journal of Vacuum Science and Technology A* **1992**,10, 1675.

12. Langowski, H.C. *Proceedings of the Society of Vacuum Coaters 36th Annual Technical Conference 1996*, Society of Vacuum Coaters, Albuquerque, NM, 398.
13. Mercea, P.V. and Bartan, M. *Journal of Membrane Science 1991*, 59, 353.
14. Felts, J.T. *Proceedings of the Society of Vacuum Coaters 33rd Annual Technical Conference 1990*, Society of Vacuum Coaters, Albuquerque, NM, 184.
15. Nelson, R.J. *Proceedings of the Society of Vacuum Coaters 35th Annual Technical Conference 1992*, Society of Vacuum Coaters, Albuquerque, NM, 75.
16. Knoll, R.W. and Theil, J.A. *Proceedings of the Society of Vacuum Coaters 38th Annual Technical Conference 1995*, Society of Vacuum Coaters, Albuquerque, NM, 425.
17. Jansen, F. *American Vacuum Society Short Course Program, 43rd National Symposium*, American Vacuum Society, Philadelphia, 1996.
18. Vossen, J. and Kern, W., eds., *Thin Film Processes II*, Academic Press, Boston, 1991, pp. 443-496.
19. Garcia-Ayuso, G., Vazquez, L. and Martinez-Duart, J.M. *Surface & Coatings Technology 1996*, 80, 203.
20. Barker, C.P, Kochem, K.H., Revell, K.M., Kelly, R.S.A. and Badyal, J.P.S. *Thin Solid Films 1995*, 46, 259.
21. Mallik, R.R., Henriksen, P.N., Butler, T., Kulnis, W.J. and Confer, T.J. *Journal of Vacuum Science and Technology A, 1992*, 10, 2412.
22. Wang, B.-C., Erlat, A.G., Spontak, R.J., Tropsha, Y. G., Vogler, E.A., Dalvie, M. and Már, K. *ACS Polymer Preprints 1997*, 38, 1018.
23. Benmalek, M. and Dunlop, H.M. *Surface & Coatings Technology 1995*, 76, 821.
24. Thyen, R., Weber, A. and Klages, C.P. *Surface & Coatings Technology 1997*, 97, 426.

25. Philips, R.W., Markantes, T. and LeGallee, C. *Proceedings of the Society of Vacuum Coaters 36th Annual Technical Conference 1993*, Society of Vacuum Coaters, Albuquerque, NM, 293.
26. Roberts, A.P., Henry, B.M., Sutton, A.P., Gorvenor, C.R.M. and Briggs, G.A.D. to be submitted to *Journal of Physical Chemistry B*.
27. Henry, B.M., Roberts, A.P., Grovenor, C.R.M., Sutton, A.P., Briggs, G.A.D., Tsukahara, Y., Miyamoto, Yanaka, M. and Chater, R.J. *Proceedings of the Society of Vacuum Coaters 41st Annual Technical Conference 1998*, Society of Vacuum Coaters, Albuquerque, NM, 434.
28. Tropsha, Y.G. and Harvey, N.G. *Journal of Physical Chemistry B* **1997**, *101*, 2239.
29. Haaland, P.D., Clarke, R., O'Connell, M., Baik, J., Hardy, S. and Nychka, D. *Non-Parametric Response Surface Methods, 1997*, presented at Workshop on Topics in Model Fitting and Mixture Experiments, Irsee, Germany.
30. Yasuda, H. *Plasma Polymerization*, Academic Press, Inc., New York, 1985, pp. 277-333.
31. Martin, Y., Williams, C.C. and Wichramasinghe, G.H. *Applied Physics* **1987**, *61*, 4723.
32. Reimer, L., ed., *Energy-Filtering Transmission Electron Microscopy* Springer-Verlag, New York, 1995.
33. Williams, J.L., Burkett, S.L. and McGuire, S. *U.S. Patent #5,364,666* 15 November 1994.
34. Green, P.J. and Silverman, B.W. *Nonparametric Regression and Generalized Linear Models*, Chapman and Hall, London, 1994.
35. Lee, J.H., Kim, D.S. and Lee, Y.H. *Journal of the Electrochemical Society* **1996**, *143*, 1442.

36. Theil, J.A., Brace, J.G. and Knoll, R.W. *Journal of Vacuum Science and Technology A* **1994**, 12, 1365.
37. Doremus, R.H. *Glass Science* John wiley & Sons, London, 1973.
38. Michalske, T.A. and Bunker, B.C. *Scientific American* **1987**, 257, 122.
39. Perkins, W.G. and Begeal, D.R. *Journal of Chemical Physics* **1971**, 54, 1683.
40. Norton, F.J. *Journal of American Ceramic Society* **1953**, 36, 90.
41. Stannet, V. in *Diffusion in Polymers* (Crank, J. ed.), Academic Press, New York, **1968**, pp. 41-73.
42. Erlat, A.G., Wang, B., Spontak, R.J., Tropsha, Y., Mar, K.D., Montgomery, D.B and Vogler, E.A. *Journal of Materials Research* (submitted).
43. Moulson, J. and Roberts, T.P. *Transactions of the Faraday Society* **1961**, 57, 1208.
44. McDonald, R.S. *Journal of Physical Chemistry* **1958**, 62, 1168.
45. Little, L.H. *Infrared Spectra of Adsorbed Species*, Academic, London, 1966.
46. Eisenberg, D. and Kauzmann, W. *The Structure and Properties of Water*, Clarendon Press, Oxford, 1969, p. 179.

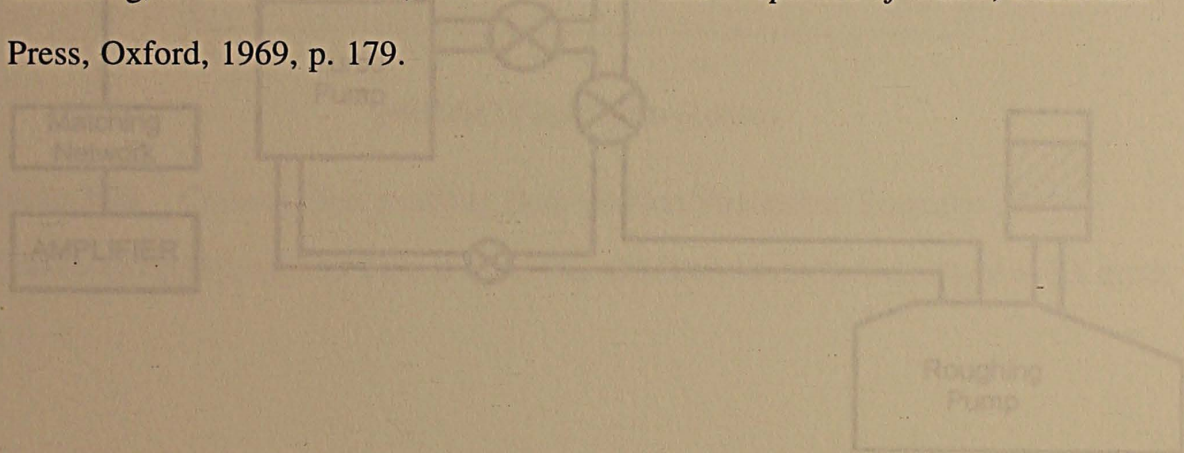
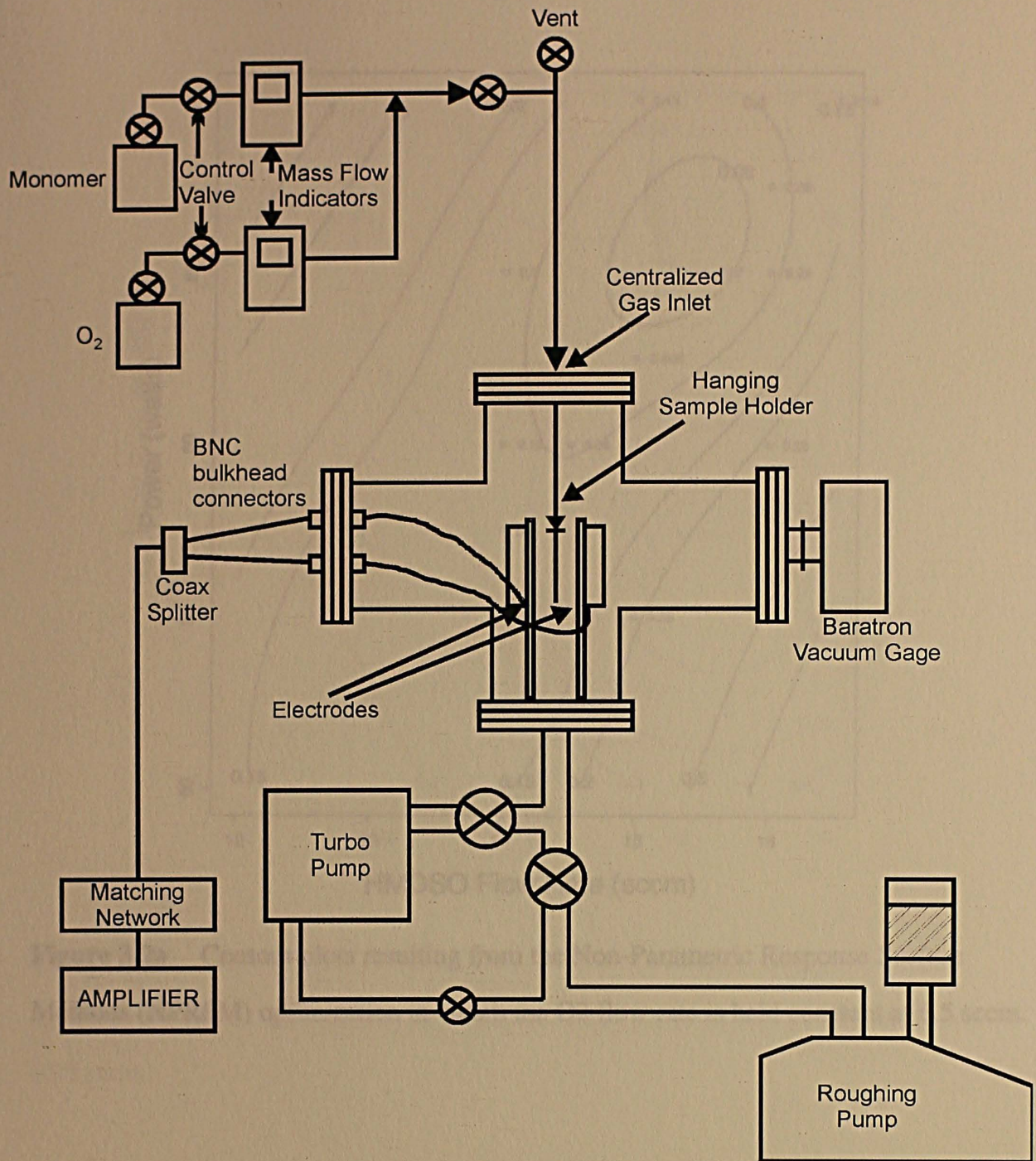
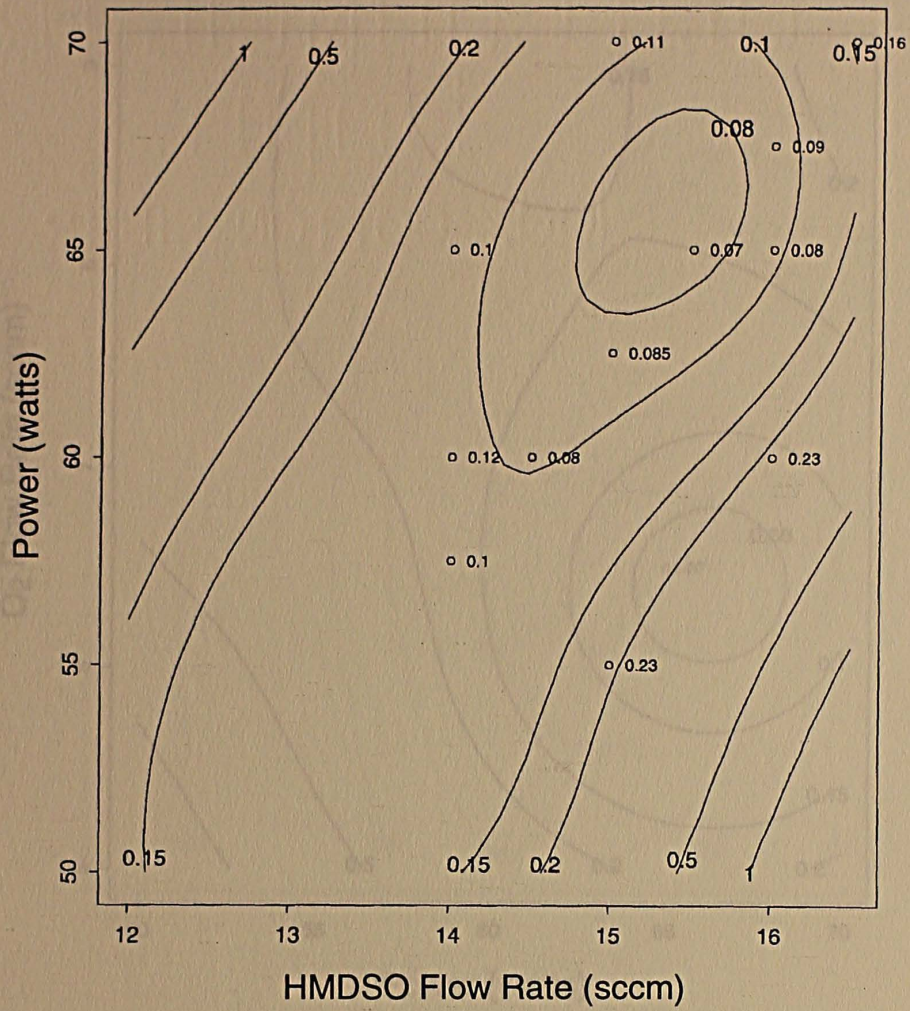


Figure 3.1 Schematic diagram of the Magnetron Plasma Deposition System used here to deposit SiO<sub>2</sub> on PET substrates.



**Figure 3.1** Schematic diagram of the Magnetron Plasma Deposition System used here to deposit SiO<sub>x</sub> on PET substrates.



**Figure 3.2a** Contour plots resulting from the Non-Parametric Response Surface Methods (NPRSM) optimization in which the O<sub>2</sub> flow rate is held constant at 6.5 sccm.

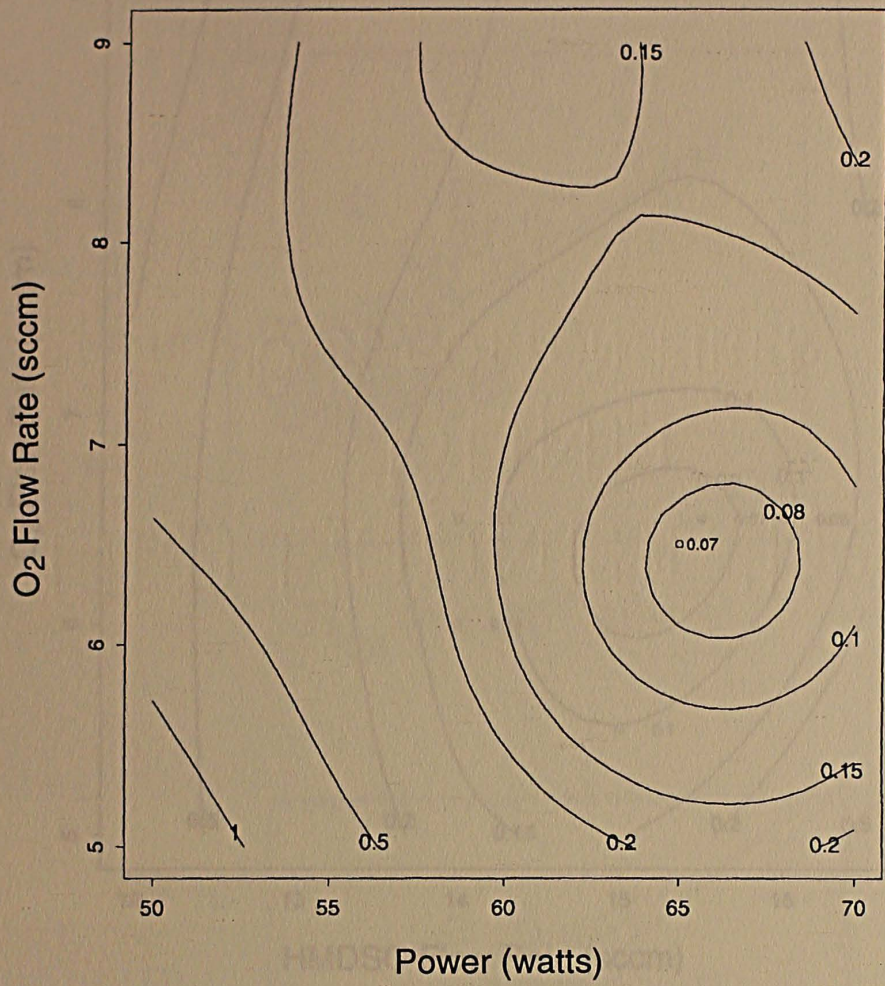


**Figure 3.2b** Contour plots resulting from the Non-Parametric Response Surface Methods (NPRSM) optimization in which the HMDSO flow rate is held constant at 15.5 sccm.

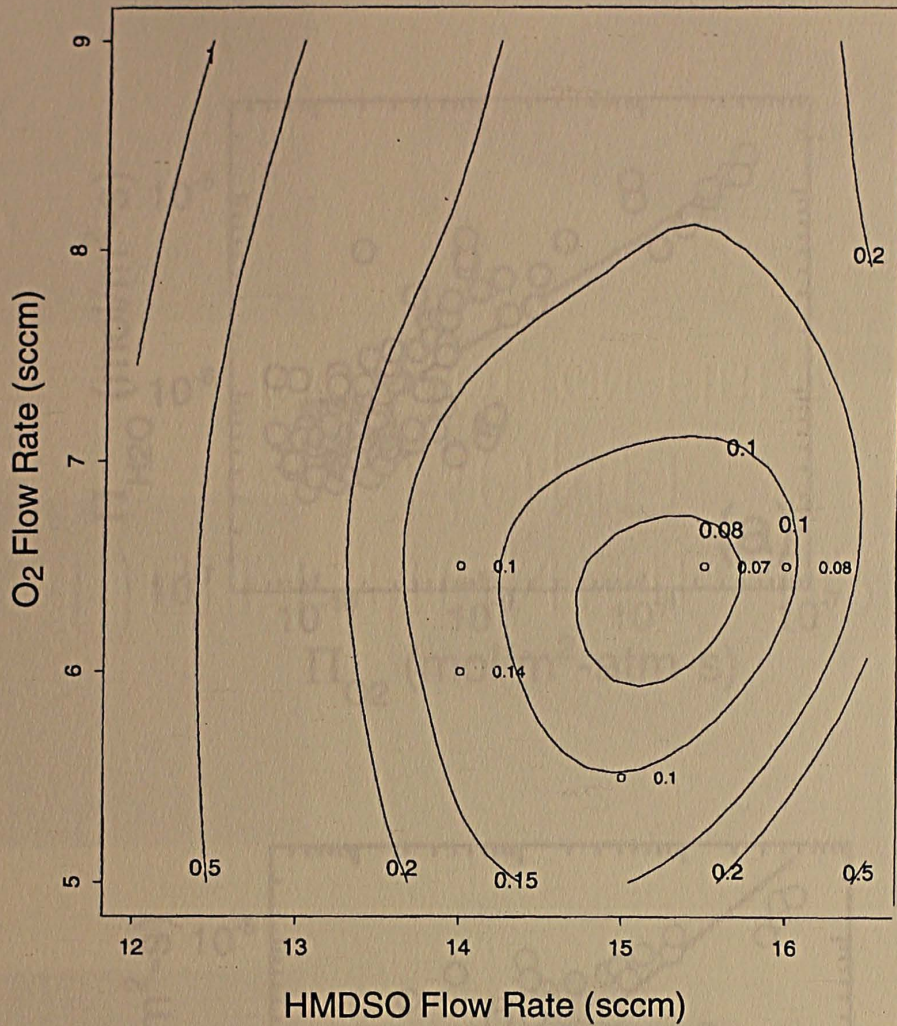


**Figure 3.2c** Contour plots resulting from the Non-Parametric Response Surface Methods (NPRSM) optimization in which the power level is held constant at 65 W.

Figure 3.3 Variation of the water vapor transmission rate ( $\Pi_{H_2O}$ ) with oxygen transmission rate ( $\Pi_{O_2}$ ) on double-logarithmic coordinates for SiO<sub>2</sub>-coated PET in which the SiO<sub>2</sub> layer is derived from (a) HMDSO and (b) TMS monomer. The solid line is a power-law fit to the data.

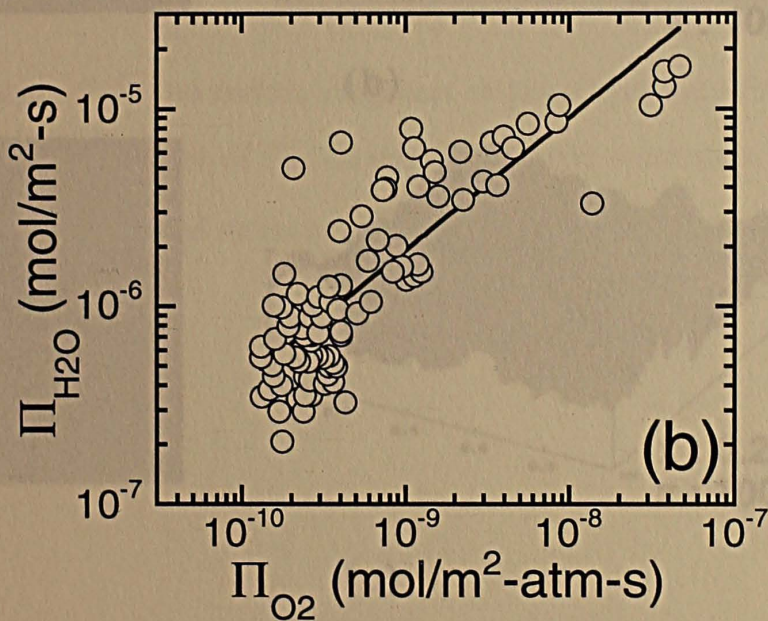
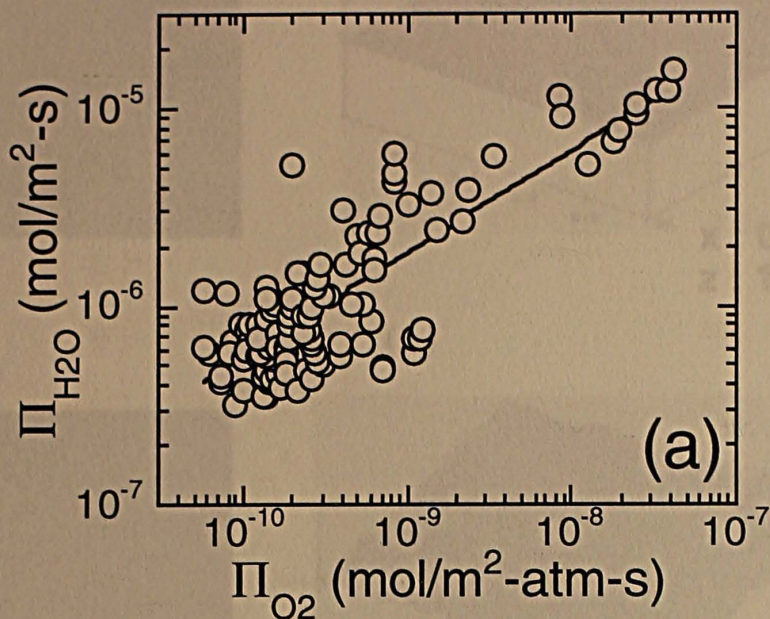
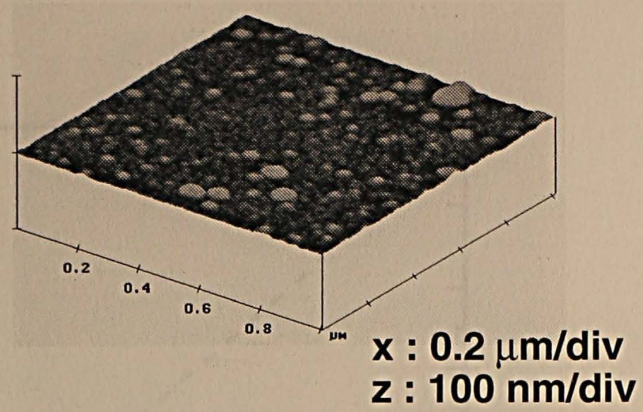
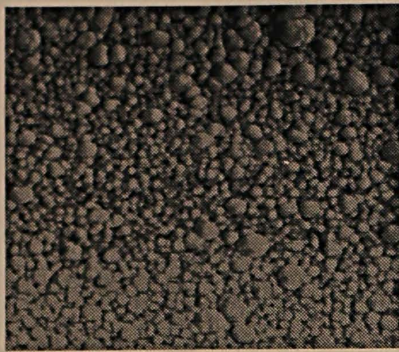
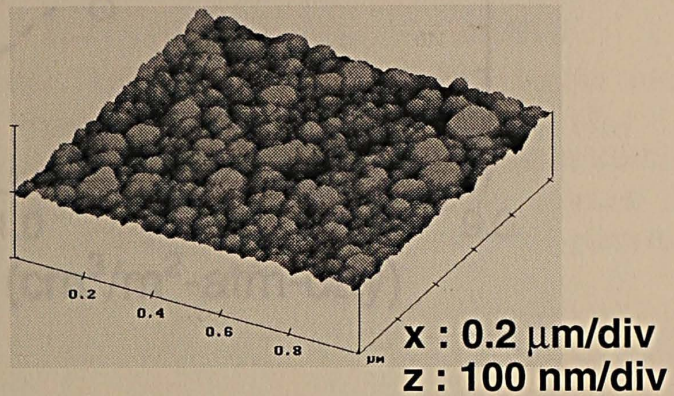


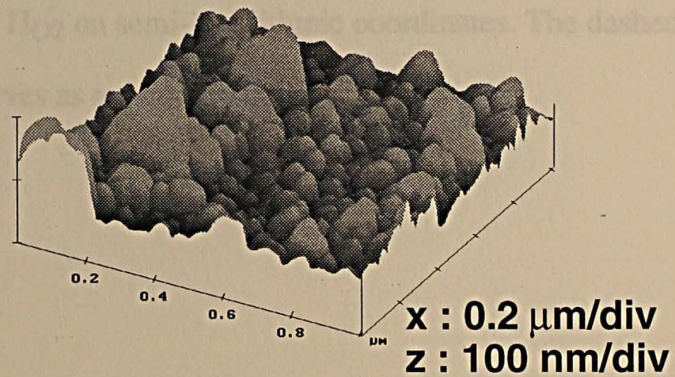
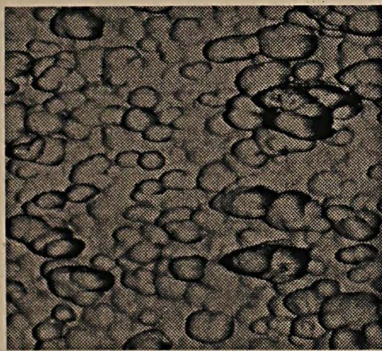
**Figure 3.3** Variation of the water vapor transmission rate ( $\Pi_{\text{H}_2\text{O}}$ ) with oxygen transmission rate ( $\Pi_{\text{O}_2}$ ) on double-logarithmic coordinates for  $\text{SiO}_x$ -coated PET in which the  $\text{SiO}_x$  layer is derived from (a) HMDSO and (b) TMS monomer. The solid line is a power-law fit to the data.



(a)



(b)



(c)

**Figure 3.4** Series of 1  $\mu\text{m}$  atomic force microscopy (AFM) images obtained in tapping mode from  $\text{SiO}_x$  coatings exhibiting different levels of barrier performance, as measured in terms of the oxygen transmission rate ( $\Pi_{\text{O}_2}$ , expressed in  $\text{cm}^3/\text{m}^2\text{-atm-day}$ ): (a) 0.48, (b) 1.5 and (c) 7.8.

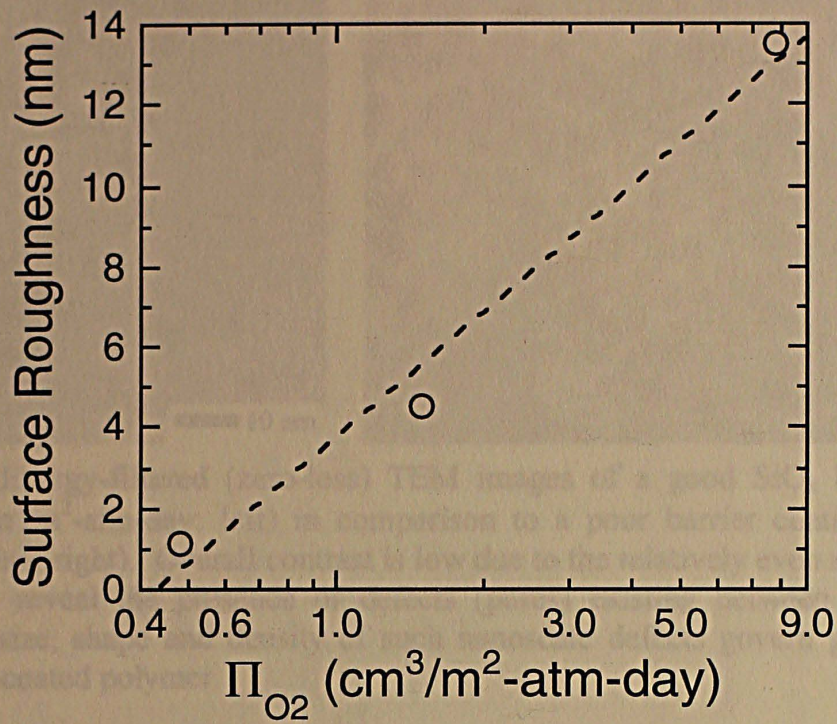


**Figure 3.5** Values of the rms surface roughness obtained from the AFM images in Fig. 4 and presented here as a function of  $\Pi_{O_2}$  on semi-logarithmic coordinates. The dashed line is a logarithmic fit to the data and serves as a guide for the eye.

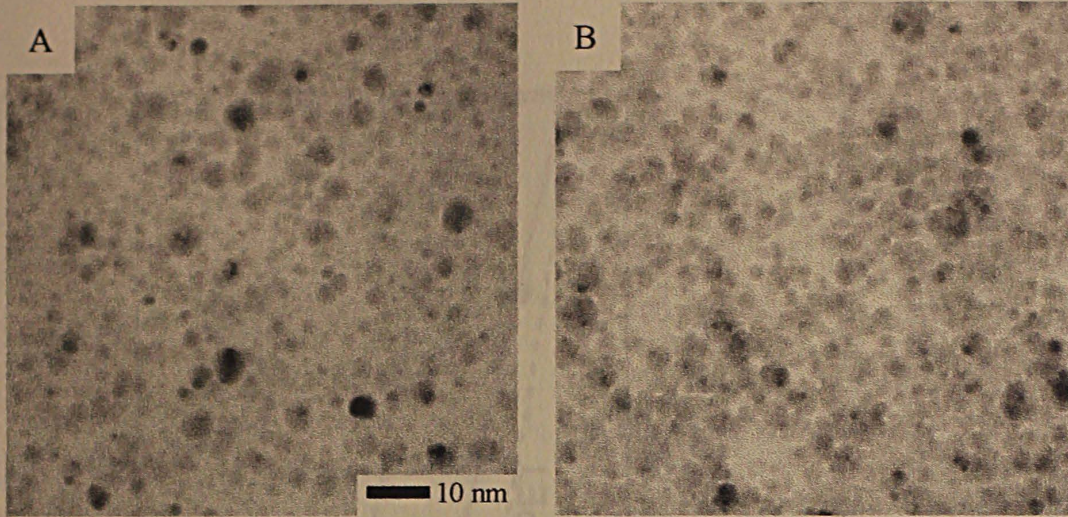


**Figure 3.6** Energy-filtered (zero-loss) TEM images of a good  $\text{SiO}_x$  barrier coating ( $\Pi_{\text{O}_2}=0.48 \text{ cm}^3/\text{m}^2\text{-atm-day}$ ; left) in comparison to a poor barrier coating ( $P_{\text{O}_2} = 7.8 \text{ cm}^3/\text{m}^2\text{-atm-day}$ ; right). Overall contrast is low due to the relatively even mass thickness. Enlargements reveal the presence of defects (pores) existing between adjacent  $\text{SiO}_x$  grains. The size, shape and density of such nanoscale defects govern gas permeation through  $\text{SiO}_x$ -coated polymer.

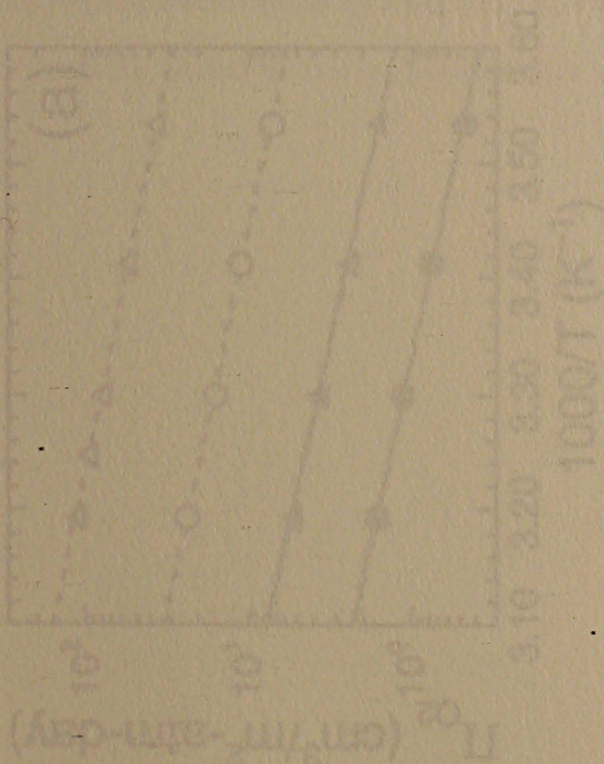


**Figure 3.7** Dependence of (a) oxygen transmission rate ( $\Pi_{\text{O}_2}$ ) and (b) water vapor transmission rate ( $\Pi_{\text{H}_2\text{O}}$ ) on  $1000/T$  for four  $\text{SiO}_x$  coatings produced under various conditions to yield different barrier properties. The data were fitted to the Arrhenius-type equation:  $\Pi = P_0 \exp(-E_a/RT)$ . The solid lines are the fits to the data. The dashed line is the fit to the data for the low- $P_{\text{O}_2}$  data.

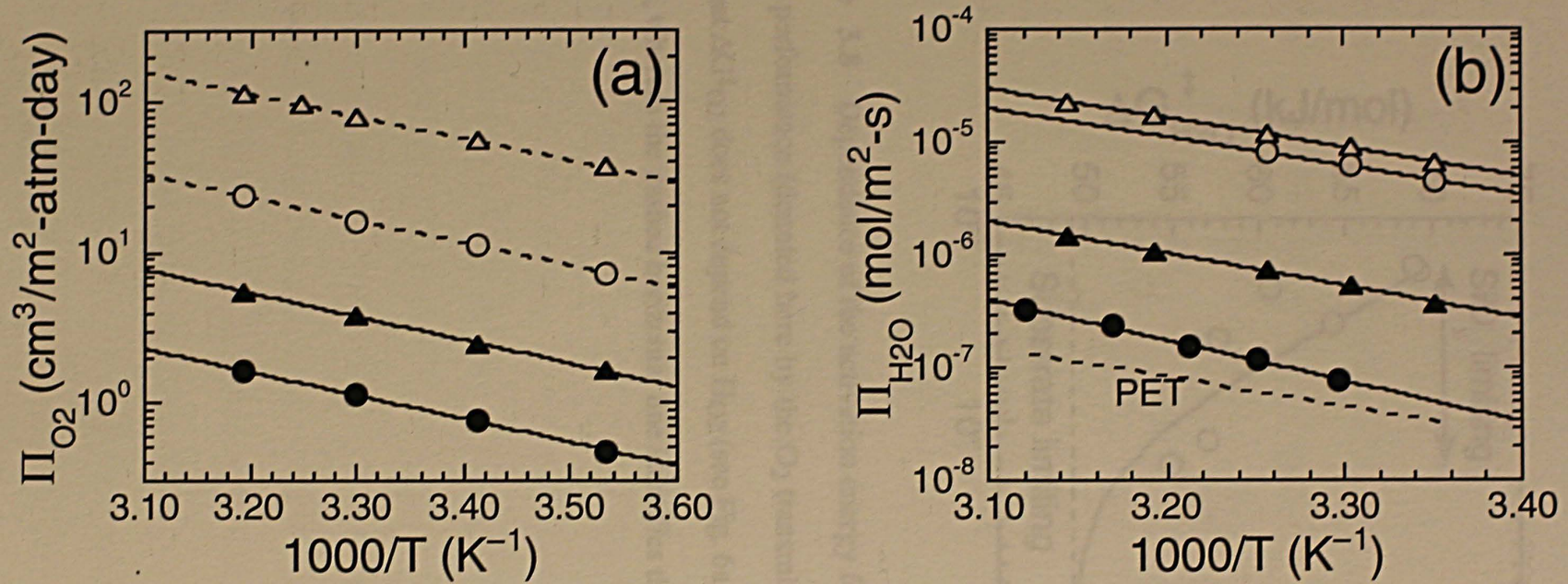


**Figure 3.7** Dependence of (a) oxygen transmission rate ( $\Pi_{O_2}$ ) and (b) water vapor transmission rate ( $\Pi_{H_2O}$ ) on reciprocal temperature for four  $SiO_x$  coatings produced under various conditions to yield different barrier performance, compared in terms of  $\Pi_{O_2}$  at 30°C (in  $cm^3/m^2\text{-atm-day}$ ): 0.18 ( $\bullet$ ), 1.6 ( $\blacktriangle$ ), 16 ( $\circ$ ) and 80 (PET,  $\Delta$ ). The solid lines are exponential fits to the data, in which case these data exhibit Arrhenius-type temperature dependence (see Eq. 1). The dashed line in (b) reflects uncoated PET and is shown to facilitate comparison of the slopes from the low- $\Pi_{O_2}$  data.

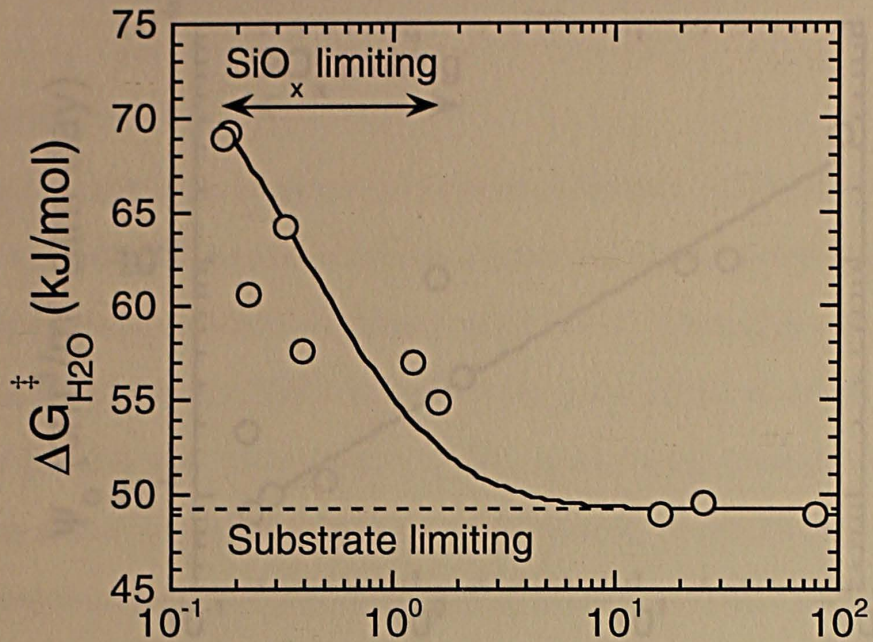


**Figure 3.8** Dependence of the activation energy for H<sub>2</sub>O transport ( $\Delta G_{H_2O}^\ddagger$ ) on SiO<sub>x</sub> barrier performance (denoted here by the O<sub>2</sub> transmission rate,  $\Pi_{O_2}$ , evaluated at 30°C). Note that  $\Delta G_{O_2}^\ddagger$  does not depend on  $\Pi_{O_2}$  (see Fig. 6a) The solid line serves as a guide for the eye, whereas the dashed horizontal line identifies the PET substrate limit.

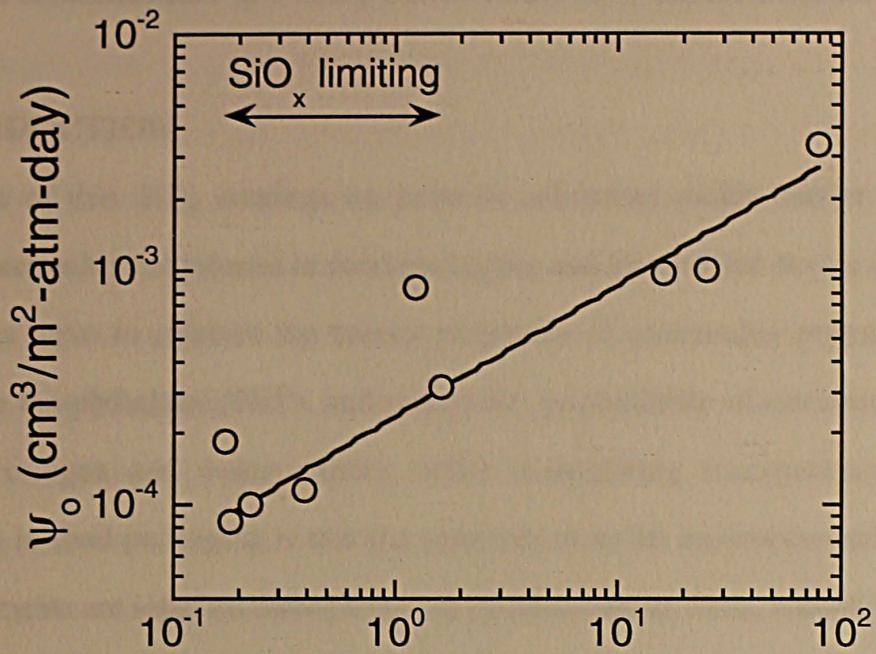


**Figure 3.9** Variation of  $\psi_0$  [ $=\Pi_{O_2}\exp(\Delta S^\ddagger/R)$ ] for  $O_2$  permeation with  $SiO_x$  barrier performance ( $\Pi_{O_2}$ ) suggesting a correlation between  $\Delta S^\ddagger$ , a measure of defect size/density, and barrier quality. The solid line serves as a guide for the eye.

## 4. EFFECT OF PECVD CONDITIONS ON THE MORPHOLOGY AND GAS BARRIER PROPERTIES OF SiO<sub>x</sub> COATINGS ON POLYCARBONATE

### 4.1 INTRODUCTION

Deposition of thin SiO<sub>x</sub> coatings on polymer substrates yields barrier materials of tremendous technological interest in food packaging and biomedical device industries.<sup>1-5</sup> Such coatings serve to enhance the barrier properties of commodity polymers, such as poly(ethylene terephthalate) (PET), and reduce the permeability of environmental gases (principally oxygen and water vapor), while maintaining transparency. Another consideration in food packaging is that the materials must be microwave-safe. Not all of these requirements are satisfied through the use of other barrier films, including the widely used aluminized coatings.<sup>6</sup> In the medical industry, concern regarding the spread of highly infectious diseases among medical and laboratory personnel has expedited replacement of brittle glass with tough polymeric materials in the production of devices such as the evacuated blood collection tubes. In these applications, optical transparency (required for spectroscopic analysis<sup>7,8</sup>) and impermeability can not be compromised to ensure proper device function. Transparency is retained by the judicious combination of high-barrier SiO<sub>x</sub> thin coatings and either amorphous (glassy) polymers (e.g., polycarbonate) or clarified<sup>9,10</sup> (nucleated) semi-crystalline polymers (e.g., polypropylene).

A wide variety of deposition techniques have been developed to deposit SiO<sub>x</sub> thin films on various substrates. The primary techniques most often employed include sputtering,<sup>11,12</sup> electron-beam (EB) deposition<sup>1,2</sup> and plasma-enhanced chemical vapor deposition (PECVD).<sup>11,13,14</sup> The present study focuses exclusively on PECVD, which is used extensively in the microelectronics industry to deposit silicon oxide thin films for electrical insulation purposes.<sup>15,16</sup> Only recently has PECVD — with its unique advantages such as low- (ambient-) temperature deposition, uniform coating formation and controllable process parameters — emerged as a valuable tool in depositing SiO<sub>x</sub> thin films from

organosilicon monomers.<sup>17-19</sup> Most fundamental studies<sup>19</sup> addressing the importance and flexibility of PECVD deposition have focused on methods by which to improve a particular PECVD system. Such improvement is typically achieved through analysis of effects resulting from variation of the most important process parameters, such as power, pressure, time and gas flow rates. In contrast to these traditional PECVD efforts, a statistically designed experimental study<sup>20</sup> has been recently performed with the dual purposes of (i) identifying the optimum PECVD process parameters to obtain the best possible barrier coating, and (ii) elucidating the oxygen and water vapor permeation mechanisms through the polymer/SiO<sub>x</sub> composite structures.

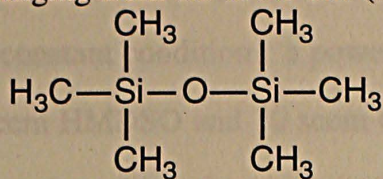
The principal objective of the present study is to ascertain, in systematic fashion, the effects of deposition time, power, pressure and gas flow rates on a variety of SiO<sub>x</sub> coating properties, including oxygen transmission rate, coating thickness, refractive index and surface morphology. These coatings are, in all cases, deposited on an amorphous polycarbonate (PC) substrate. Furthermore, the mechanism of molecular transport through the PC/SiO<sub>x</sub> laminates is analyzed in terms of activated rate theory. Activation energies are calculated from oxygen transmission rates measured from a broad spectrum of PC/SiO<sub>x</sub> composites and are compared, on a quantitative basis, in terms of barrier performance and discussed in the context of earlier findings.

## 4.2 EXPERIMENTAL

### 4.2.1 Material Processing

Polycarbonate with a number-average molecular weight of 20,000 to 40,000 g/mol, was obtained from Atlantic Plastics (Raleigh, NC) in sheet form and extruded into a thin film measuring 0.18 mm thick. Each SiO<sub>x</sub> coating was deposited on a 8 cm × 8 cm square of the polycarbonate film, as well as on Si and KBr substrates, in a radio-frequency (RF) discharge PECVD system, described in detail elsewhere<sup>21</sup> and schematically illustrated in Fig. 4.1. For the deposition, a polymer film was placed on the electrodes, and the chamber

was evacuated to below 0.7 Pa. The vapor of an organosilicon monomer (hexamethyldisiloxane, HMDSO, shown in Scheme I) and an oxidizer ( $O_2$ ) were admitted into the chamber at flow rates ranging from 1.5 to 3.5  $cm^3$ (STP)/min



Hexamethyldisiloxane (HMDSO)

### Scheme I

(abbreviated sccm) for HMDSO and 50 to 110 sccm for  $O_2$ , while the system was pumped continuously to maintain a pressure in the range of 10–20 Pa. The RF power generator system generated a plasma with a frequency of about 1 to 50 MHz at 0.1–2.0  $W/cm^2$ , depending on the number and proximity of the electrodes. The PC/ $SiO_x$  laminates produced in this manner used HMDSO at 98% purity (Aldrich Chemicals, Milwaukee, WI) and oxygen at 99.5% purity (National Welders, Durham, NC).

#### 4.2.2 Material Characterization

Measurements of oxygen transmission rates (II) were performed using a temperature-controlled Oxtran 2/20 permeability testing instrument manufactured by Modern Controls, Inc. (Minnesota, MN). To compare barrier performance, measurements were collected at 10, 20, 30, 35 and 40°C at 0% relative humidity. The thickness and refractive index of the  $SiO_x$  coatings were discerned using a Rudolf ellipsometer from coatings deposited on Si wafers. The wavelength and incident angle employed in all of these measurements were 632.8 nm and 70°, respectively. Data were acquired from at least 4 different points on each sample and averaged (the typical standard deviation was less than 1%). Surface morphological characterization was conducted by atomic force microscopy (AFM) with a Digital Instruments Nanoscope D-3000 instrument operated in tapping mode to obtain phase<sup>22</sup> and topographical images, as well as root-mean-square (rms) surface roughness measurements.

## 4.3 RESULTS and DISCUSSION

### 4.3.1 Deposition Time

A series of  $\text{SiO}_x$  films was deposited at varying deposition times between 10 and 120 sec under the following set of constant conditions: a power level of 100 W, a pressure of 16 Pa, and flow rates of 2.5 sccm HMDSO and 70 sccm  $\text{O}_2$ . As seen in Fig. 4.2, one of the primary effects of increasing deposition time is to increase the thickness of the  $\text{SiO}_x$  coating, which, in turn, yields the growth rate achieved for a particular system. Since the coating thickness increases almost linearly with deposition time under the conditions listed above, the growth rate is estimated to be about 1.2 nm/sec. Since thickness varies linearly with deposition time, thickness, rather than time, will be used in future property comparisons. Shown in Fig. 4.3, for instance, is the dependence of  $\Pi$  (Fig. 4.3a) and refractive index (Fig. 4.3b) on coating thickness. A general thickness-induced reduction in  $\Pi$  is in agreement with previously reported results,<sup>23</sup> which find that  $\Pi$  decreases dramatically until a critical coating thickness is attained. Beyond this critical thickness,  $\Pi$  remains relatively constant. Both of these features are evident in Fig. 4.3a, revealing a critical thickness in the vicinity of 60 nm and subsequent  $\Pi$  invariance up to 130 nm.

The strong dependence of  $\Pi$  on coating thickness below the critical thickness has been attributed<sup>23</sup> to the surface nucleation and growth mechanism of  $\text{SiO}_x$  and accompanying lack of uniform coverage early in the deposition. Once the plasma is activated and HMDSO and  $\text{O}_2$  molecules are excited and dissociated to form radicals and ions, these chemically reactive species deposit on the substrate surface. In the case of  $\text{SiO}_x$  deposition, relatively small  $\text{SiO}_x$  clusters nucleate on the substrate surface and grow through coalescence with adjacent clusters to produce a continuous film.<sup>24</sup> At relatively short deposition times (<50 sec, which corresponds to a coating thickness of about 60 nm), the plasma may not be entirely stable, yielding clusters of different size and shape that do not necessarily produce a continuous coating. Large-scale defects (pores) responsible for undesirably high  $\Pi$  by acting as diffusive pathways through the coating remain during this time. Upon plasma

stabilization at the critical coating thickness, good surface coverage is achieved, as evidenced by the reasonably constant value of  $\Pi$ .

Within this regime, fine-scale defects, rather than macroscopic ones, are expected to govern the permeation of penetrant molecules. This change in transport mechanism is supported by the change in refractive index ( $n$ ) with respect to coating thickness, displayed in Fig. 4.3b, since refractive indices are correlated directly with film density and chemical stoichiometry. In the case of silicon oxide thin films,  $n$  has been found<sup>25</sup> to increase with increases in either the mass density ( $d$ ) of the film or the content of Si. Since the HMDSO flow rate, which dictates the concentration of monomer in the chamber, is held constant, the change in  $n$  is attributed solely to film density. The refractive index and mass density are related through the Lorenz-Lorenz equation,<sup>26</sup> which can be expressed as

$$d \propto (n^2-1)/(n^2+1) \quad (1)$$

where the constant of proportionality is system-specific. Corresponding values of  $d_r$ , the mass density of the coating (from Eq. 1) normalized with respect to the maximum  $d$  at relatively long deposition times, are presented for comparison in Fig. 4.3c. According to this figure, the density of the coating after only 20 sec of deposition (25 nm thickness) is 27% lower than that ultimately achieved in the densified coating after long (110 sec) deposition times. The initially low values of  $d_r$  are indicative of macroscopic defects in the coating, as alluded to above. Such defects diminish in both size and density as an increasing fraction of the substrate surface area is covered. When the coating exceeds *ca.* 60 nm in thickness, uniform coverage is achieved, resulting in a densified  $\text{SiO}_x$  thin film.

Another important time- (or thickness-) dependent consideration is the surface morphology of the  $\text{SiO}_x$  coating, since surface characteristics have been reported<sup>20</sup> to vary with barrier performance. In light of the data provided in Fig. 4.3, an accompanying change in the surface morphology of these coatings is anticipated *a priori*. In Fig. 4.4, topographical AFM images of  $\text{SiO}_x$  coatings deposited at varying times are shown. Comparison of these images reveals that, except for the coating corresponding to the

shortest deposition time (Fig. 4.4a), no gross change in surface morphology or roughness is apparent as the coating thickness is increased. The significantly different morphology observed in Fig. 4a is attributed more to the surface characteristics (e.g., roughness) of the PC substrate than to the plasma instability, since the morphologies of coatings below and above the critical thickness appear similar. It should be noted at this juncture, however, that substantially thicker coatings undergo excessive thermal loading and macroscopic cracking, which, by promoting a retrograde increase in  $\Pi$ , compromises the barrier efficacy of the  $\text{SiO}_x$  coating.<sup>12,23</sup>

#### 4.3.2 Deposition Power

A second series of  $\text{SiO}_x$  coatings deposited on PC and reference Si substrates are analyzed here to determine the effect of varying deposition power on  $\Pi$ , coating thickness, refractive index (density) and surface morphology. In this series, the power level is increased from 10 to 120 W. As in the previous sections, other plasma conditions such as pressure (16 Pa), HMDSO and oxygen flow rates (2.5 and 70 sccm, respectively), and deposition time (120 sec) are held constant throughout each deposition. The data displayed in Fig. 4.5 clearly demonstrate that  $\Pi$  for these PC/ $\text{SiO}_x$  laminates decreases abruptly as the power level is increased. Up to about 60 W,  $\Pi$  remains in excess of  $100 \text{ cm}^3/\text{m}^2\text{-atm-day}$ , thereby achieving less than an order of magnitude reduction relative to the uncoated PC substrate ( $\Pi=910 \text{ cm}^3/\text{m}^2\text{-atm-day}$ ). This result suggests that plasma formation is incomplete under these conditions. Sufficient energy is therefore unavailable for HMDSO and oxygen molecules to become excited and dissociate into the chemically active radicals and ions that deposit on the PC and eventually coalesce to form contiguous  $\text{SiO}_x$  films.<sup>24</sup>

Further analysis of Fig. 4.5 reveals that, at power levels greater than 80 W, coatings exhibiting the maximum barrier attainable for the PC/ $\text{SiO}_x$  system are produced. It is well-established<sup>14,27,28</sup> that an increase in discharge power during a PECVD process serves to increase the extent of molecular dissociation, which is also accompanied by an increase in

the kinetic energy of the radicals and ions impinging on the substrate surface. Moreover, an increase in deposition power results in an increase in substrate temperature (by as much as 50°C).<sup>28</sup> [The glass transition temperature for the PC employed here is 150°C, as measured by thermal calorimetry, and is expected to remain sufficiently above any plasma-induced substrate temperature increase to keep the PC from flowing as a melt.] An increase in substrate temperature improves the surface mobility of dissociated HMDSO and O<sub>2</sub> molecules, thereby enhancing the extent by which SiO<sub>x</sub> networks crosslink to form denser and less defective SiO<sub>x</sub> films.<sup>28</sup> All these effects synergistically combine to govern the mechanism of gas transport through the resultant coating. Pronounced excitation of HMDSO and O<sub>2</sub> molecules yields more close-packed layers of SiO<sub>x</sub> and consequently reduces the tortuous pathways (defects) through which O<sub>2</sub> molecules diffuse during  $\Pi$  measurements. In addition, the plasma conditions promote the formation of volatile compounds such as CO, CO<sub>2</sub> and H<sub>2</sub>O,<sup>28</sup> which are vented out of the deposition chamber during PECVD. This reduces the composition of carbon and other impurities incorporated in the coating, thereby improving the chemical purity of the SiO<sub>x</sub> coating (which can affect barrier performance<sup>12,29</sup>).

The thickness of the coating is also influenced by the deposition power level, as is evident in Fig. 4.6. In this figure, the thickness is seen to increase with increasing power to a maximum and then decrease slightly, which is consistent with the data presented in the previous section. An interesting feature of Fig. 4.6 is that the power level (80–100 W) at which the maximum thickness of 145 nm is attained corresponds to the onset of the regime in which  $\Pi$  becomes virtually independent of power (see Fig. 4.5). This confirms the previous conclusion reported by Felts,<sup>23</sup> namely, that a critical thickness is required to achieve markedly improved barrier performance. In contrast to Fig. 2, the data shown in Fig. 4.6 imply that higher power levels only serve to improve the rate of deposition (in nonlinear fashion) to a point. This implication is in agreement with recent studies<sup>27</sup> demonstrating that the deposition rate of organosilicon monomers in a PECVD system

increases initially with increasing power level and then levels off due to monomer depletion (which may serve to explain the reduction in thickness at 120 W in Fig. 4.6). In this case, sufficient energy is available for  $\text{SiO}_x$  network formation (cross-linking), but the amount of HMDSO monomer may simply be insufficient to react with  $\text{O}_2$ . A second plausible explanation for a thickness reduction at high power levels is that the kinetic energy of the ions reach a saturation level, beyond which they have a tendency to sputter the substrate surface.<sup>28</sup> Such ion "splashing" could cause loosely attached material to be removed from the surface, leaving behind potential defect sites.

As pointed out earlier, the mass density of the coating also plays an important role in discerning the degree to which  $\text{SiO}_x$  clusters pack together and, hence, the barrier efficacy of a given coating. The dependence of mass density on deposition power level can be inferred from the refractive index measurements presented in Fig. 4.7. These data, increasing to a saturation level with increasing power, appear similar in magnitude and trend to those shown in Fig. 4.3b and agree with the results of related studies.<sup>30</sup> In a study of electron resonance microwave plasma-deposited silicon oxide films, for example, Herrak and Thomson<sup>30</sup> report an increase in refractive index from 1.44 to 1.47 for a substrate temperature increase from 25 to 300°C (due to an increase in deposition power). The saturation level apparent in Fig. 4.7 occurs over the same power range as that responsible for the low  $\Pi$  values in Fig. 5 due presumably to coating densification. Application of Eq. 4.1 to the refractive index data in Fig. 4.7, followed by normalization with respect to the maximum measured density, yields  $d_r$ , as provided earlier in Fig. 4.3c. A significant difference between the refractive index data included in Figs. 3b and 7 is that the values of  $d_r$  corresponding to the minimum thickness (25 nm) and power level (10 W), respectively, differ considerably: 0.73 from the thickness measurements and 0.93 from the power measurements. This differentiating feature indicates that the coatings produced under the conditions listed at the beginning of this section are relatively dense even at low power levels. Comparison of Figs. 4.5 and 4.7 therefore reveals that bulk density